UNIVERSITÉ DE MONTRÉAL

Ultrashort optical pulse generation from a Cr^{4+}-doped yttrium aluminium garnet tunable solid-state laser

Par

Yongmao Chang

DÉPARTEMENT DE PHYSIQUE

FACULTÉ DES ARTS ET DES SCIENCES

THÈSE PRÉSENTÉE À LA FACULTÉ DES ÉTUDES
SUPÉRIEURES EN VUE DE L'OBTENTION DU GRADE DE
PHILOSOPHIÆ DOCTOR (Ph.D.)
(GÉNIE PHYSIQUE)

Août, 1999

i

UNIVERSITÉ DE MONTRÉAL

FACULTÉ DES ÉTUDES SUPÉRIEURES

Cette thèse intitulée :

Ultrashort optical pulse generation from a Cr^{4+}-doped yttrium aluminium garnet tunable solid-state laser

Présentée par: Yongmao Chang

En vue de l'obtention du grade de Philosophiae Doctor (Ph.D.)
a été dûment acceptée par le jury de l'examen constitué de

....

Dr. Roorda, Sjoerd, Président-rapporteur

....

Dr. Cochrane, Robert William, Membre du jury

....

Dr. Piché, Michel, Examinateur externe

....

Dr. Maciejko, Romain, Co-directeur de recherche

....

Dr. Leonelli, Richard, Directeur de recherche

....

Dr. Stewart, Neil Frederick, Représentant du doyen de la FES

Thèse acceptée le: ......4 novembre 1999......

SOMMAIRE

Cette thèse présente des résultats expérimentaux relatifs à la génération d'impulsions laser ultrabrèves par un système basé sur un grenat d'yttrium-aluminium dopé au chrome (Cr^{4+}:YAG). Le cristal de Cr^{4+}:YAG constitue un mileu de gain élargi par interactions vibroniques qui peut être pompé par un laser Nd:YAG. Il émet entre 1.34 et 1.58 μm à la température de la pièce. La génération d'impulsions ultrabrèves dans cette gamme de longueur d'ondes s'avère importante pour des applications telles les communications ultrarapides par fibre optique ou la spectroscopie résolue en temps de semiconducteurs à bande interdite étroite. Le système décrit ici constitue une alternative efficace à des systèmes plus complexes tels les lasers à centres de couleur ou les oscillateurs paramétriques optiques pompés par un laser titane-saphir.

Le laser Cr^{4+}:YAG développé dans le cadre de cette thèse présente déjà en régime stationnaire plusieurs caractéristiques uniques. Une plage d'accordabilité de 210 nm, soit de 1345 à 1557 nm, a été obtenue avec un seul jeu de miroirs. Une puissance élevée de 730 mW a été mesurée à 1.46 μm avec une puissance de 6.5 W du laser pompe Nd:YAG. L'effet laser s'avère toutefois fortement influencé par la température du cristal de Cr^{4+}:YAG et les effets combinés de lentille thermique et de saturation de l'absorption du faisceau pompe. L'absorption parasite par états excités a été étudiée théoriquement aussi bien qu'expérimentalement. Dans la gamme de longueurs d'onde de l'émission, cette absorption est due à la transition $^3B_2(^3T_2)$ à $^3E(^3T_1(F))$ tandis qu'à la longueur d'onde du faisceau pompe, elle provient de la transition $^3A_2(^3T_2)$ à $^3E(^3T_1(P))$. Les sections efficaces d'absorption par états excités pour les modes libres du laser on été déterminés à partir des données d'efficacité de lasage en tenant compte des paramètres de la cavité.

La possibilité de générer des impulsions ultrabrèves par un laser Cr^{4+}:YAG en utilisant un absorbant saturable basé sur une hétérostructure à confinement quantique a été examinée. L'autodémarrage en mode pulsé du système laser a été obtenu en remplaçant le miroir de fin de cavité par un réflecteur de Bragg contenant deux puits quantiques fortement contraints de GaInAs/InAlAs et en n'utilisant qu'un seul prisme plutôt qu'une

paire pour la compensation de la dispersion du cristal. Des impulsions stables d'une durée de 390 fs on été générées entre 1420 et 1510 nm avec une largeur de bande correspondant voisine de la limite théorique et une puissance de sortie moyenne dépassant les 240 mW. Afin de mieux comprendre le mécanisme conduisant à l'autoblocage de modes, des mesures de diffraction des rayons-X et de photoluminescence à basse température ont été effectuées. La variation rapide de la réponse nonlinéaire du réflecteur de Bragg à puits quantiques est expliquée par la présence de dislocations qui agissent comme centres de recombinaison nonradiatifs.

ABSTRACT

In this thesis, experimental results of ultrashort pulse generation from Cr^{4+}-doped yttrium aluminium garnet (YAG) laser system are presented. The Cr^{4+}:YAG crystal is a vibronically broadened solid state laser gain medium, which lases at room temperature from 1.34 to 1.58 μm and can be pumped by a Nd:YAG laser at 1.06 μm. Ultrashort pulses from this coherent light source are potentially important in technology applications such as ultrafast fiber-optic communications and time-resolved spectroscopy of narrow-bandgap semiconductors. It is a practical alternative to more conventional cryogenic colour center lasers at this wavelength such as NaCl:OH⁻ or complex optical parametric oscillators synchronously pumped by a Ti:sapphire laser.

The cw power performance of a Cr^{4+}:YAG laser was characterized and several unique properties were identified. A broad tuning range of 210 nm, i.e, from 1345 to 1557 nm, was demonstrated by means of one set of mirrors with useful cw output power of as high as 730 mW at 1.46 μm (with a Nd:YAG pump power of 6.5 W). The lasing action was found to be strongly influenced by the temperature of the crystal and the combined effects of thermal lensing and saturable absorption of the pump beam. The excited-state absorption (ESA) at the pump and lasing wavelengths were investigated both experimentally and theoretically. ESA at the lasing wavelength occurs for the transition from the state $^3B_2(^3T_2)$ to $^3E(^3T_1(F))$, while the pump ESA comes from the transition from $^3A_2(^3T_2)$ to $^3E(^3T_1(P))$. The emission ESA cross sections for the free-running modes were estimated from the laser efficiency data by taking into account the pump and cavity parameters.

Ultrashort pulse generation with a Cr^{4+}:YAG laser was investigated using passive mode-locking with a semiconductor quantum well saturable absorber. Self-starting of the laser system was demonstrated using a strained GaInAs/InAlAs saturable Bragg reflector (SBR) with a single prism for dispersion compensation instead of the standard prism pair. Near transform-limited 390 fs long pulses were produced from 1420 to 1510 nm with as high as 240 mW of useful output power. In order to understand the mode-locking

mechanism, the SBR sample was investigated by high resolution x-ray diffraction and photoluminescence measurements. The fast recovery of the SBR nonlinear response was explained by misfit dislocations which act as non-radiative recombination centers.

To:

My parents

Yuehui

Pam Pam

ACKNOWLEDGEMENTS

TABLE OF CONTENTS

List of figures

Chapter 6.

List of Tables

Chapter 1

INTRODUCTION TO ULTRAFAST OPTICAL PULSES

Over the past decades, demand for faster communication speeds has forced computer networks and data communication infrastructures to evolve beyond the limits of traditional copper-based transmission media to the higher bandwidth achievable with fiber optics. Many advances have been seen in optical communication systems. These advances have made possible high-data rate, multi-access optical networks, 2.5 Gb/s and even 10 Gb/s systems. The growth in new services such as the internet, teleconferencing, video-on-demand, CATV and multimedia applications continues to increase the demands on network bandwidth. In such an information age, ultrafast optical research is definitely one of the exciting areas in the field aimed for high capacity optical communications.

People are talking about "ultrashort optical pulses" on various occasions. The definition of what constitutes a short pulse has been revised many times but currently "ultrashort" refers to a duration of few picoseconds or less. Ultrashort optical pulses allow the manipulation and study of physical phenomena on time scales that are inaccessible to any other techniques. Thus, the development of reliable and user-friendly mode-locked lasers has increased the range of commercial and scientific applications for ultrashort pulses, spawning intense research interest in a wide range of technologies.

This chapter includes a simplified description of laser mode-locking. The chapter is organized as follows. A short historical introduction is given in section 1.1. Section 1.2 highlights the important characteristics of tunable solid state laser sources and their favorable features for the generation of ultrashort optical pulses. This special class of lasers is discussed in more detail since all the specific experiments presented later deal with near-infrared tunable solid state lasers, useful for the communication research. Next, there is a description of laser mode-locking, which is the general technique employed in producing a periodic train of short-pulse outputs from lasers. The discussion on the specific mode-locking techniques is deferred until Chapter 2. Section 1.4 presents a

commonly used autocorrelation technique in the characterization of ultrashort optical pulses. After this concise outline of laser mode-locking, some important applications requiring the use of ultrashort pulses are mentioned in Section 1.5. The chapter then concludes with an overview of the thesis outline.

1.1 Brief history of ultrashort laser pulses

The middle of this century witnessed the emergence of new, novel means of generating light [1]. The advent of semiconductor technology in 1948 [2], and later, of the laser technology in 1960 [3], both based on the quantum picture of microsystems, enabled the production of coherent, high intensity, and spectrally well-defined light output. The concurrent development of fiber-optics as a reliable means of telecommunications also required the development of compatible light sources such as the semiconductor laser [4]. The coalescence of semiconductor, laser and guide-wave technology opened the door for faster means of communication and computation. A new technology benefiting from the interaction of these three fields soon emerged and became known as *optoelectronics*, *quantum electronics* or recently, *photonics*.

Over the last thirty years, the development of ultrafast lasers has been described in terms of three generations [5] which have been closely related to breakthroughs in the laser media and appropriate pumping schemes. The first-generation laser pulses were generated mostly from lamp-pumped solid-state lasers, dye lasers and gas lasers. They were mode-locked by active and passive techniques to generate pulses of a few ten picoseconds. The first laser to be mode-locked was a He-Ne laser with nanosecond pulse widths [6]. At that time, active modulation techniques were shown to be unable to mode-lock the whole available gain bandwidth while the pulses generated by passive mode-locking were limited by the recovery time of the resonant saturable absorber. Furthermore, flashlamp pump pulses were limited to a few 100 μs duration, indicating that there was only a limited number of cavity round trips on which the mode-locking mechanism could act.

The second generation of ultrashort lasers appeared quickly after the demonstration of the cw dye laser [7]. The cw mode-locked dye laser [8] takes advantage of the strong

gain/absorption in the dyes to achieve more powerful pulse compression than was hitherto possible. The resulting lasers generated sub-picosecond pulses and it was then necessary to take the group-velocity dispersion (GVD) into account. This led to much better understanding of the interaction between GVD and nonlinear frequency chirp and resulted in the generation of down to 30 femtosecond (fs) pulses, limited by the gain bandwidth of the dyes. Unfortunately, the dyes have a limited lifetime due to photochemical degradation; they are also inconvenient to handle and often toxic and carcinogenic. Such practical considerations with dye lasers soon led to their replacement by femtosecond solid state lasers in most ultrafast laser applications.

The third generation was ushered in by the demonstration of Ti:sapphire as a broadly tunable solid-state laser medium [9]. A femtosecond Ti:sapphire laser pumped with an argon ion laser was first demonstrated in 1990 [10]. It generates pulses as short as 60 fs from a single Ti:sapphire laser cavity. The mode-locking mechanism was soon explained in terms of self-focusing in the laser rod due to the optical Kerr effect [11]. The success achieved with Ti:sapphire lasers led to intense research on other solid-state lasers covering a broader spectral range. Kerr-lens mode-locking was soon successfully applied to other lasers including the diode-pumped Nd:YAG laser [12], the Nd:YAG laser-pumped Cr:forsterite laser [13-14], the argon ion laser pumped Cr:LiSAF laser [15-16], the krypton laser-pumped Cr:LiCAF laser [17] and the Cr:YAG laser [18-19]. Such femtosecond solid-state lasers provide sub-100 fs duration of pulses with direct spectral coverage from 600 – 1600 nm. This range is greatly extended by the use of nonlinear frequency-shifting techniques thanks to the high peak powers available from such lasers.

Today's ultrashort pulse technology has reached the stage of the development of compact practical ultrashort lasers for the real-life application. A large gain-bandwidth is necessary for the generation of ultrashort optical pulses. Tunable solid-state lasers make a practical class of lasers that have an extremely large optical gain bandwidth suitable for short pulse generation. The next section reviews some of their essential features and the physical mechanisms that give rise to the enormous spectral gain bandwidth.

3

1.2 Tunable solid state lasers

Common to all lasers is a means of optical amplification which arises from the stimulated emission of photons between the electronic transition levels of a gain medium which can be in the form of a solid, a liquid or a gas. A pumping mechanism is also required to energetically excite the atoms of the gain medium and to feed power into amplified light. The optical gain, when combined with a suitable amount of positive feedback from highly reflective mirrors, gives rise to oscillations and the generation of a highly intense, coherent light beam. Under most circumstances, the optical gain will saturate, i.e., will start to decrease with the increasing oscillation intensity. When the saturated gain reaches a level that is just large enough to counterbalance the losses experienced by the circulating electromagnetic radiation inside the cavity, a steady-state level is reached. One of the feedback mirrors, usually termed as output coupler, can be made partially reflective and partially transmitting at the oscillation wavelength of the optical resonator, hence aiding in the generation of coherent output power.

Tunability in the sense that the output wavelength of the laser can be varied over a given range is possible. The finite lifetime of the upper lasing level gives rise to the finite spread of frequencies over which optical gain can be achieved, as a consequence of the uncertainty relation. Note gain bandwidth in solid-state lasers is due to phonon broadening (collision). The term 'tunable' usually means that the peak wavelength of the laser emission can be varied over a range that is much greater than several percent of the central oscillation wavelength [21].

The tunable nature of the solid-state lasers arises from the particular characteristics of their gain media. These are insulating crystals (also known as hosts) which have been doped with a small fraction of 3d transition metal ions, such as Ti^{3+}, Cr^{3+}, Cr^{4+} etc. There is a strong coupling between the vibrational energy states of the host crystals and the electronic energy states of the active ion, resulting in broad absorption/emission linewidths. Thus such lasers are also termed as 'vibronic' solid-state lasers. For example, the case of the Cr^{4+} ion as dopant in an yttrium aluminium garnet (YAG) lattice will be thoroughly considered in Chapter 3.

In vibronic lasers, the electronic structure of the laser-active dopant ion is that of argon with the valence electrons filling the 3d shell outside the inert $3s^2$, $3p^6$ configuration. They do not have a complete outer electron shell for electrostatic shielding from neighboring ions, unlike the fixed-wavelength solid-state lasers based on the 4f rare-earth ions such as Nd:YAG. Therefore these electrons are 'exposed' and can interact strongly with the host crystal field. Two major consequences of this fact play a critical role in the lasing characteristic of the gain medium. First, the otherwise parity-forbidden electronic transitions between the lasing states of the free ions become allowed as a result of the crystal field splitting that takes place due to Coulombic interactions with the neighboring lattice ions. Second, a strong coupling occurs between the electronic states of the active dopant ion and the quantized vibrational levels of the lattice.
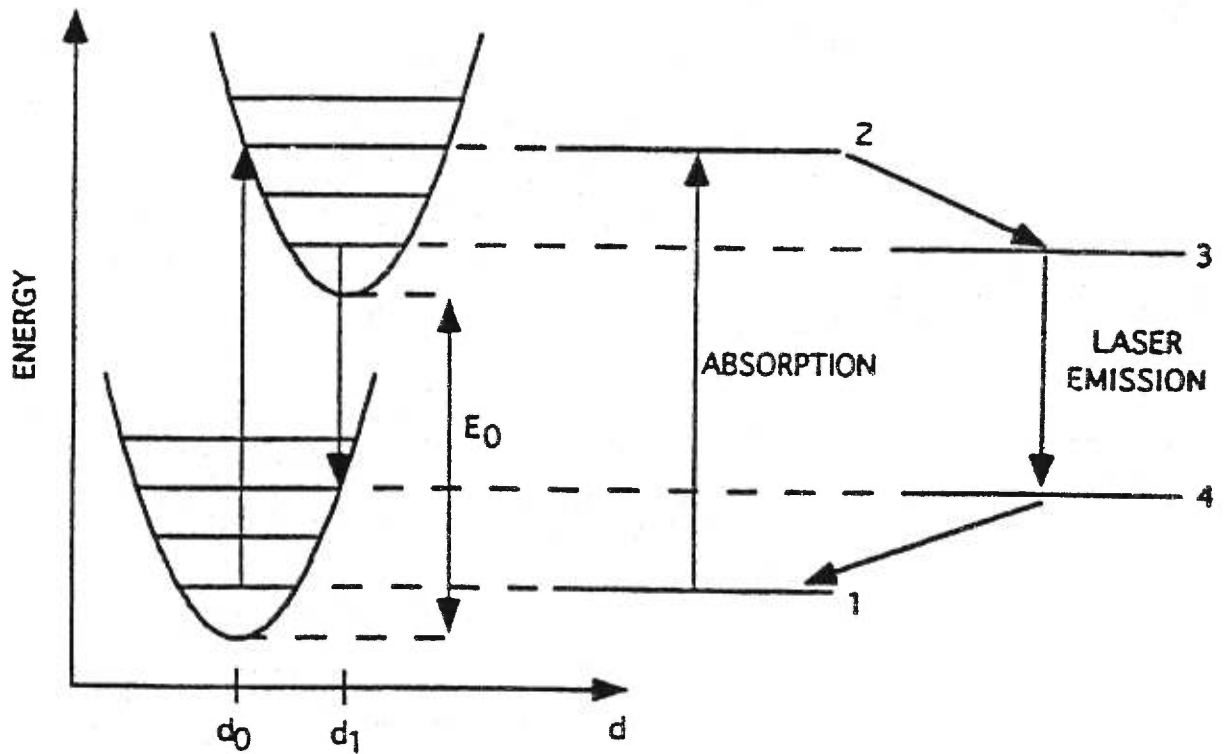
Fig. 1.1 Configuration coordinate diagram of a laser-active dopant in the presence of lattice vibrational coupling.

The configuration coordinate diagram shown in Fig. 1.1 is a convenient way of showing the coupling occuring between the electronic energy states of the dopant ion and the vibrational states of the surrounding lattice ions. The approximate parabola shows the variation of the potential energy about the equilibrium point of the dopant ion as a function of a generalized crystal coordinate d. The ladder energy-levels shown on the right represent the quantized energy-levels of the lattice vibration, each quantum of the lattice vibration being represented by a pseudo-particle also known as phonon. In the absence of any electronic-vibrational coupling, the absorption would have occurred between the ground state and the excited state, only at the wavelength λ_0 corresponding to a so-called zero-phonon energy E_0 which is given by Plank's energy relation as

$$E_0 = \frac{hc}{\lambda_0} = \frac{1.24eV}{\lambda_0(\mu m)} \qquad \text{Eq.1.1}$$

In Eq.1.1, c is the speed of light (3×10^8m/s) and the h is Plank's constant (6.626×10^{-34} J.s). The presence of the lattice vibrational coupling, on the other hand, causes the reconfiguration of the active ion at a new equilibrium position, denoted by d_1 in Fig. 1.1, once excitation takes place. This gives rise to the emergence of a large number of additional possible electronic-vibrationic transitions which are simultaneously accompanied by the emission or absorption of phonons. One possible cycle of such transitions, which make up what is known as a 4-level laser scheme, is also shown in Fig.1.1. The absorption process, occurring between level 1 and level 2, is followed by a fast nonradiative decay with the emission of phonons, bringing the ion to the upper lasing level 3. Stimulated radiative transitions, taking place between level 3 and level 4 which is essentially unpopulated, give rise to the optical gain. Once photons are released by stimulated emission, rapid nonradiative relaxations bring the ion from the lower lasing level 3 to the ground state with the emission of more phonons. The energy difference between the emitted and the absorbed photons (known as the Stokes shift) is transferred through the nonradiative relaxation process to the crystal that also acts as a heat sink to remove the unused heat from the gain medium.

The role of phonons in the laser action has been extensively reviewed in the literature [21-24]. Note that transition-metal ions do not always lead to vibronic lasers in crystals.

For example, Cr^{3+}:sapphire, also known as ruby, gives rise to a narrow linewidth fixed-wavelength laser, while Cr^{3+}:LiSAF leads to a vibronic tunable laser. The difference arises because the local crystal field in LiSAF is stronger than that in sapphire. Nevertheless in ruby, the absorption bands are broad as a consequence of the coupling between the vibrational and the electronic energy levels.
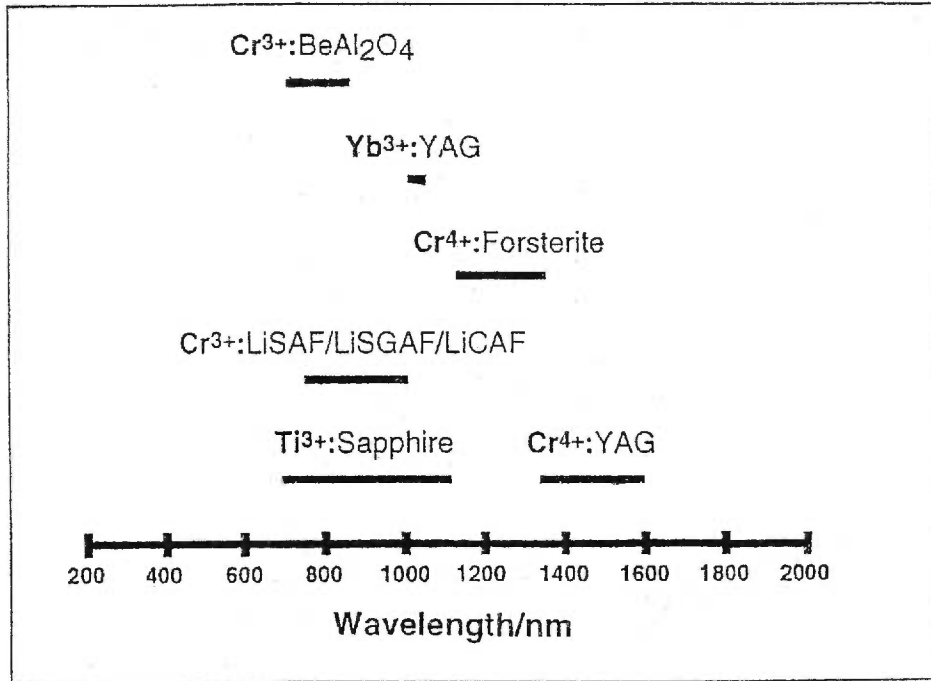
Fig. 1.2 Direct tuning range of room temperature vibronic solid-state lasers.

Historically, tunable laser operation was first reported in Ni^{2+}:MgF_2 [25], Co^{2+}:MgF_2 and ZnF_2 crystals [26] in the early sixties, shortly after the first demonstration of the laser action in ruby [3]. For almost two decades, work in the pursuit of new tunable solid-state lasers lay dormant while color-center lasers [27] (such as NaCl:OH⁻ and KCl:Tl) enjoyed a privileged popularity for obtaining tunable laser output. Those lasers required cryogenic operating temperatures, and because of this inconvenience, vibronic room temperature solid-state laser soon replaced them. With the invention of the Cr^{3+}:$BeAl_2O_4$ (alexandrite) laser, several new, robust, chemically stable, room-temperature, tunable gain media were

discovered [28-33]. Fig. 1.2 gives an idea of the tuning ranges of the more common tunable solid-state lasers.

It should be noted that the huge gain bandwidth (up to approximately 100 THz, i.e. 400 nm for Ti:sapphire) available in these lasers, as shown in Fig. 1.2, is ideal for the generation of extremely short optical pulses. To understand this, the next two sections provide the basics of short pulse generation and characterization.

1.3 Laser mode-locking

A simplified laser resonator including the gain medium and two highly reflective mirrors is depicted in Fig. 1.3. The laser transition of the gain medium has a finite linewidth Δv over which it can provide optical gain such that the laser emission has a finite spectral bandwidth Δv. Consider a laser operating in the TEM_{00} transverse mode with a cavity length L. Such a cavity is capable of supporting a large number of longitudinal electromagnetic field distributions, or longitudinal modes, each of which satisfies Maxwell's equations and the boundary conditions imposed by the mirrors. The frequency difference δv between two adjacent modes (also known as the longitudinal mode spacing), is given by

$$\delta v = v_{n+1} - v_n = \frac{c}{2L} \qquad \text{Eq.1.2}$$

The electrical field of the nth lasing mode E_n at the output coupler is given by

$$E(t)_n = A_n e^{2\pi i [v_0 + (n-1)\delta v + \phi_n]} \qquad \text{Eq.1.3}$$

where A_N is the amplitude of the nth mode, v_0 is frequency of the lowest mode and ϕ_n is a phase factor.

When no attempt is made to control the laser spectrum, the 'free' running laser modes oscillate independently with random phases. Even though the output power may appear time-invariant, the resulting laser output is noisy and incoherent with no regular temporal structure. By using special intracavity devices, all the longitudinal modes may be locked

8

in phase so that ϕ_n in Eq.1.3 is a constant. The oscillating modes will interfere to give a resultant electric field amplitude $E_T(t)$ [34, 35]

$$E_T(t) = e^{i2\pi(\nu_0 + \phi_n)} \sum_{n=1}^{n=N} A_n e^{i2\pi(n-1)\Delta \nu t} \qquad \text{Eq.1.4}$$

Assuming that A_n is the same for all the modes, the amplitude A_T of $E_T(t)$ is expressed as [34]

$$A_T(t) = A_n \left(\frac{\sin(\pi N \Delta \nu t)}{\sin(\pi \Delta \nu t)} \right) \qquad \text{Eq.1.5}$$

The mode-locked output $A_T(t)$ corresponds to a train of pulses separated by the cavity round trip time T_{RT} ($T_{RT} = \frac{1}{\delta \nu} = \frac{c}{2L}$), as shown in Fig. 1.3.
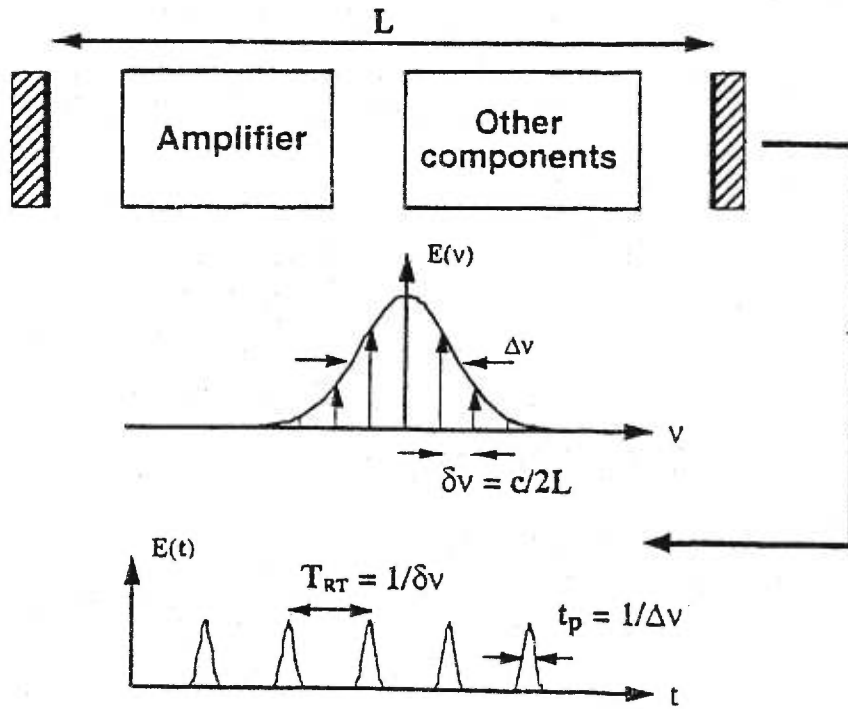
Fig. 1.3 Schematics of the output signal from a mode-locked laser. $E(\nu)$ is the electric field amplitude as a function of frequency ν, and $E(t)$ is its Fourier transform in the time domain.

The temporal profile is the Fourier transform of the spectral profile and the duration of the pulses, t_p, is inversely proportional to the full gain-linewidth given by Heisenberg's uncertainty principle [20],

$$\Delta v \bullet t_p \geq k \qquad\qquad \text{Eq.1.6}$$

where k is a factor which depends only on the specific pulse shape (For example, $k = 0.441$ for a Gaussian pulse, 0.315 for hyperbolic secant pulses and 0.11 for single-sided exponential pulses). When $\Delta v \bullet t_p = k$, the optical pulses are said to be '*transform-limited*', i.e., the pulsewidth takes the minimum value which can be supported by the spectral bandwidth. In other words, in order to generate ultrashort pulses in the time domain, it is necessary to achieve a mode-locked laser output with a broad spectral-width in the frequency domain. For this reason, the shortest optical pulses are generated from those gain media with the broadest spectral gain profile. This explains why the broadly tunable vibronic lasers discussed in Section 1.2 are a good choice for the realization of femtosecond lasers.

The purpose of mode-locking is to ensure that the oscillating laser modes are locked together in phase. Chapter 2 deals with the various techniques employed for mode-locking lasers. The next section describes commonly employed techniques for characterizing ultrashort pulses.

1.4 Characterization of optical pulses

Since there are no readily available direct pulse measurements at time scales shorter than about one picosecond, the ultrashort pulsewidths of mode-locked lasers are obtained from autocorrelation measurements [36], first demonstrated in 1966 by Maier et al. [37]. The method is depicted in Fig. 1.4. A pulse train is split by a 50/50 beam splitter into two equal-intensity beams which are then fed into the arms of a Michelson interferometer. Mirror M2 is mounted on a moving stage so that a variable delay can be introduced between the pulse trains when they are combined. Light is then focused onto a phase-matched birefringent crystal to generate the second harmonic of the input radiation. A

filter separates the fundamental light from the second harmonic signal monitored with a photomultiplier connected to an oscilloscope.
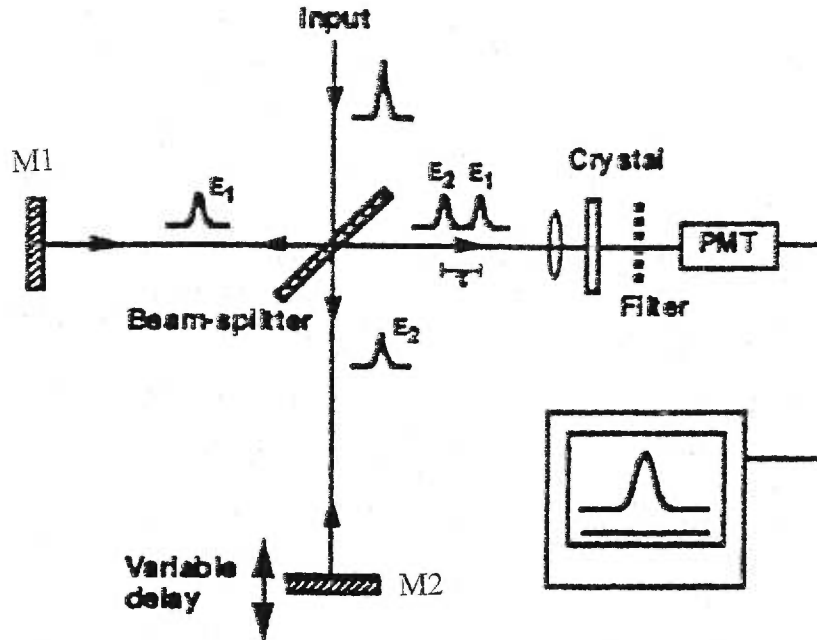
Fig.1.4 Schematic of second harmonic autocorrelator

The time delay τ between the two pulse trains in Fig. 1.4 can be calculated from the displacement Δl of mirror M2

$$\tau = \frac{2\Delta l}{c} \qquad\qquad \text{Eq.1.7}$$

where c is the speed of light. For example, a displacement of 1 mm corresponds to a time delay of 6.67 ps. The intensity of the second harmonic $I_{2\omega}$ is proportional to the square of the incident fundamental power in the crystal, which is given by

$$I_{2\omega}(\tau) = \int \left| E_1(t) + E_2(t+\tau) \right|^2 dt \qquad\qquad \text{Eq.1.8}$$

One sees that the monitored signal is a function of the time delay τ. As the time delay is adjusted, the two pulses interfere with one another and generate fringes. In particular, if the two beams are collinear and a slow scan process is used, the rapid fringe-like variations

of the interference pulses are averaged out and the recorded second harmonic intensity is given by [36]

$$I_{2\omega}(\tau) = a[1 + 2G(\tau)]$$ Eq.1.9

where a is a constant and $G(\tau)$ is the normalized second order autocorrelation function expressed as :

$$G(\tau) = \frac{\int I(t-\tau)I(t)dt}{\int I(t)^2 dt}$$ Eq.1.10

A background second harmonic signal is generated by the individual pulses as seen from Eq.1.9, even when the delay between them is large enough that they do not overlap in the crystal. As the delay is reduced, the superposition of the pulses generates a higher peak intensity in the crystal and the second harmonic signal increases. When the time delay $\tau = 0$, $G(0) = 1$ and the autocorrelation of the pulse has a contrast ratio of 3:1 compared to the background signal. In practice, the beams from the autocorrelator are arranged to be non-colinear and to intersect in the crystal. In this phase-matching configuration, a background-free autocorrelation trace can be obtained.

The actual functional form of the autocorrelation function depends on the specific pulse profile. An intensity profile has to be assumed in order to establish a relationship between the original pulse duration and the width of the autocorrelation function. Table.1.1 presents the ratio of autocorrelation width to pulse duration for the two most common pulse shapes as well as the products of their associated bandwidths [36].

Table 1.1 Table of time bandwidths and autocorrelation widths for Gaussian and sech^2 pulses

Pulse shape	$\Delta v \bullet t_p \geq k$	τ_{au} / τ_p
Sech^2	0.315	1.543
Gaussian	0.441	1.414

A complete characterization of the ultrashort optical pulses requires a measurement of the corresponding spectral distribution of the pulse intensity as a function of wavelength. The resulting time-bandwidth product deduced from the autocorrelation trace and the spectrum measurement must be consistent with the assumed pulse shape in order to conclude that the pulses are transform-limited. To record the real-time spectral intensity variation of the pulses, a scanning spectrometer (Rees, model 212A) was routinely employed in our experiments.

1.5 Application of ultrashort pulses

Most applications in which mode-locked lasers have been utilized can be classified into two categories: those requiring extremely short time resolution and those employing the high-peak intensities of the pulses. In the first category, widely tunable femtosecond lasers permit time-resolved studies of many physical, chemical and biological processes. Mode-locked lasers in different wavelength regions have been used to probe new semiconductor materials and devices to measure the time duration of relaxation events, employing correlation techniques [38]. Since available purely electronic devices are incapable of accessing time scales shorter than one ps, mode-locked pulses may be conveniently used to define time scales in reference to which fast events can be measured. A possible application of time-resolved spectroscopy studies is the development of ultrafast electronic devices, such as photonics switches [39].

Many chemical processes are also studied using femtosecond optical pulses. The chemical reactions proceed via unstable intermediate states that last only a few hundred fs and in order to understand the reaction process, the structure and the lifetime of the intermediate states need to be known. A pump pulse is absorbed by the material under study to initiate the reaction. The progress of the reaction is monitored by a probe pulse after a short time delay, such that the change in absorption in the reactants can be measured. This can be used to determine the evolution of a chemical process by adjusting the time delay between the two pulses.

In the second category, mode-locked lasers have been used in the study of numerous nonlinear processes requiring very high intensities to be observed. One such important example that may dramatically change tomorrow's communication technology is the soliton transmission systems in which a mode-locked laser is used to launch solitons in an optical fiber. As a result of the precise balance between the nonlinearities and the dispersion experienced by the high-intensity pulses, essentially distortion-free pulse propagation can be accomplished over very long distances [40]. Soliton systems have demonstrated transmission over 1,000,000 km at Gbits/s speeds [41]. In other applications requiring high intensities, mode-locked lasers have been used to access new wavelength regions by nonlinear frequency conversion techniques such as second harmonic conversion [42] and optical parametric oscillation [43].

High power femtosecond laser sources at 1.5 μm are also useful to test optical communication systems and to investigate non-linear effects which may be needed for the future development of high capacity systems. A femtosecond pulse will have a spectral width of several nanometers and laser gain media with large bandwidths will be required to support and amplify ultrashort pulses.

1.6 Outline of the thesis

This thesis describes the experimental and theoretical work carried out to generate ultrashort pulses based on the newly developed Cr^{4+}:YAG laser crystal. The broad emission band of Cr^{4+}:YAG matches well with the spectral range utilized for fiber optic communications. This subject is thus of great interest because of the high demand for this laser source as a measurement instrument and for optical telecommunication characterization. To build such an ultrafast laser source is thus a target of quite a few laboratories. However, there are several problems associated with this laser, such as thermal lensing, crystal quality and excited-state absorption. Moreover, contrary to Ti:sapphire laser, the Kerr-lens mode-locking of Cr^{4+}:YAG laser does not function properly, i.e., the operational regime is erratic, and seldom reproducible for crystal to

crystal. In fact, this represented a major challenge to the author especially at the early stage of the construct of the Cr^{4+}:YAG laser from scratch.

This thesis is organized as follows. As a detailed introduction, Chapter 2 describes the different mode-locking techniques and some of the theoretical background behind the laser resonators for the generation of optical pulses. Pulse duration measurements by means of the second harmonic autocorrelation are discussed. The rest of the thesis deals with the application of passive mode-locking to the Cr^{4+}:YAG laser with a self-starting nature.

Chapter 3 deals with the theoretical work on excited-state absorption (ESA) for the laser gain medium. The crystal-field energy levels for the Cr^{4+} ions in the D_{2d} site symmetry in the YAG lattice are investigated by diagonalizing the Hamiltonian matrices including the electrostatic term, the Trees correction and the crystal-field interaction as well as the spin-orbit coupling. For the first time the ligand-field theory is extended to include the D_{2d} site symmetry. A good agreement with the experimental data is obtained and the ESA associated transitions are explained. The presence of ESA due to the Cr^{4+} ions is an intrinsic limit to the laser performance. Because few detailed experimental characterizations of this tunable solid-state laser are available in the literature, the experimental investigation of the continuous-wave (cw) laser performance of Cr^{4+}:YAG is described in Chapter 4, including the details of slope efficiency, tuning range, saturable absorption and thermal lensing effects. A broad tuning range of 210 nm, i.e., from 1345 to 1557 nm, was obtained, significantly exceeding the results previously reported in the literature with one set of mirrors.

The subsequent chapter deals with ultrashort pulse generation with Cr^{4+}:YAG laser. We concentrate on the self-starting Cr^{4+}:YAG laser passively mode-locked with a semiconductor quantum well saturable absorber. Self-starting of the laser system is demonstrated using a strained GaInAs/InAlAs saturable Bragg reflector (SBR) with a single prism for dispersion compensation instead of the standard prism pair. This is the first time in Canada to mode-locking of a Cr^{4+}:YAG laser with stable subpicosecond pulses were achieved. This chapter also discusses the mode-locking mechanism. Results on the characterization of the SBR by means of high-resolution x-ray diffraction and liquid-helium temperature photoluminescence measurements are reported for the first time.

1.7 References

1. Derry T.K. and Williams T.I., *"A short history of technology"*, (Dover, New York, 1993), p.633.

2. Bardeen J. and Brattain W.H., *"The transistor – a semiconductor diode"*, Phys. Rev. **74**, 230 (1948)

3. Maiman T., *"Stimulated optical radiation in ruby"*, Nature **187**, 493 (1960).

4. Van Heel A.C.S., *"A new method of transporting optical images without aberration"*, Nature **173**, 39 (1954).

5. Krausz F., Fermann M.F., Brabec J., Curley P.F., Hofer M., Ober M.H., Spielmann Ch., Wintner E. and Schmidt A.J., IEEE J. Quantum Electron. **28**, 2097 (1992).

6. Hargrove L.E., Fork R.L. and Polock M.A., Appl. Phys. Lett. **5**, 4 (1964).

7. Peterson O.G., Yuccio S.A. and Snavely B.B., Appl. Phys. Lett **17**, 245 (1970).

8. Ippen E.P., Shank C.V. and Dienes A., Appl. Phys. Lett. **21**, 348 (1972).

9. Moulton P.F., J. Opt. Soc. Am. B **3**, 125 (1986).

10. Spence D.E., Kean P.N. and Sibbett W., *Sub-100 fs pulse generation from a self-mode-locked Ti:sapphire laser*, Conference on Laser and Electro-Optics (Optical Society of America, Anaheim, 1990) paper CPDP-10-1, pp 619-20.

11. Piché M., Opt. Commun. **86**, 156 (1991).

12. Liu K.X., Flood C.J., Walker D.R. and van Driel H.M., Opt. Lett., **17**, 1361 (1992).

13. Seas A., Petricevic V. and Alfano R.R., Opt. Lett. **17**, 937 (1992).

14. Sennaroglu A., Pollack C.R. and Nathel H., Opt. Lett. **18**, 826 (1993).

15. Li Kam Wa P., Chai B.H. and Miller A., Electron. Lett. **27**, 2351 (1991).

16. Rizvi N.H., French P.M.W. and Taylor J.R., Opt. Lett. **17**, 879 (1992).

17. Evans J.M., Spence D.E., Sibbett W., Chai B.H.T. and Miller A., Opt. Lett. **17**, 1447 (1992).

18. Sennaroglu A., Pollack C.R. and Nathel H., Opt. Lett. **19**, 390 (1994).

19. Colon P., Tong Y.P., French P.M.W., Taylor J.R. and Shestakov A.V., Opt. Lett. **19**, 1468 (1994).

20. Siegman A.E., *Lasers,* (Millverlley, CA, University Science books, 1986).

21. Moulton P.F., *"Tunable solid-state lasers"*, Proc. IEEE **80**, 348 (1992).

22. Walling J.C., *"Tunable parametric-ion solid-state lasers"*, in *Tunable lasers*, L.F. Mollenauer, J.C. Pollock, eds., Springer Topics in Applied Physics, (Springer-Verlag, Berlin, 1992), p.331.

23. Koechner W., *Solid State Laser Engineering,* 2nd Ed (Springer series in optical sciences 1) (Berlin: Springer, 1977).

24. Payne S.A. and Albrecht G.F., 1991 *Encyclopedia of lasers and Optical Technology* (San Diego, CA: Academic) p.603-24.

25. Johnson L.F., Dietz R.E. and Guggenheim H.J., *"Optical maser oscillation from $Ni^{2+}:MgF_2$ involving simultaneous emission of phonons"*, Phys. Rev. Lett. **11**, 318 (1963).

26. Johnson L.F., Dietz R.E. and Guggenheim H.J., *"Spontaneous and stimulated emission from Co^{2+} ion in MgF_2 and ZnF_2"*, Appl. Phys. Lett. **5**, 21 (1964).

27. Pollack C.R., 1991 *Encyclopedia of lasers and Optical Technology* (San Diego, CA: Academic) p.9-26.

28. Walling J.C., Heller D.F., Samelson H., Harter D.J., Pete J.A. and Morris R.C., *"Tunable alexandrite lasers: development and performance"*, IEEE J. Quantum Electron. **21**, 1568 (1985).

29. Moulton P.F., *"Spectroscopic and laser characteristics of $Ti:Al_2O_3$"*, J. Opt. Soc. Am. B **3**, 125 (1986).

30. Payne S.A., Chase L.L., Newkirk H.W., Smith L.K. and Krupke W.F., *"$LiCaAlF_6:Cr^{3+}$: A promising new solid-state laser material"*, IEEE J. Quantum Electron. **24**, 2243 (1988).

31. Petricevic V., Gayen S.K., Alfano R.R., Yamagishi K., Anzai H. and Yamaguchi Y., *"Laser action in chromium-doped forsterite"*, Appl. Phys. Lett. **52**, 1040 (1988).

32. Angert N.B., Borodin N.I., Garmash V.M., Zhitnyuk V.A., Okkrimchuk A.G., Siyuchenko O.G. and Shestakov A.V., *"Lasing due to impurity color centers in yttrium aluminum garnet crystals at wavelengths in the range 1.35 – 1.45 μm"*, Sov. J. Quantum Electron. **18**, 73 (1988).

33. Payne S.A., Chase L.L., Smith L.K., Kway W.L. and Newkirk H.W., *"Lasing performance of LiSrAlF$_6$:Cr^{3+} crystal"*, J. Appl. Phys. **66**, 1051 (1989).

34. New G.H.C., Rep. Prog. Phys. **46**, 877 (1983).

35. Svelto O., *"Techniques of solid-state lasers"*, in *Laser handbook*, F.T. Arecchi and E.O. Schulz-Dubois, eds., (North-Holland, Amsterdam, 1972), p.529.

36. Diels J.C., Foutaine J.J., McMichael I.C. and Simon F., Appl. Opt. **24**, 1270-82 (1980).

37. Maier M., Kaiser W. and Giordimaine J.A., Phys. Rev. Lett. **17**, 1275 (1966).

38. Gobel E.O., *"Ultrafast spectroscopy of semiconductors"*, Opt. and Photonics News **3**, 33 (1992).

39. Stegeman G.I. and Miller A., in *Photonics in switching*, ed. J. Midwinter (Academic, Cambridge, MA, 1993), p.81.

40. Mollenauer L.F., *"Soliton transmission speeds greatly multiplied by sliding-frequency guiding filters"*, Opt. and Photonics News **5**, 115 (1994).

41. Nakazawa M., Yamada E., Kubota H. and Suzuki K., Electron. Lett. **27**, 1270 (1992).

42. Ellingson R.J. and Tang C.L., *"High-repetition-rate fs pulse generation in the blue"*, Opt. Lett. **17**, 343 (1992).

43. Wachman E.S., Edelstein D.C. and Tang C.L., *"CW mode-locked and dispersion compensated femtosecond optical parametric oscilators"*, Opt. Lett. **15**, 136 (1990).

Chapter 2

Generation of laser pulses by mode-locking techniques

2.1 Introduction

As described in Chapter 1, the goal of mode-locking is to ensure that the oscillating laser modes are locked together in phase. Since the first demonstration of laser mode-locking by Hargrove et al. in 1964 [1], a number of novel mode-locking techniques have been proposed and demonstrated in solid state, liquid (dye) and gas lasers. This chapter highlights the important contributions in the experimental techniques of longitudinal mode-locking to generate ultrashort pulses and provides examples of gain media in which these techniques have been shown to work. Emphasis will be placed on those schemes that are related to the experimental work presented in this thesis. For the sake of completeness, active mode-locking will be included. Review articles giving more detailed accounts of the various topics brought up in this chapter have been written by Smith [2], Demaria et al. [3], Siegman and Kuizenga [4], Fork et al. [5], Krausz et al. [6] and French [7].

(a) Active mode-locking   (b) Passive mode-locking

| Amplifier | Modulator | | Amplifier | Intensity – dependent loss |
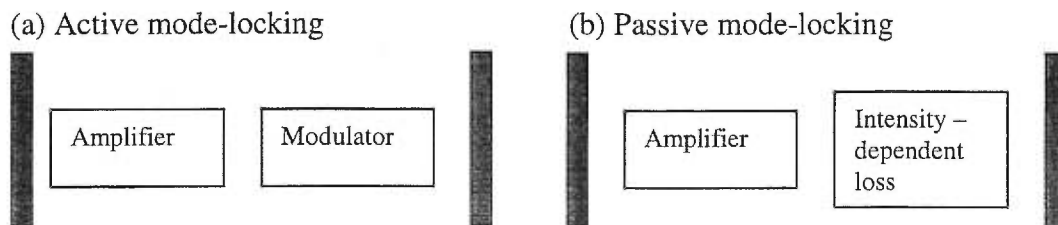
Fig. 2.1 Schematics of active and passive mode-locking

The techniques for mode-locking lasers fall into two categories: active and passive mode-locking. These approaches are schematically represented in Fig. 2.1. In the first case, the radiation in the laser cavity is modulated by a signal derived from an external clock source which is matched to the cavity round trip delay time. In the second case, the laser radiation itself generates a modulation through the action of a nonlinear device in the

laser cavity. This modulation is thus automatically synchronized to the cavity round trip frequency and requires no external clock signal.

2.2 Active mode-locking

Active mode-locking techniques, which were among the first to be applied to lasers in order to obtain reliable ultrashort pulse duration, involve the synchronized modulation of the round-trip cavity loss or gain at the frequency equal to that of the axial mode spacing or one of its harmonics. Stable mode-locking operation can only be supported when the external signal is present. Viewed in the time domain, the periodically varying net cavity loss allows the circulating electromagnetic-field distribution to lase only in a narrow time window around the maximum of the modulator transmission, resulting in the temporal shaping of an output pulse shorter than the cavity round-trip transit time. Equivalently, one can picture the same effect in the frequency domain where the intracavity modulator generates frequency sidebands overlapping with the neighboring axial modes and causing them to be coupled together. As will be elaborated in the following subsections, the three commonly used active mode-locking schemes are amplitude modulation, frequency modulation, and synchronous pumping.

2.2.1 Amplitude modulation (AM) mode-locking

In an AM mode-locked laser, a low-amplitude intensity modulation is imposed on the intracavity laser beam. This modulation is usually achieved by inserting an acousto-optic modulator driven by an electric signal so that a time-varying acoustic wave is generated in the modulator; this creates a periodic diffraction loss in the laser. Consider a longitudinal cavity mode of frequency ν which has a sinusoidal amplitude-modulation imposed upon it at frequency f with a modulation depth δ_1. The electric field is given by

$$E = ((1 - \delta_1) + \delta_1 \, sin \, 2\pi f t \,)) E_0 \, sin \, 2\pi \nu t \qquad \text{Eq.2.1}$$

The electric field can be resolved into three distinct frequency components.

$$E = E_0[\sin 2\pi v t + \frac{\delta_1}{2}\sin 2\pi(v + f) + \frac{\delta_1}{2}\sin 2\pi(v - f)] \qquad \text{Eq.2.2}$$

The first component at frequency v corresponds to the original longitudinal mode but the other two components at $(v - f)$ and $(v + f)$ are side bands which beat in phase with the parent mode. It will coherently drive them to oscillate in phase if the modulation frequency f is set equal to the longitudinal mode spacing. All the lasing modes in the cavity are subject to the same modulation and phase locking spreads through the lasing bandwidth to generate a mode-locked pulse.

The laser can also be mode-locked at frequencies that are integer multiples of the cavity round trip time, i.e., $f = n\Delta v$ where n is an integer. In this case the side bands generated from the pth mode overlap with the $(n+p)^{th}$ mode and the $(n-p)^{th}$ mode. With both fundamental and higher order modulations, the optical pulse synchronises itself with the phase of the RF electrical signal to arrive at the modulator when the transmission is maximum and the acoustic wave amplitude is minimum.

Several authors have made detailed studies of the dynamics of AM mode-locking [8,9,10] to understand the pulse formation process. Following Kuizenga and Siegman [10], a Gaussian pulse is traced through several round trips in the cavity and a self-consistent solution is sought. This gives the pulse duration τ_p,

$$\tau_p = \frac{\sqrt{\sqrt{2}\ln 2}}{\pi}\left(\frac{g_0}{\delta_1}\right)^{\frac{1}{4}}\left(\frac{1}{f_m\Delta F}\right)^{\frac{1}{2}} \qquad \text{Eq.2.3}$$

where δ_1 is the modulation depth, ΔF is the gain bandwidth and f_m is the modulation frequency. The saturated round-trip gain g_0 is given by

$$g_0 = \frac{1}{2}\ln\left[\frac{1}{1-L}\right] \qquad \text{Eq.2.4}$$

where L is the round-trip cavity loss.

Eq.2.3 shows that the pulse duration can be decreased by increasing the depth of modulation δ_1 and by increasing the modulation frequency f_m (i.e. by locking at a higher harmonic of the cavity length). The modulator driving power P_m is proportional to the square of the modulation depth and the pulse duration τ_p scales with the power as $(1/P_m)^{1/8}$. The pulse duration will therefore only decrease slowly with an increasing RF

power and therefore increasing f_m is the most effective way to reduce the pulse duration in an actively mode-locked laser.

Because of its straightforward implementation and the fact that all of the modulator parts can be commercially obtained, it is usually the first mode-locking technique to be pursued in order to produce ultrashort pulses from a new laser source. Some examples of optical gain media where AM mode-locking has been successfully demonstrated include Nd:glass [11], Nd:YAG [12], Ar$^+$-ion [13], Rh6G [14], KCl:Tl^0 [15], Ti:sapphire [16], Cr:forsterite [17], and Cr:YAG [18]. One notes that in the case of broadly tunable lasers, capable of producing subpicosecond pulses, pulsewidths obtained through AM mode-locking does not use up much of the available gain bandwidth. Usually, there are two reasons for this. One reason is that a long transient build-up time is required to couple the axial modes over a large bandwidth. Over such a long period the circulating pulse may no longer stay in synchronism with the driving RF source to get successively shorter and the pulsewidth gets clamped at a larger value. More importantly, as the pulse gets shorter, approaching 1 ps, dispersive pulse broadening effects in the gain medium and other intracavity elements become the dominant pulsewidth limiting factors. Effects of dispersion on pulsewidth will be further discussed in Section 2.4.

2.2.2 Frequency modulation (FM) mode-locking

An alternative way of periodically varying the intracavity loss is through frequency modulation (FM). In FM mode-locking, the index of refraction of an intracavity element, usually an electro-optic material, is sinusoidally varied at a frequency equal to the axial mode spacing. The instantaneous phase shift on passing through the modulator is proportional to the rate of change in the applied RF signal. Only light which travels through the modulator when the applied RF signal is maximum or minimum will be unchirped. The modulation frequency is a multiple of the round trip time and so the frequency shift imparted to the light will be the same on each pass through the modulator and will accumulate on successive round trips in the cavity. The accumulated frequency shift will eventually push the light outside the lasing bandwidth. The light which is

synchronised with the zero frequency shift time window in the modulator will be unaffected and will be amplified on successive round-trips so that a pulse will be generated. A full analysis gives the following pulse duration [10],

$$\tau_p = \frac{\sqrt{2\sqrt{2}\ln 2}}{\pi}\left(\frac{g_0}{\delta_c}\right)^{\frac{1}{4}}\left(\frac{1}{f_m \Delta F}\right)^{\frac{1}{2}} \qquad \text{Eq.2.5}$$

This expression for the pulse width for FM mode-locking is similar to the AM mode-locking case of Eq.2.3 except for an extra factor of $\sqrt{2}$. The pulses produced by FM mode-locking are linearly chirped due to the quadratic variation of phase around the zero phase-shift window.
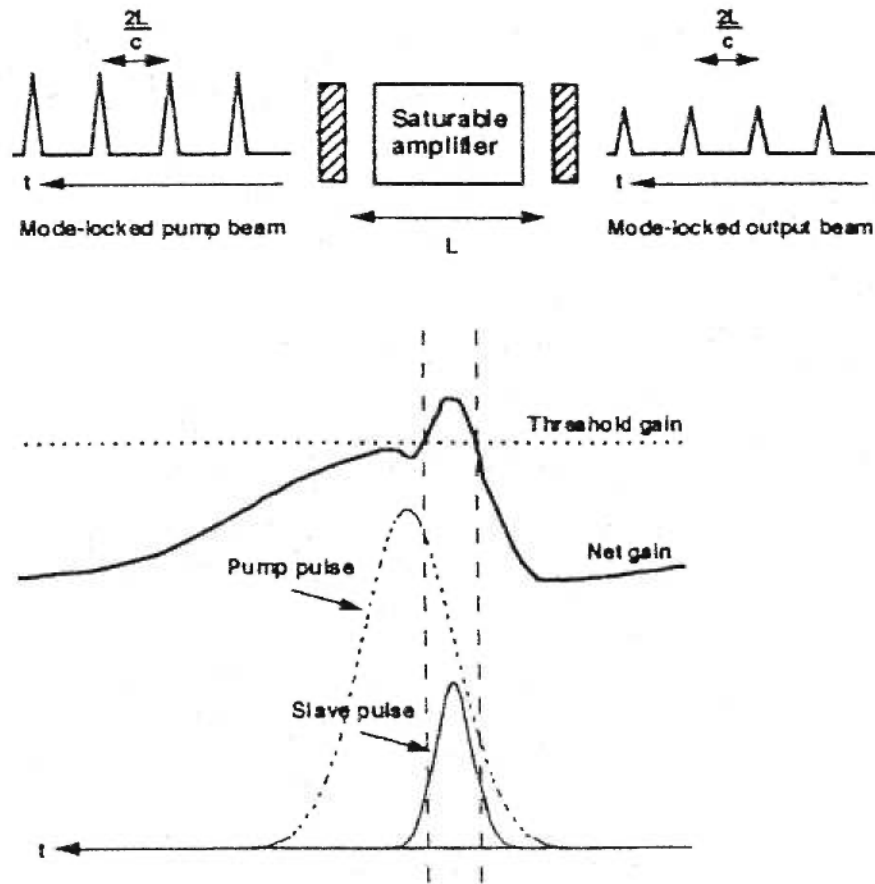
Fig. 2.2 Schematics of a synchronously pumped system.

2.2.3 Synchronous pumping

Synchronous pumping, on the other hand, is used to periodically vary the gain of a laser. It differs from the loss modulation in that it requires gain saturation to work efficiently. Fig. 2.2 illustrates the basic principle of operation. Essentially, the laser medium is resonantly (or 'synchronously') pumped by a train of pulses from another mode-locked laser. The rate at which the gain is 'switched on' in the slave laser follows the profile of the pump laser. The gain is then 'switched off' by gain saturation which can occur on a time scale faster than the pump pulse duration. This completes the 'fast modulation function' and explains why synchronously mode-locked lasers generate pulses significantly shorter than those obtained with conventional active mode-locking through loss modulation. The length of the synchronously pumped laser, sometimes called the 'slave laser', is set to correspond to the repetition rate of the pump pulse train, derived from the 'master laser'.

2.3 Passive mode-locking

Unlike the active mode-locking techniques discussed in the previous sections, passive mode-locking does not require an external modulator to maintain steady pulses. The major characteristic of the technique is the presence of an intensity-dependent saturable loss mechanism, resulting from a saturable absorber. A saturable absorber is a material whose optical density decreases when the intensity of the incident light increases. In the initial stages of the lasing action in a resonator, the electromagnetic energy distribution consists of randomly distributed noise spikes covering the whole emission bandwidth. As the lasing action begins to take place, the saturable absorber selects and favours the growth of the noise burst with the highest peak power at the expense of the other noise bursts, ultimately leading to a short output pulse. The saturable absorber, which comes in a variety of forms, has more enhanced pulse shortening action, the shorter the pulses get. One can alternatively say that the effective modulation depth which is independent of the

pulse width in active mode-locking is actually controlled by the pulse itself in passive mode-locking. This gives rise to pulses much shorter than those produced by the active mode-locking mechanisms alone as the ultimate pulsewidth is no longer limited by the fixed modulation strength but by the gain bandwidth, the saturable absorber action, and dispersive effects.

Quite generally, passive mode-locking may be divided into two categories: resonant and nonresonant passive mode-locking. The former relies on the saturation effects in wavelength-dependent absorption process as will be discussed in Sections 2.3.1 to 2.3.3. Section 2.3.4 covers nonresonant passive mode-locking techniques, where fast-saturable-absorption-like action can be created by exploiting Kerr nonlinearities in a medium.

2.3.1 Passive mode-locking with a resonant saturable absorber

In a resonant saturable absorber, the effect is associated with a particular electro-magnetic transition in a material. It is therefore wavelength dependent. Different absorbers have to be chosen to cover different parts of the spectrum. When light of an appropriate wavelength enters a resonant saturable absorber, electrons in the active centres are excited from the ground state to an excited state. Once an active centre has absorbed a photon, it cannot attenuate the beam any further ('bandfilling') until it has dissipated its stored energy and returned to the ground state. When the incident light intensity is low, only a small fraction of the available absorption sites will be excited at any one time and the absorption of the material will be high. As the intensity is increased, more of the absorption centres will be excited and fewer will be available to attenuate the beam and eventually, a point will be reached where no more light can be absorbed. Once the light intensity has exceeded this saturation threshold, the absorber will be effectively transparent. A saturable absorber will therefore transmit short, high intensity pulses but will attenuate low intensity CW radiation.

The excited upper-state of an absorber will have a characteristic lifetime such that the absorption will not immediately recover after an intense pulse has passed through. The recovery time of the absorber can be the principal factor which sets a limit on the pulse

25

duration produced by a passively mode-locked laser. But some extra compression beyond the absorber recovery time can be achieved by taking advantage of the interplay with the saturable gain of the lasing medium. In this case, the low leading edge of the pulse will be attenuated and shaped by the saturable absorber effect until the pulse intensity exceeds the saturation threshold. If the saturation energy of the lasing medium is low, then the front and the middle portion of the pulse will saturate the gain and deplete the inversion such that most of the trailing edge will not be amplified. The depletion of the gain by the leading edge of the pulse provides additional pulse compression and this effect is particularly useful in dye lasers where the saturation fluence is low. As an example of slow saturable absorber mode-locking, dye lasers are discussed in the following section.

2.3.2 Passively mode-locked dye lasers.

Many organic dye compounds are useful when selecting laser media for mode-locking because the wide bandwidths and fast recovery times of their optical transitions enable them to support ultra-short pulses. In the first experiments on passive mode-locking, a dye cell was introduced into the cavity of a ruby laser to act as a saturable absorber [19], giving pulses of a few ns. The first passively mode-locked dye laser was demonstrated by Ippen et al. [20], obtaining 1.5 ps pulses tunable from 590 to 610 nm. This was further reduced to 300 fs by Bradley et al. [21] by placing the absorber at the output mirror.

The combined action of the saturable absorber and dynamic gain saturation leading to cw ultrashort pulse trains was theoretically treated by New [22] in the "quasi-continuous mode-locking" model, successfully explaining the obtained results. In the hope of coming up with a close-form solution, a more analytical approach was employed by Haus [23-24]. He treated the problem of passive mode-locking with both fast and slow saturable absorbers for a homogeneously broadened laser through a rate equation analysis and showed that the output temporal pulse envelope is quite accurately given by

$$I = I_0 \sec h^2 (\frac{t}{\tau_p}) \qquad\qquad \text{Eq.2.6}$$

26

where the pulse width τ_p depends on the gain medium and the saturable absorber parameters. Haus further extended his model and explained various parameter ranges which give rise to mode-locking, relaxation oscillation, and so on [25]. In particular, the recently developed Kerr-lens mode-locking to be discussed later can also be understood as fast saturable-absorber-like mode-locking techniques by a straightforward extension of the fast saturable absorber mode-locking model.

Meanwhile, refinements in the design and optimization of various resonator parameters led to a continuous improvement in the performance of passively mode-locked dye lasers. A major development was that of colliding-pulse mode-locking (CPM) in a ring laser which generated 90 fs pulses [26]. In this system, there were two dye jets, one to provide the gain and the other to act as a saturable absorber. Two counter-propagating pulses in a ring configuration cavity were synchronized to overlap in the saturable absorber, creating an interference pattern. The light intensity in the bright fringes of the transient grating was greater than in the individual pulses separately, such that the absorber is saturated more efficiently, shortening and stabilizing the laser pulses. As a drawback, however, CPM dye lasers suffered from a lack of tunability because the saturable absorber action, being a resonant process, occurs over a very narrow wavelength window just enough to accommodate a sub-ps pulse. As an alternative, Mourou and Sizer [27] reported 70 fs pulses from a Rh6G dye laser that was synchronously pumped and passively mode-locked using a fast recovery DQOCI saturable absorber. Unlike the CPM laser, this synchronously pumped dye laser was tunable from 590 to 615 nm and could be operated at an outstanding 10% overall efficiency.

CW passively mode-locked femtosecond dye lasers usually produce tens of milliwatts of average output power and their tuning capabilities are quite limited such that they cannot be used in applications needing broad wavelength ranges and in experiments requiring high powers. Furthermore, the lack of robustness, the bleaching of the dye and their toxic nature pose severe problems. As a laboratory tool, however, they enjoyed a privileged position until the field of ultrafast optics was revolutionized by the advent of the hybridly mode locked tunable solid-state lasers.

2.3.3 Passive mode-locking with quantum well saturable absorbers

In the near-infrared, saturable absorbers alternative to organic dyes can be provided by semiconductor materials, in particular with multiple quantum well (QW) structures. The current development of molecular beam epitaxy (MBE) has allowed many novel multi-layer semiconductors to be grown. Various QW structures exhibit low saturation energies and have been used to generate cw mode-locked pulse train for solid-state laser media.

A QW structure consists of alternate layers of semiconductor materials less than a few 10 nanometer thick with slightly different dopant concentrations such that adjacent strata have different electrical properties. Electrons are not able to move freely between the layers and the confinement on a nanometer scale leads to the development of quantized energy levels. By precise control of the dopant concentrations and layer thicknesses, the energy level gap associated with the quantized levels can be engineered as required to coincide with the gain bandwidth of laser media at near to mid- infrared wavelengths. The density of charge carriers in the semiconductor layers can also be controlled by adjusting the dopant concentration such that the optical flux saturation threshold can be designed to give an optimal saturable absorption performance in a compact and convenient solid-state unit.

QW structures actually exhibit two distinct absorption recombination times. First, the semiconductor upper state lifetime varies from a few tens of ps to ns, depending on the purity of the material and on the precise growth conditions. The second lifetime is of the order of 300 fs and arises from the recovery of the absorption due to the thermalization of the excitons which also contributes to the absorption. Typically, a QW absorber with a carrier recombination time of hundreds of ps is readily saturated by the radiation in a cw solid-state laser cavity. CW pulse trains are formed without the pulse energy growing sufficiently to deplete the gain of the laser gain medium below the threshold, hence causing Q-switching. A ~100 ps pulse is thus formed. It has sufficient intensity to saturate the excitonic absorption corresponding to the ~300 fs thermalization time and this saturable absorption can then compress the ps pulses down to a few 100 fs or to the limit

set by the gain bandwidth. This technique has been successfully applied to colour centre lasers [28], fibre lasers [29], Ti:sapphire lasers [30] and Cr:LiSAF lasers [31].

Recently, there has been much interest in mode-locking vibronic solid-state laser media using techniques which simulate the action of a fast saturable absorber with a recovery time of ~1 fs. These techniques exploit the optical Kerr effect to introduce an essentially instantaneous intensity-dependent loss mechanism in the laser, as discussed in the following subsection.

2.3.4   Kerr-lens mode-locking

Kerr-lens mode-locking (KLM) uses the self-focusing effect generated through the optical Kerr effect in conjunction with an aperture to produce an ultrafast saturable absorber action in a laser cavity. The Kerr effect is non-resonant (i.e. wavelength independent) such that the technique can be used in the visible and near infrared regions to generate widely tunable femtosecond pulses.

The Kerr effect arises from the aharmonic motions of bound electrons in a medium under the influence of an intense propagating electric field. It can be viewed as a nonlinear intensity-dependent contribution to the refractive index as

$$n(r,t) = n_0 + n_2 I(r,t) \qquad \text{Eq.2.7}$$

where I is the intensity of the propagating electromagnetic field and n_2 (cm^2/W) is the nonlinear index of refraction related to the third-order dielectric susceptibility $\chi^{(3)}$ of the medium.

Self-focusing occurs in the spatial domain and exploits the fact that the laser beam profile, usually a Gaussian TEM$_{00}$ mode, experiences a changing refractive-index profile across its diameter. This is analogous to propagation in a graded-index lens and results in focusing. KLM was first experimentally observed in a Ti:sapphire laser [32] and first explained in terms of self-focusing by Piché [33] and Negus et al. [34].

To obtain a simplified understanding of how KLM works, we refer to Fig. 2.3, showing the variation of the pump and laser beam profiles inside the gain crystal of a longitudinally-pumped solid-state laser. For high intensity (pulsed) radiation the effects of

self-focusing produces a narrower beam waist at the focus of lens L_1 than would otherwise be obtained, and for the asymmetric beam waist shown above, to particularly collimate the output beam (shown by the solid line). The lower intensity (cw) radiation is not focused to such a small beam waist in the laser rod and is not fully collimated after passing through the second lens L_2 (dashed line). If a hard aperture of the right size is placed after the second lens L_2, it can favor the oscillation of the high intensity beam by creating more passive loss for the low-intensity (cw) beam. It should be noted that the presence of a hard aperture is usually not necessary since the spatial gain set up by the pump beam itself (shown as dotted area) can provide enough aperture (the so-called soft aperture) to give more gain for the self-focusing high-intensity beam. Thus a pulse circulating in the cavity will experience a lower loss, or a higher gain, than a less intense pulse or a cw signal, resulting in mode-locked operation.

After repeatable results were obtained by several groups [35-39], KLM, also known as self-mode-locking, soon became the preferred method for the generation of ultrashort optical pulses. It was applied to a large number of other tunable solid-state lasers, such as Nd:YLF [40], Cr:LiSAF [41], Cr:forsterite [42-43], Nd:YAG [44], Cr:LiCAF [45], NaCl:OH⁻ [46] and Cr^{4+}:YAG [47].

Fig. 2.4 illustrates a typical KLM Ti:Sapphire laser in which the laser rod acts as the self-focusing element. The prism pair provides the adjustable intracavity group-velocity dispersion (GVD) compensation to be discussed in Section 2.5. KLM has been observed with and without intracavity negative GVD compensation. In the latter case, however, the excess positive chirp acquired by the pulses as a result of self-phase modulation gives rise to non-transform-limited pulse formation. By providing negative GVD such as in the CPM dye laser, much shorter transform-limited pulses may be obtained [48].

Due to the short interaction length, relatively high powers are required to generate sufficient nonlinear phase change for a significant amplitude modulation. Therefore, KLM requires higher pump powers and mode-locking is hard to initiate. Usually KLM lasers are not self-starting since the initial intensity fluctuations in the laser cavity are not strong enough to generate a sufficient nonlinearity so as to produce stable pulse trains. Some kind of jump-start initiation technique is required to provoke the initial intensity conditions
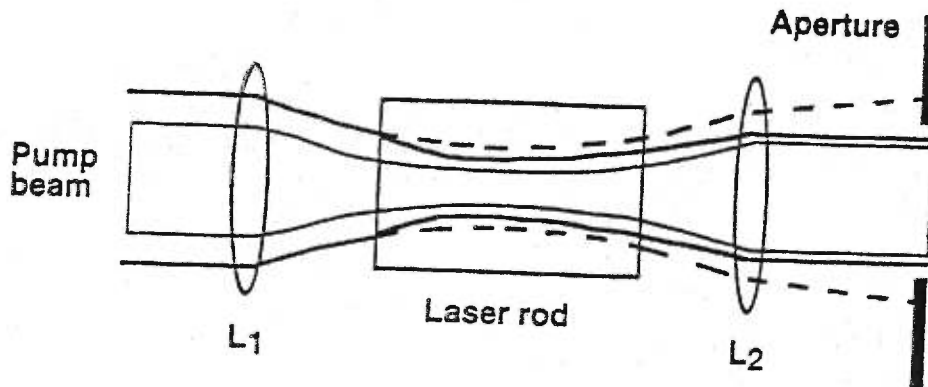
Fig.2.3 Schematic of KLM. The solid line represents the high intensity pulsed radiation, the dashed line the low-intensity radiation.
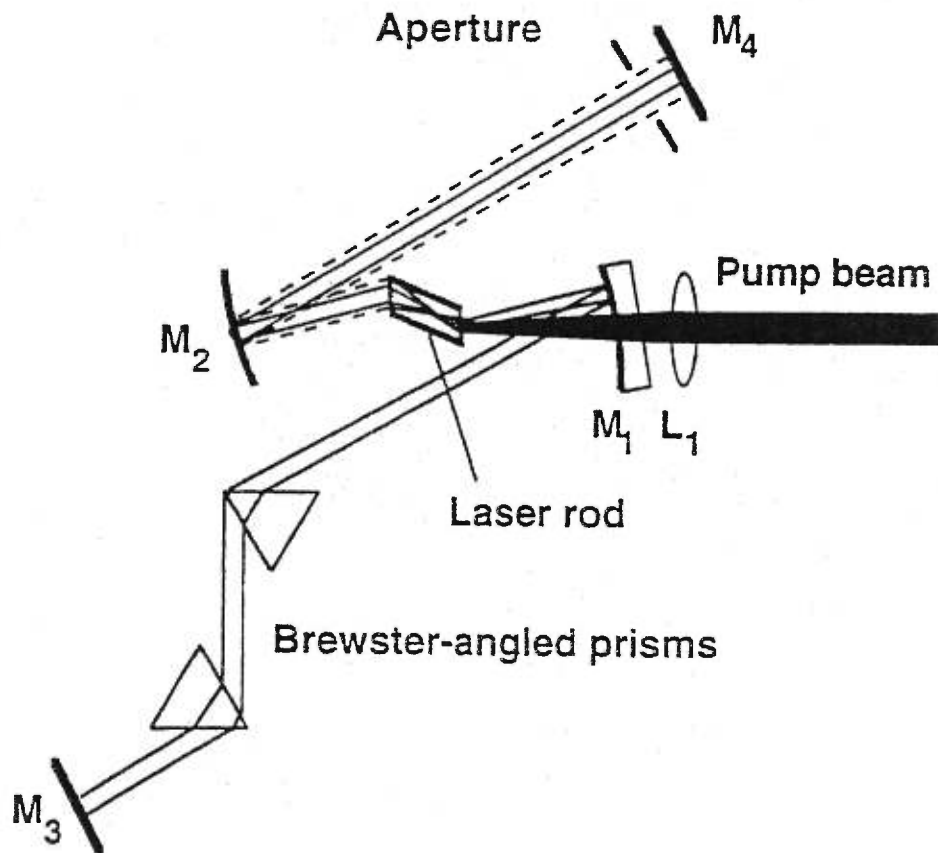
Fig.2.4 Schematic of KLM Ti:sapphire laser. Solid line represents the high intensity pulsed radiation, the dashed line the low-intensity radiation.

necessary for the onset of nonlinear pulse shaping. This will be considered in the scheme of hybrid mode-locking in the following subsection.

2.4 Hybrid passive mode-locking

Hybrid mode-locking combines the action of a saturable absorber and loss or gain modualtion in the same laser system. This represents a compromise between active and passive mode-locking, and benefits from some of the advantages of both approaches but shares some of the difficulties – notably the need to match the cavity length to the driving signal frequency. Generally, hybrid mode-locking does not represent a distinct class of mode-locking and will not generate pulses shorter than those obtainable with passive mode-locking.

As discussed in Section 2.3.2, the synchronous pumping of a dye laser containing both a saturable amplifier and saturable absorber dye enables various dye laser systems to be mode-locked by the action of gain and absorption saturation which would not otherwise be possible. Synchronous pumping produces a sufficiently intense pulse which saturates more strongly the amplifier/absortion medium than the intensity fluctuations of the free-running laser. This permits the use of dye combinations whose saturation parameters preclude their operation in a standard passively mode-locked laser with a slow saturable absorber. This technique therefore extends the spectral coverage of cw mode-locked lasers. It also tends to produce higher pulse energies than those produced by pure passive mode-locking. Reference [49] provides a review of hybrid mode-locked dye lasers.

For tunable solid-state lasers, hybrid mode-locking usually refers to the presence of an active mode-locking mechanism which is used to initially generate pulses of sufficient intensity to include the optical Kerr effect. As discussed in the previous section, KLM is not self-starting, although it is self-sustaining. Some kind of fire-up technique is required to initiate mode-locking and to form pulses which are then sufficiently short and energetic to cause the Kerr nonlinearity and induce KLM. A variety of initiation techniques have been suggested to start mode-locking in lasers with KLM, including acoustic-optic modulation [50-51], regenerative mode-locking [52], synchronous pumping [53], moving-

32

mirror mode-locking with an external cavity [54], and QW saturable absorpion in a resonant external cavity [55], or in the main laser cavity [56].

2.5 Group-velocity dispersion compensation

A series of experiments performed with passively mode-locked dye lasers show that negative dispersion and the nonlinear interaction of the pulses with the gain medium could, in addition to gain dynamics and saturation, aid in short-pulse generation [57-58]. In particular, Dietel et al. [58] reported that an optimum amount of negative dispersion provided by an intracavity prism gives rise to an increased pulse compression, obtaining 50-fs pulses from an Rh6G dye laser, passively mode-locked using a DODCI saturable absorber. With the growing experimental evidence suggesting the importance of the interplay between negative dispersion and gain medium nonlinearities, Martinez et al. [59-60] analyzed saturable-absorber mode-locking in the presence of Kerr-nonlinearity-induced self-phase modulation and negative dispersion. Their results showed that a proper balance of the two effects can give rise to soliton-type pulse formation with shorter pulse-widths in a manner similar to the formation of solitons in an optical fibre [61].

The following two subsections provide a qualitative description of dispersion and self-phase modulation and show how each affects the properties of a propagating pulse. It is shown that a correct amount of negative dispersion can cause a significant cancellation of the positive chirp acquired by such pulses as a result of self-phase modulation. Though sketchy, this simplified picture helps show the importance of negative dispersion in mode-locked lasers. The technique of adding an adjusting amount of negative dispersion in a mode-locked laser cavity to balance the otherwise positively chirped pulses has become known as GVD compensation. For references, see [61-64] for a more thorough treatment of both subjects.

2.5.1 Group velocity dispersion

In general, a dielectric medium has many characteristic resonance wavelengths in the neighbourhood of which an electromagnetic wave interacting with the bound electrons of the system will be absorbed. The wavelength-dependent absorption of the medium in turn gives rise to a wavelength-dependent index of refraction, the two effects being quantitatively related through the Kramers-Kronig relation. Dispersion results from the wavelength dependence of the index of refraction and has a crucial influence on the propagation of ultrashort pulses in such a medium. In many cases, away from the resonance wavelengths, the refractive index $n(\lambda)$ can be accurately represented by the Sellmeier equation which accounts for the various medium resonances and their strengths according to

$$n^2(\lambda) = 1 + \sum_i \frac{B_i \lambda^2}{\lambda^2 - \lambda_i^2}$$ Eq.2.8

In Eq.2.8, B_i and λ_i give the strength and the wavelength of the ith resonance, respectively, and λ is the vacuum wavelength of the electromagnetic wave. Other empirical equations giving an accurate fit of the refractive index as a function of wavelength exist, a popular one being the standard Schott glass formula which is of the form

$$n^2(\lambda) = A_0 + A_1 \lambda^2 + A_2 \lambda^{-2} + A_3 \lambda^{-4} + A_4 \lambda^{-6} + A_5 \lambda^{-8}$$ Eq.2.9

In Eqs.2.8 and 2.9, the coefficients B_i and A_i are calculated by applying a least-squared fitting routine to experimentally obtained data. Both forms of the dispersion equations are frequently used for characterizing the dispersive properties of a dielectric medium. Appendix I lists the dispersion equations for some of the materials used in various occasions in this thesis.

The wavelength dependence of n causes pulses having different carrier wavelengths to travel at different group velocities v_g given by

$$v_g = \frac{d\omega}{dk} = \frac{c}{n - \lambda \dfrac{dn}{dk}}$$ Eq.2.10

where c is the speed of light. k is the real part of the complex wavevector which is related to the refractive index by

$$k(\lambda) = \frac{2\pi n(\lambda)}{\lambda} \quad \text{or} \quad k(\omega) = \frac{\omega n(\omega)}{c} \qquad \text{Eq.2.11}$$

The term $\lambda dn / dk$ in Eq.2.10 gives the correction term and determines the extent to which the group velocity departs from the phase velocity (c/n) in the medium. Another direct consequence of this wavelength dependence of n is the fact that for a pulse having a sufficiently large wavelength bandwidth, different spectral components will travel at different group velocities.

The effect of dispersion on a light pulse can be simply considered in terms of the dispersion of the group delay of the different frequency components. The group delay of light as a function of angular frequency after propagation through a medium of length L is given by $T(\lambda)$ where

$$T(\lambda) = \frac{L}{v_g} = L\frac{dk}{d\omega} = -\frac{d\phi}{d\omega} \qquad \text{Eq.2.12}$$

Note that the phase change experienced by an electromagnetic wave of the form $e^{i(\omega t - kL)}$ on the propagation through a medium of length L is given by $\phi(\omega) = -\omega n(\omega) L / c$. The group delay is thus given by $-d\phi/d\omega$.

For a pulse of bandwidth $\Delta\omega = 2\pi\Delta\nu$, the dispersion, defined as *pulse broadening/unit bandwidth*, comes from the spread in propagation time of the frequency components of the light pulses and is given by

$$\frac{\Delta t}{\Delta\omega} = L\frac{dT(\omega)}{d\omega} = L\frac{d^2k}{d\omega^2} = -\frac{d^2\phi}{d\omega^2} \qquad \text{Eq.2.13}$$

$d^2k/d\omega^2 > 0$ ($d^2\phi/d\omega^2 < 0$) is often called *normal* dispersion while anomalous dispersion corresponds to the case when $d^2k/d\omega^2 < 0$ ($d^2\phi/d\omega^2 > 0$).

GVD is often defined with respect to wavelength and in particular is characterized by using the dispersion parameter, D (*GVD/unit length*). For optical fibres, it is common to

35

quote dispersion (i.e. D) in units of ps/(nm·km). Thus the D parameter is positive for normal dispersion (i.e., $d^2k/d\omega^2 > 0$).

$$\frac{\Delta t}{\Delta \lambda} = LD = \frac{d^2}{d\omega^2}T(\omega) = L\frac{\lambda}{c}\frac{d^2n}{d\lambda^2} = L\frac{\omega}{\lambda}\frac{d^2k}{d\omega^2} = -\frac{\omega}{\lambda}\frac{d^2\phi}{d\omega^2} \qquad \text{Eq.2.14}$$

Eqs.2.13 and 2.14 can thus be used for a rough estimate of the degree of broadening experienced by a pulse once the dispersion of a medium is known.

It should be noted that the frequency-dependent phase shift, $\phi(\omega)$, experienced by the light propagating through the medium may be expanded about the central frequency ω_0 using the Taylor expansion:

$$\phi(\omega) = \phi(\omega_0) + \frac{d\phi}{d\omega}(\omega - \omega_0) + \frac{1}{2}\frac{d^2\phi}{d\omega^2}(\omega - \omega_0)^2 + \frac{1}{6}\frac{d^3\phi}{d\omega^3}(\omega - \omega_0)^3 + ... \quad \text{Eq.2.15}$$

For most situations, it is only necessary to consider terms up to $d^2\phi/d\omega^2$ and that is what is generally meant by 'dispersion' in the context of ultrafast lasers. For extremely short pulses (<~50 fs) with correspondingly broad bandwidths, the third order dispersion term may be significant. Also, at the wavelength for which $d^2\phi/d\omega^2 = 0$, the third order term is significant. For instance, this is particularly relevant for the case of optical transmission in silica glass fibres near ~ 1.3 μm.

For a Gaussian pulse, it is straightforward to calculate the change in pulse profile more precisely. Consider a Gaussian pulse of width τ_{in} and central frequency $\omega_0 = 2\pi\nu_0$ described by:

$$E_{in} = E_0 e^{-2(\ln 2)t^2/\tau_{in}^2} e^{i\omega_0 t} \qquad \text{Eq.2.16}$$

To calculate the effect of dispersion, Eq.2.16 is Fourier-transformed to the frequency domain and the appropriate contribution from Eq.2.13 is added to the phase. Transforming back to the time domain gives the resulting output (dispersion) profile which produces a frequency chirp of sign opposite to $d^2\phi/d\omega^2$. The pulse broadening after propagating a distance L will be given by

$$\tau_{out} = \tau_{in}\sqrt{1 + (\frac{L}{L_D})^2} \qquad \text{Eq.2.17}$$

36

where

$$L_D = \frac{\pi c \tau_{in}^2}{2(\ln 2)\lambda^2 \, |D|}$$ Eq.2.18

In Eq.2.18, L_D is the characteristic 'dispersion length', defined as the length over which the pulse duration increases by a factor of $\sqrt{2}$. As can be seen from these relations, the shorter the initial pulsewidth, the more dramatic the resulting broadening due to GVD. As a matter of fact, even though the given equations apply to the case of a pulse with a Gaussian envelope, the qualitative features are the same for most pulse profiles.

Viewed in the frequency domain, the Fourier transform of the pulse acquires a dispersion–induced phase shift but keeps its original envelope and hence the original frequency bandwidth. Fig. 2.5 shows the change in the temporal and spectral profiles of a Gaussian pulse after propagation through a medium of length L and refractive index $n(\lambda)$. Notice that the temporal profile changes while the spectral profile is unchanged. Thus the dispersion broadening occuring in the time domain causes the pulse to be no longer transform-limited.
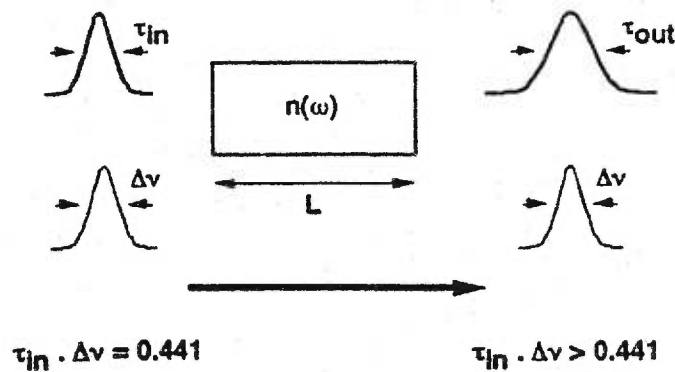
Fig. 2.5 Schematic of the broadening of a Gaussian pulse due to dispersion.

It should be noted that the time-varying phase shift results from the emergence of a modified instantaneous carrier frequency ω across the temporal extend of the pulse, given by

$$\omega = \omega_0 + \frac{4\sqrt{\ln 2}\, \text{sgn}(D)\dfrac{L}{L_D}}{1 + (\dfrac{L}{L_D})^2}\frac{\tau_{out}}{\tau_{in}} \qquad\qquad \text{Eq.2.19}$$

where ω_0 is the original carrier frequency of the propagating pulse and other variables are as defined previously in Eq.2.14, and Eqs.2.16 to 2.18. As shown in Eq.2.19, the pulse propagating in the dispersive medium acquires a linear frequency chirp whose sign follows the sign of the dispersion parameter. As will be discussed in the following section, the induced chirp in the case of negative dispersion may be exploited to balance the positive chirp of a self-phase modulated pulse, aiding in shortening the pulse.

2.5.2   Self-phase modulation (SPM)

Self-phase modulation arises from the Kerr effect in the temporal domain as described in Eq.2.7. If one considers a pulse, it is clear that the peak of the pulse will be more intense, and therefore experience a higher refractive index than the wings. It is then possible for ultrashort pulses to experience an intensity-dependent nonlinear phase-shift. The derivative of phase with respect to time is frequency such that SPM induces pulses with frequency sweeps or 'chirp'.

Consider a pulse with an intensity profile $I(t)$, propagating through a nonlinear medium of length L. In addition to accumulating the usual linear phase ϕ_0, the light will also experience a nonlinear phase change which will be proportional to the intensity profile of the pulse i.e.,

$$\phi = \phi_0 + \Delta\phi = -n\frac{2\pi}{\lambda}L = -(n_0 + n_2 I(t))\frac{2\pi}{\lambda}L \qquad\qquad \text{Eq.2.20}$$

The pulse will therefore acquire a phase profile $\Delta\phi = -\dfrac{2\pi}{\lambda}n_2 I(t)L$. The first derivative of this phase corresponds to a local change in frequency.

$$\delta\omega = \frac{d}{dt}\Delta\phi = -n_2\frac{2\pi}{\lambda}L\frac{dI(t)}{dt} \qquad\qquad \text{Eq.2.21}$$

From Eq.2.21, the instantaneous frequency chirp, $\delta\omega(t)$, will be proportional to $-dI(t)/dt$. Thus for the front of the pulse where the medium experiences an increase of intensity with time, $\delta\omega$ will be negative such that the light will shift to a lower frequency. At the peak of the pulse $dI(t)/dt = 0$ and there will be no frequency shift. At the back of the pulse the medium will experience a decrease of intensity with time and $\delta\omega$ will be positive. Therefore, there will be a sweep of frequencies from low to high across the temporal profile of the pulse. This is described as a "positive chirp" and occurs for media which have a positive n_2.

It should be understood that while GVD produces a linear frequency chirp by effectively redistributing in time the various frequency components of an optical signal, SPM produces a nonlinear frequency chirp by shifting some of the frequency components to new frequencies. Thus photons at new frequencies are created and the spectral width of the optical signal is increased. For geometries which maintain a constant beam size (and therefore a constant intensity I) over the interaction length, one can estimate the increase in spectral width of an initially unchirped signal by

$$\Delta\omega = \Delta\omega_0 \sqrt{1 + \frac{L}{L_{NL}}} \qquad \text{Eq.2.22}$$

where $\Delta\omega_0$ is the initial width which is inversely related to the pulse duration. L_{NL} is the characteristic "non-linear length", defined as the length over which the spectral width of a pulse increases by a factor of $\sqrt{2}$ due to SPM.

$$L_{NL} = \frac{\lambda}{n_2(2\pi)I} \qquad \text{Eq.2.23}$$

When a pulse propagates through a length L of nonlinear medium with an intensity such that $L \gg L_{NL}$, it will exhibit a strong nonlinear spectral broadening due to SPM.

Fig. 2.6 shows the effect of SPM on the changes in the spectral and temporal profiles of a Gaussian pulse after propagation through a nonlinear medium of length L. Without the presence of dispersion, SPM alone maintains the original temporal shape of the pulse but generates new frequency components, effectively increasing the bandwidth of the pulse.
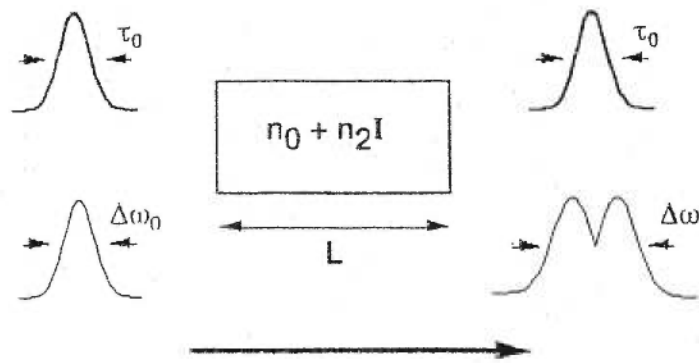
Fig. 2.6 Schematic of the broadening of a Gaussian pulse due to SPM.

2.5.3   Pulse compression using SPM and GVD

The control of GVD inside the laser cavity is the crucial step in the development of femtosecond lasers. In particular, ultrashort pulses have correspondingly broad spectral profiles and are thus sensitive to dispersion phenomena.

Standard optical media, such as silica glass and many gain media such as Cr^{4+}:YAG, exhibit "*normal*" dispersion for visible light, which corresponds to the situation where higher frequencies travel slower than lower frequencies. An initially unchirped (i.e., transformed limited) optical pulse will therefore become positively chirped after propagating through such a medium. If this positively chirped signal then propagates in a medium which exhibits negative GVD (i.e., *anomalous* $d^2k/d\omega^2 < 0$) such that higher frequencies travel faster than low frequencies, then the back of the pulse will travel faster than the front and will tend to "catch up". This results in pulse compression and is schematically illustrated in Fig. 2.7.

The essential role of negative dispersion in generating transformed limited pulses may be qualitatively understood by considering the chirp acquired as a result of these two processes. Fig. 2.8(a) shows the linear chirp due to the GVD (refer to Eq.2.19) and the positive chirp due to SPM (proportional to $-dI(t)/dt$) (dark line). Fig. 2.8(b) shows that the resultant chirp (dark line) due to the two processes can be cancelled across a major

portion of the pulse (dashed line) provided that the magnitude of the added dispersion is correct. As a result of this GVD compensation, the increased spectral bandwidth due to SPM can become effectively unchirped to produce the shortest possible pulses from a mode-locked laser.
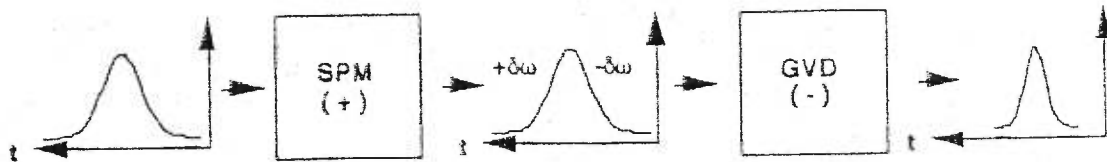
Fig. 2.7 Schematic of nonlinear optical pulse compression.

In mode-locked laser cavities, there is usually sufficient peak power to induce significant SPM and the interaction of SPM and GVD is what determines the final steady state of the laser. One way of obtaining a controlled amount of negative dispersion is by employing a prism pair [65]. In such a contribution, a longer wavelength pulse will take a longer transit time compared to a lower wavelength pulse, hence always giving rise to a net negative dispersion contribution. Furthermore, the amount of dispersion can be adjusted by varying the prism separation and material. Specific details of how the negative dispersion depends on the configuration of the prism pair can be found in Chapter 5.
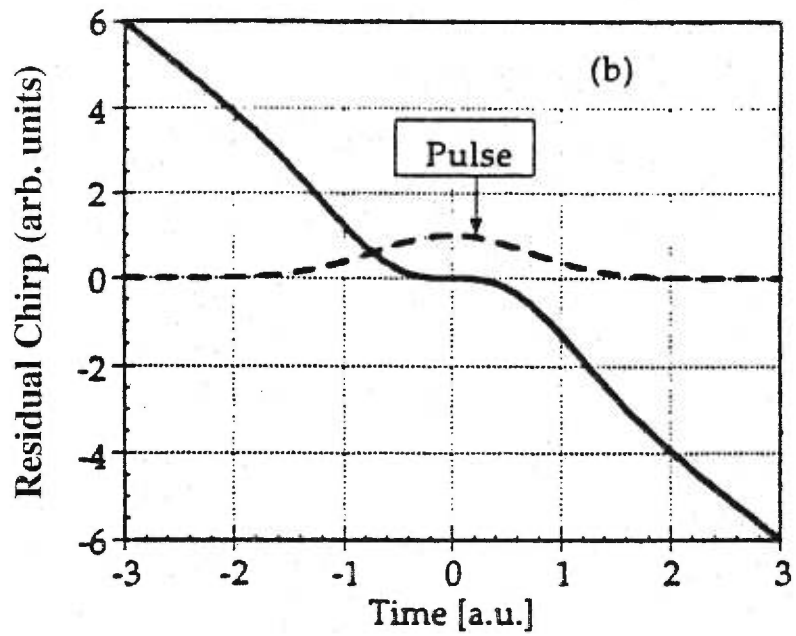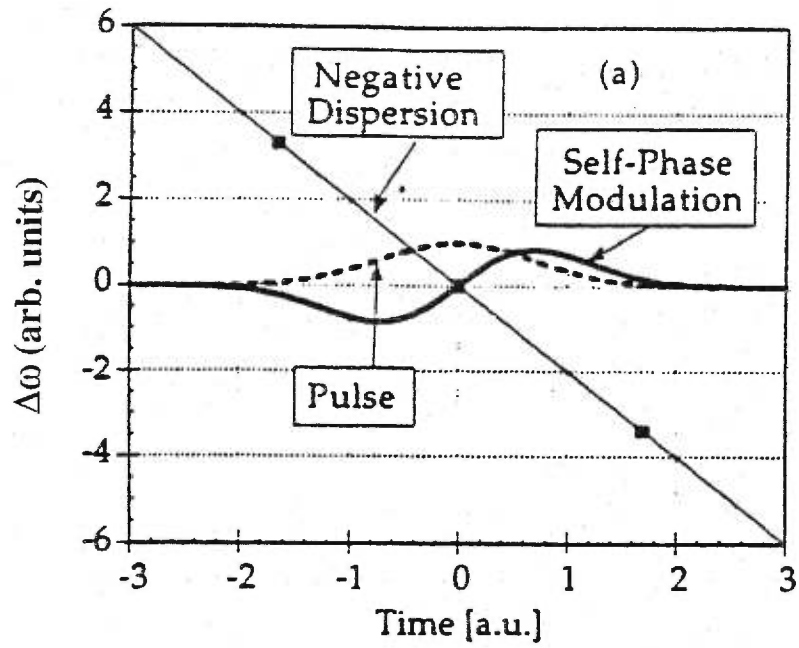
Fig.2.8 (a) Chirp caused by negative dispersion and SPM and (b) resulting residual chirp.

2.6 Conclusions

In this chapter, a highly condensed version of laser mode-locking techniques used in the past three decades has been given.

Among the various ultrafast pulse-generation schemes, it was noted that KLM turns out to be superior. The versatility of this technique and the concurrent development of tunable solid-state lasers paved the way for an unprecedented development and research efforts in this field. One called it the "ultrafast revolution" [66] and others the renaissance of modern-day laser engineering [6]. From the experimentalist's point of view, the simplicity of the technique makes it possible to build sophisticated ultrashort sources with a gain medium and a prism pair. The most recent trends have been in the directions of searching for new gain media to reach out to new spectral regions [67-68] and producing the shortest possible pulses from already mode-locked lasers by minimization of higher-oder phase distortions [69-71]. As to the Ti:sapphire laser, higher-order phase distortion minimization resulted in the direct production of pulses as short as 11 fs [71-72]. Furthermore, with the dispersion compensation with a prism pair in combination with improved doubled chirped mirrors, self-starting 6.5 fs pulses from a KLM mode-locked Ti:sapphire laser were demonstrated [73], which are nearly gain-bandwidth limited.

The race still continues in the field of ultrafast optics. A major part of ultrafast laser development in the near future will be to develop useful compact practical devices appropriate to real world applications. As described in previous subsections, KLM is extremely sensitive to alignment and in general is not self-starting though self-sustaining. An alternative method of mode-locking has received increasing attention, which relies on a semiconductor quantum-well-structure with a Bragg reflector, the so-called saturable Bragg reflector (SBR) [74]. Lasing with SBR is always accompanied by self-starting mode-locking. In constrast to KLM, this technique works over the full stability regime, and no critical cavity adjustments are necessary.

A very recently demonstrated method of providing negative GVD is the careful design of the dielectric coating layers of mirrors [75], hence eliminating the need for a prism pair. Using this mirror-dispersion–controlled resonator design, pulses as short as

11-fs have been produced from a Ti:sapphire laser [76]. Such an idea can also be extended to chirped SBR mirrors that combine both saturable absorption and negative GVD in a simple SBR structure as one intracavity element [77]. In the coming future, a possible consequence of such a design may be the development of scaled-down solid-state femtosecond lasers, as small as the size of a shoebox.

2.7 References

1. Hargrove L.E., Fork R.L. and Polock M.A., Appl. Phys. Lett. **5**, 4 (1964).

2. Smith P.W., *"Mode-locking of lasers"*, Proc. IEEE **58**, 1342 (1970).

3. DeMaria A.J., Glenn W.H., Brieniza M.J. and Marck M.E., *"Picosecond laser pulses"*, Proc. IEEE **57**, 2 (1969).

4. Siegman A.E. and Knizenga D.J., *"Active mode-locking phenomena in pulse and continous lasers"*, Opto-electronics **6**, 43 (1974).

5. Fork R.L., Shank C.V., Yen R. and Hirlimann C.A., IEEE J. Quantum Electron. **19**, 500 (1983).

6. Krausz F., Fermann M.F., Brabec J., Curley P.F., Hofer M., Ober M.H., Spielmann Ch., Wintner E. and Schmidt A.J., IEEE J. Quantum Electron. **28**, 2097 (1992).

7. French P.M.W., *"The generation of ultrashort laser pulses"*, Rep. Prog. Phys. **58**, 169 –267 (1995); *"Ultrafast solid-state lasers"*, Comtemp. Phys. **7**, 283-301 (1996).

8. DiDomenico M.Jr., J. Appl. Phys. **35**, 2870 (1964).

9. Kuhl J., Opt. Lett. **12**, 334-6 (1987).

10. Kuizenga D.J. and Siegman A.E., IEEE J. Quantum Electron. **6**, 694 (1970).

11. Demaria A.J., Ferrar C.M. and Danielson G.E. Jr., Appl. Phys. Lett. **8**, 22 (1966).

12. DiMomenico M. Jr., Geusic J.E., Marcos H.M., and Smith R.G., Appl. Phys. Lett. **8**, 180 (1966).

13. Crowell M.H., IEEE J. Quantum Electron. **1**, 12 (1965).

14. Dienes A., Ippen E.P. and Shank C.V., Appl. Phys. Lett. **19**, 258 (1971).

15. Pinto J.F., Yakymyshyn C.P. and Pollock C.R., Opt. Lett. **13**, 383 (1988).

16. Squier J., Salin F., Coe S., Bado P. and Mourou G., Opt. Lett. **16**, 85 (1991).

17. Seas A. Petricevic V. and Alfano R.R., Opt. Lett. **16**, 1668 (1991).

18. French P.M.W., Rizvi N.H., Taylor J.R. and Shestakov A.V., Opt. Lett. **18**, 39 (1993).

19. Mocher H.W. and Collins R.J., Appl. Phys. Lett. **7**, 270 (1966).

20. Ippen O.P., Shank C.V. and Dienes A., Appl. Phys. Lett., **21**, 348 (1972).

21. Ruddock I.S. and Bradley D.J., Appl. Phys. Lett. **29**, 296 (1976).

22. New G.H.C., *"Pulse evolution in mode-locking of the cw dye laser"*, IEEE J. Quantum Electron. **10**, 115 (1974).

23. Haus H.A., *"Theory of mode-locked with a fast saturable absorber"*, J. Appl. Phys. **46**, 3049 (1975).

24. Haus H.A., *"Theory of mode-locked with a slow saturable absorber"*, IEEE J. Quantum Electron. **11**, 736 (1975).

25. Haus H.A., *"Parameter ranges for cw passively mode-locked lasers"*, IEEE J. Quantum Electron. **72**, 169 (1976).

26. Fork R.L., Greence B.I. and Shank C.V., Appl. Phys. Lett. **38**, 671 (1981).

27. Mourou G.A. and Sizer T. II., Opt. Commun. **41**, 47 (1982).

28. Islam M.N., Sunderman E.R., Soccoloch C.E., Bar-Joseph I., Sauer N., Chang T.Y. and Miller B.I., IEEE J. Quantum Electron. **25**, 2454 (1989).

29. DeSouza E.A., Islam M.N., Soccolich C.E., Pleihel W., Stolen R.H., Simpson J.R. and DiGiovanni P.J., Electron. Lett. **29**, 447 (1993).

30. Mellish R., French P.M.W., Taylor J.R., Delfyett D.J. and Florez L.T., Electron. Lett. **29**, 894 (1993).

31. Mellish R., French P.M.W., Taylor J.R., Delfyett D.J. and Florez L.T., Electron. Lett. **30**, 223 (1994).

32. Spence D.E., Kean P.N. and Sibbett W., Opt. Lett. **16**, 42 (1992).

33. Piché M., Opt. Commun. **86**, 156 (1991).

34. Negus D.K., Spine U.L., Goldblatt N. and Feuguet G., *Digital Solid-State Lasers* (Hilton Heas: Sc, 1991), Paper PDP4 (Washington DC: Optical Society of America), p.120-4.

35. Negus D.K., Spinelli L., Goldblatt N. and Feugnet G., in *OSA Proceedings on Advanced Solid State Lasers*, G. Dube and L. Chase, eds., (Washington DC: Optical Society of America, 1991), **10**, p.120.

36. Gabetta G., Huang D., Jacobson J., Ramaswamy M., Ippen E.P. and Fujimoto J.G., Opt. Lett. **16**, 1756 (1991).

37. Huang C.P., Kapteyn H.C., McIntosh J.W. and Murnane M.M., Opt. Lett. **17**, 139 (1992).

38. Krausz F., Spielmann Ch., Brabec T., Winter E. and Schmidt A.J., Opt. Lett. **17**, 204 (1992).

39. Rizvi N.H., French P.M.W. and Taylor J.R., Opt. Lett. **17**, 279 (1992).

40. Malcolm G.P.A. and Ferguson A.I., Opt. Lett. **16**, 1967 (1991).

41. Miller A., LiKamWa P., Chai B.H.T., and Van Stryland E.W., Opt. Lett. **17**, 195 (1992).

42. Seas A., Petricevic V. and Alfano R.R., Opt. Lett. **17**, 937 (1992).

43. Sennaroglu A., Pollock C.R. and Nathel H., Opt. Lett. **18**, 826 (1993).

44. Liu K.X., Flood C.J., Walker D.R. and van Driel H.M., Opt. Lett. **17**, 1261 (1992).

45. LikamWa P., Chai B.H.T. and Miller A., Opt. Lett. **17**, 1438 (1992).

46. Kennedy G.T., Grant R.S. and Sibbett W., Opt. Lett. **18**, 1736 (1993).

47. Sennaroglu A., Pollock C.R. and Nathel H., Opt. Lett. **19**, 390 (1994).

48. Spence D.E., Evans J.M., Sleat W.E. and Sibbett W., Opt. Lett. **16**, 1762 (1991).

49. Diels J-C., *Femtosecond dye lasers* in *"Dye laser principles: with applications; - quantum electronics - principle and applications"*, ed. Duarte F.J. and Hillman L.L., (Academic, San Diego, CA, 1990), pp.41-132.

50. Curley P.F. and Ferguson A.I., Opt. Lett. **16**, 1016 (1991).

51. Li K.W.P., Chai B.H.T. and Miller A., Electron. Lett. **27**, 2351 (1991).

52. Kalfa J.D., Watts M.L. and Pieterse J-W.J., IEEE J. Quantum Electron. **28**, 2151 (1992).

53. Spielmann Ch., Krausz F., Brabec T., Wintner E. and Schmidt A.J., Opt. Lett. **16**, 1180 (1991).

54. Rizvi N.H., French P.M.W. and Taylor J.R., Opt. Lett., **17**, 279 (1992).

55. Keller U., 'tHooft G.W., Knox W.H. and Cunningham J.E., Opt. Lett. **16**, 1022 (1991).

56. Rizvi N.H., French P.M.W. and Taylor J.R., Opt. Lett. **18**, 983 (1993).

57. Dietel W., Dopel E., Kuhlke D. and Wilhelmi B., Opt. Commun. **43**, 433 (1982).

58. Dietel W., Fontaine J.J. and Diels J-C., Opt. Lett. **8**, 4 (1983).

59. Martinez O.E., Fork R.L. and Gordon J.P., Opt. Lett. **9**, 156 (1984).

60. Martinez O.E., Fork R.L. and Gordon J.P., J. Opt. Soc. Am. **2**, 753 (1985).

61. Hasegawa A. and Tappert F., Appl. Phys. Lett. **23**, 142 (1973).

62. Hasegawa A. and Tappert F., Appl. Phys. Lett. **23**, 171 (1973).

63. DeSilvestri de S., Laporta P. and Svelto O., IEEE J. Quantum Electron. **20**, 533 (1984).

64. Rudolph W. and Wilhelmi B. (ed.) 1989 *Light pulse compresssion.*

65. Fork R.L., Martinez O.E. and Gordon J.P., Opt. Lett. **9**, 150 (1984).

66. Knox W.H., "The revolution in femtosecond near-infrared pulse generation", Optics and Photonics News **3**, 10 (1992).

67. Petricevic V., Gayen S.K., Alfano R.R., Yamagishi K., Anzai H. and Yamagushi Y., Appl. Phys. Lett. **52**, 1040 (1988).

68. Angert N.B., Borodin N.I., Garmash V.M., Zhitnynk V.A., Okhrimchuk A.G., Siyuchenko O.G. and Shestakov A.V., Sov. J. Quantum Electron. **18**, 73 (1988).

69. Huang C.P., Asaka M.T., Backus S., Murnane M.M., Kapteyn H.C. and Nathel N., Opt. Lett. **17**, 1298 (1992).

70. Lemoff B.E. and Barty C.P.J., Opt. Lett. **18**, 57 (1993).

71. Asaka M.T., Huang C.P., Garvey G., Zhou J., Kapteyn H.C. and Murnane M.M, Opt. Lett. **18**, 977 (1993).

72. Xu L., Spielmann C., Krausz F. and Szipocs R., Opt. Lett. **21**, 1259 (1996).

73. Jung I.D., Kartner F.X., Matuschek N., Sutter D.H., Morier-Genoud F, Keller U., Tilsch M. and Tschudi T., Opt. Lett. **22**, 1009 (1997).

74. Tsuda S., Knox W.H., de Souza E.A., Jan W.Y. and Cunningham J.E., Opt. Lett. **20**, 1406 (1995).

75. Szipocs R., Ferencz K., Spielmann Ch. and Krausz F., Opt. Lett. **19**, 201 (1994).

76. Stingl A., Spielmann Ch., Krausz F. and Szipocs R., Opt. Lett. **19**, 204 (1994).

77. Kopf D., Zhang G., Fluch R., Mose M. and Keller U., Opt. Lett. **21**, 486 (1996).

Chapter 3

Excited-state absorption (ESA) of Cr^{4+} in the Cr^{4+}:YAG gain medium

We theoretically investigate the spectroscopic and lasing properties of a Cr^{4+}:YAG gain medium, which is of interest for near-infrared (**NIR**) tunable laser applications. The crystal-field energy levels for the Cr^{4+} ions in the D_{2d} site symmetry in the YAG lattice are investigated by diagonalizing the Hamiltonian matrices including the electrostatic term, the Trees correction and the crystal-field interaction. It is shown that the strong NIR absorption around 1000 nm is due to transitions from the ground state to the $^3A_1(^3T_1)$ state. The excited-state absorption transitions at the pump and lasing wavelengths are investigated. The zero-field splitting for the ground state is also considered taking into account the spin-orbit coupling.

3.1 Introduction

For the technologically important infrared spectral range from 1100 to 1600 nm, the tetrahedrally coordinated Cr^{4+} ion seems to be the most promising lasing ion. This fact motivates the numerous spectroscopic and laser studies of Cr-doped crystals which aim to find new laser materials as the host lattice for Cr^{4+} [1-3]. The Cr^{4+}-doped $Y_3Al_5O_{12}$ (**YAG**) laser has received considerable attention recently since it can be tuned over the 1550-nm wavelength range where the present-day low loss fiber-optic transmission systems are operated. The first tunable CW lasing of Cr^{4+}:YAG operating at room temperature was demonstrated by Shestakov et al. [4], while the first picosecond pulse generation with a high repetition rate was reported by French et al. [5].

Recent spectroscopic studies [1, 6, 7] show that the observed absorption, emission and excited-state absorption (**ESA**) transitions are difficult to assign to the Cr^{4+} energy-level scheme. Although the Cr^{4+} ion with the $3d^2$ electron configuration is the simplest non-Kramers ion among transition elements, crystal-field (**CF**) analyses of Cr^{4+} (with an unusual valence) in crystal hosts are rather scarce, in strong contrast to those of the more

common Cr^{3+}. To the best of our knowledge, the available CF analyses of Cr^{4+} in the overall cubic YAG crystal are based on the approximated cubic T_d symmetry [6, 7], although the local site symmetry for Cr^{4+} is tetragonal D_{2d}. The results relying on the Tanabe-Sugano ligand field diagrams as well as group theory considerations assuming tetrahedral (T_d) symmetry are obviously inadequate and only partially successful. Because of the large distortion of the tetrahedron, the cubic CF approximation cannot provide a full understanding of the energy level structure of the Cr^{4+} ions in YAG. For example, a large noncubic CF splitting of the $^3T_1$ energy levels of some 5000 cm^{-1} has been reported experimentally [6], which could not be interpreted in terms of the cubic approximation. Therefore, the D_{2d} site symmetry has to be considered. A CF analysis of Cr^{4+} taking into account the actual site symmetry would help in the search for new tunable laser materials based on Cr^{4+} as well as other isoelectronic ions, e.g. Mn^{5+}, Ti^{2+} and Fe^{6+} [1]. Laser action at 1181 nm from Mn^{5+} in $Ba_3(VO_4)_2$ under pulsed 592 nm excitation was demonstrated recently [8]. The Mn^{5+} ion, when stabilized in tetraoxo coordination, presents NIR emission in the 1.0-1.5 μm range [9].

The ESA at the lasing wavelengths is less studied for optically pumped lasers [10]. ESA has often been identified as being responsible for the inhibition of laser oscillation by absorbing photons at the lasing wavelengths. Many other Cr^{4+} doped materials, which exhibit broad NIR emission bands similar to that of Cr^{4+}:YAG, could not be made to lase due to a large ESA [2, 11, 12]. For a Cr^{4+}:YAG laser, ESA limits the laser efficiency performance, resulting in only a few percent saturated round-trip gain [13, 14]. There exists a large disparity between the available experimental values for the emission and ESA cross-sections. In this chapter, a detailed theoretical investigation of the ESA is presented. Later in chapter 4, a cw tunable Cr^{4+}:YAG laser system pumped with a Nd:YAG laser in the cw mode is constructed, and the laser efficiency data are used to determine the emission and ESA cross-sections.

This chapter is organized as follows. First, the room temperature absorption and emission spectra of Cr^{4+} in YAG are concisely described in Section 3.2. Second, a theoretical description of the ligand (crystal) field theory and zero-field splitting is presented. Third, crystal-field (CF) analysis for the Cr^{4+} energy-level scheme pertinent to

the laser action including the ESA transitions is analyzed. Note that, in Chapter 4, emission and ESA cross-sections for Cr^{4+} in Cr^{4+}:YAG gain medium are estimated experimentally from the laser efficiency data. Finally, a short conclusion summarizes the essential points.

3.2 Spectroscopic background

General spectroscopic studies of the laser active Cr^{4+} ion in YAG have been carried out experimentally by several groups [6, 7]. Our sample is a 20-mm-long, Brewster-cut YAG crystal rod used for constructing a cw Cr^{4+}:YAG laser (see Chapter 4). The broad absorption and emission spectra at room temperature, as shown in Fig. 3.1, arise as a consequence of the strong coupling between the vibrational and electronic energy states of Cr^{4+} ions.

The basic feature of the absorption spectrum, shown in Fig. 3.1(a), is the three broad intense spin-allowed bands with centres at approximately 480 nm (between 380 and 550 nm), 640 nm (between 550 and 780 nm) and 1000 nm (between 900 and 1100 nm). An absorption cross-section of 3×10^{-18} cm^2 at $\lambda = 1064$ nm was determined at room temperature. At a low temperature of about 12 K, the 480 nm and 640 nm bands shift to 450 nm and 650 nm, respectively, while the 1000 nm band remains almost unchanged [6].

The 640 nm and 1000 nm bands are primarily ascribed to $^3A_2 \rightarrow {}^3T_1$ and $^3A_2 \rightarrow {}^3T_2$ transitions, respectively, of the Cr^{4+} ions in the T_d approximation [2, 7]. Kück et al. [15] interpreted the strong NIR absorption centred at about 1000 nm as due to the $^3B_1(^3A_2) \rightarrow {}^3E(^3T_2)$ transition in D_{2d} symmetry. From group theory considerations, this transition into the orbital doublet is allowed in two polarization directions, in contrast with the experimental finding that the transition giving rise to the strong NIR absorption band is polarized along one of the crystallographic axes [6]. Eilers et al. [6] concluded that the two broad bands centred at 650 nm and 1000 nm are both due to the splitting of the $^3T_1$ state of T_d symmetry by D_{2d} symmetry.

(a)

(b)
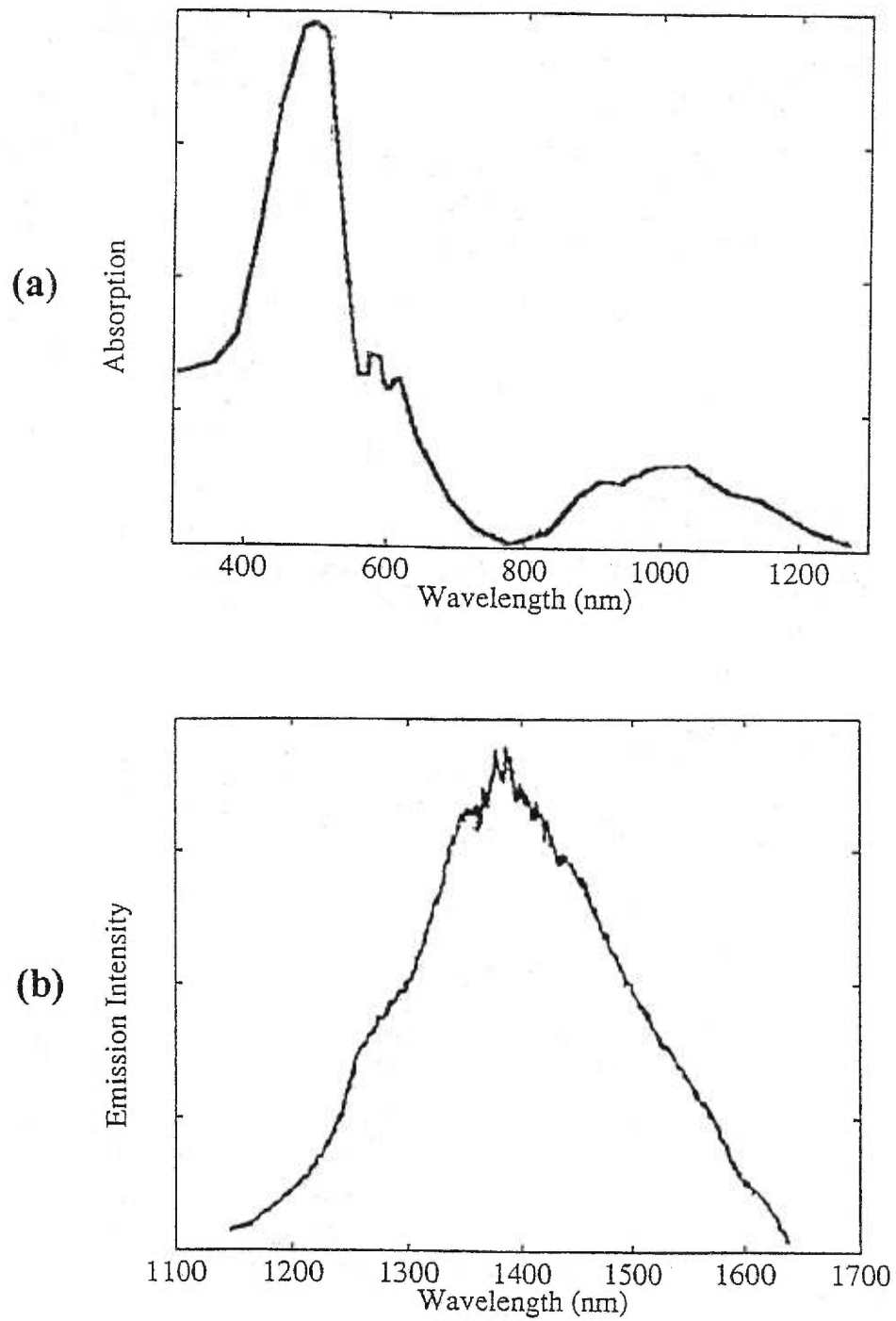
Fig. 3.1 The absorption (a) and emission (b) spectrum of Cr^{4+}:YAG laser crystal at room temperature. The emission was obtained when excited with the 1064-nm output of a Nd:YAG laser.

The strong broadband absorption around 1000 nm in Cr^{4+}:YAG agrees well with the 1064 nm output of a cw Nd:YAG laser. There is also the possibility of using InGaAs laser diodes operating at 980 nm as pump sources to build a compact, diode-pumped Cr^{4+}:YAG laser [3]. The measured unpolarized emission spectrum of Cr^{4+}:YAG taken at room temperature, shown in Fig. 3.1(b), using an excitation from a Nd:YAG laser ranges from 1100 to 1650 nm, extending over some 550 nm with a peak wavelength at 1380 nm. The fluorescence lifetime of Cr^{4+}:YAG is found to be 3.6 μs at room temperature, whereas a typical lifetime at 10 K is 30.6 μs [7]. This broadband emission is ascribed to the $^3T_2 \rightarrow$ $^3A_2$ transition in T_d symmetry, or more precisely, the $^3B_2(^3T_2) \rightarrow {}^3B_1$ transition in D_{2d} symmetry.

For the crystal structure, yttrium aluminum garnet ($Y_3Al_5O_{12}$), also known as YAG, has one Y site and two Al sites. The Y ion is dodecahedrally coordinated. Al_1 is octahedrally coordinated and Al_2 is tetrahedrally coordinated. It is now commonly believed that similar to the chromium-doped forsterite and yttrium silicate lasers, the near-infrared fluorescence is attributed to the tetravalent chromium ions as substitutional impurities in the tetrahedral Al_2 sites. The proposed configuration of the active Cr^{4+}, shown in Fig. 3.2, consists of a Cr^{4+} ion surrounded by four oxygen ions in a tetrahedral arrangement [6, 12]. This tetrahedron is distorted due to tension along the S_4 symmetry axis (z-axis in Fig. 3.2), the overall symmetry of the centre being widely accepted as D_{2d} point group.

Fig. 3.3 shows the energy levels of tetrahedrally coordinated Cr^{4+}:YAG ions with $3d^2$ electron configuration. The pump band absorption in the 0.9 to 1.1 μm wavelength region corresponds to the transition between the states $^3A_2$ and $^3T_2$. There is also an excited state absorption (ESA) at 1 μm originating from the $^3T_2$ state to the higher lying $^3T_1$ state. The laser emission in the 1.4 μm region occurs as a result of the transition from the $^3T_2$ state back to the $^3A_2$ state.
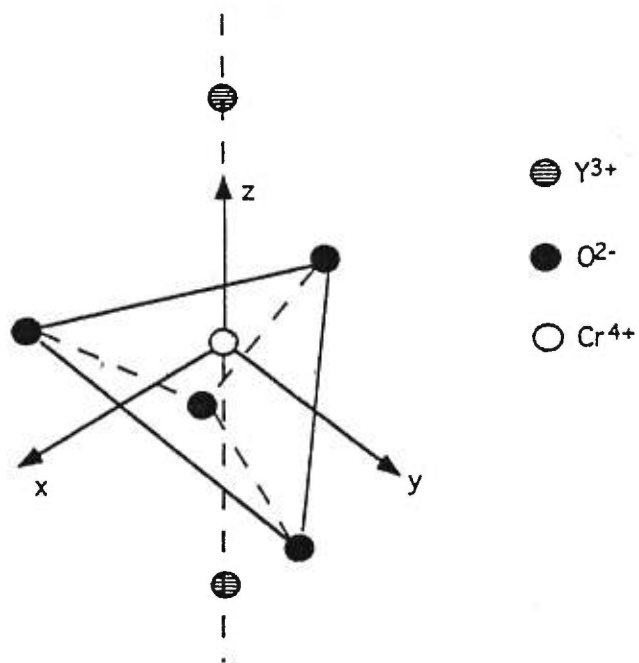
Fig. 3.2 Configuration of the Cr^{4+} ions in Cr^{4+}:YAG lattice.
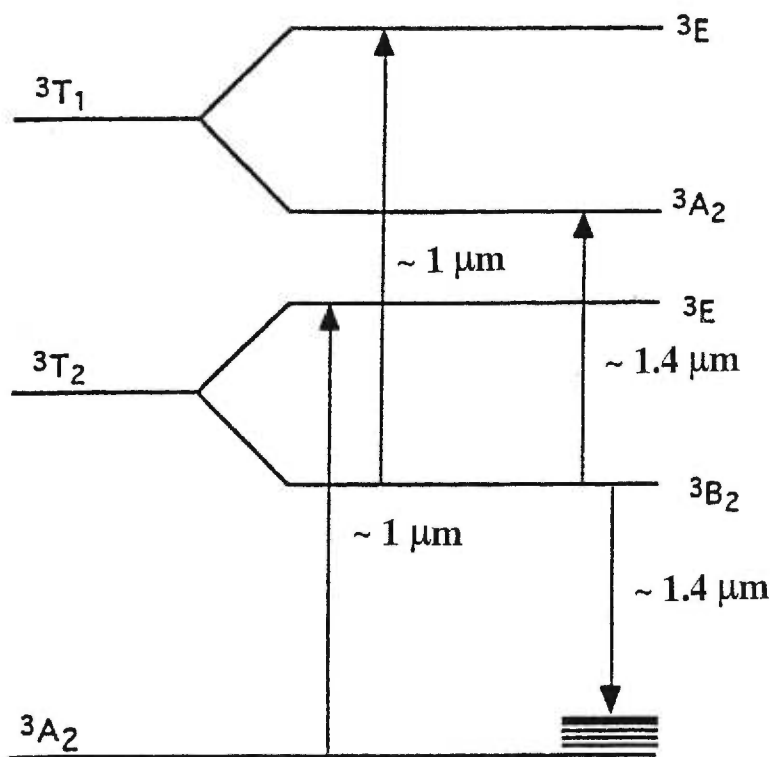
Fig. 3.3 Energy level diagram of the Cr^{4+} ion with $3d^2$ electron configuration

3.3 Ligand field theory and zero-field splitting

3.3.1 Ligand (crystal) field theory

The energy levels and state vectors of transition ions incorporated in a solid are strongly modified due to the interactions between ions and the host lattices, which depend in a complicated way on a particular ion, the symmetry and the strength of the crystal field, the spin-orbit coupling and also the hyperfine interaction of the electrons and nuclei. These interactions, however, can be parameterized in a systematic way. For the transition-metal ($3d^N$) ions, all the electronic shells except the $3d$ shell are spherically symmetric and so will not cause splittings of the energy levels. Hence, the Hamiltonian for a $3d$ ion in crystal can be written as (for detail see, e.g., Refs. 15-18)

$$H = H_{fi} + H_{CF} = H_{es} + H_{so} + H_{Trees} + H_{CF} \qquad \text{Eq.3.1}$$

The free-ion Hamiltonian H_{fi} (excluding the kinetic energy of electrons and their Coulomb attraction with the nucleus) consists of electrostatic repulsion amongst these $3d$ electrons:

$$H_{es} = \sum_{i<j}^{N} \frac{e^2}{r_{ij}} \qquad \text{Eq.3.2}$$

the spin-orbit interaction:

$$H_{so} = \sum_{i=1}^{N} \zeta(r_i) s_i \bullet l_i \qquad \text{Eq.3.3}$$

and the Trees correction $H_{Trees} = \alpha L(L+1)$ describing the two-body orbit-orbit polarization interaction (see, e.g., Ref. 17, p.54). The ligand (crystal) field Hamiltonian in Eq.3.1., in Wybourne's notation [19], is parameterized by

$$H_{CF} = \sum_{kq} B_{kq} C_q^{(k)} \qquad \text{Eq.3.4}$$

where B_{kq} are the crystal field (CF) parameters and $C_q^{(k)}$ are the renormalized spherical tensor operators. The Wybourne's B_{kq} parameters for low symmetry are complex and in general $B_{k-q} = (-1)^q B_{kq}^{*}$. Since the crystal field potential must be invariant under the operations of a given point symmetry group, the crystal field parameters are limited by the

point symmetry of the environment around an ion in the crystal. If our considerations are restricted to the states of the same parity, i.e., within one configuration $(3d^N)$ only, the rank k in Eq.3.4 will assume only even values. Non-vanishing CF parameters for 32 point groups can be found, e.g., by Morrison in Ref. 20.

Since the strength of ligand field is usually in the weak and/or intermediate range for most of the $3d$ transition metal ions in crystals, the basis of states in the LS coupling scheme is the most convenient one and can be taken as:

$$| \psi > = | d^N \alpha S M_s L M >$$

where α is an extra quantum number (seniority) and the orbital quantum number $l = d$, i.e., 2. Quantum number α specifies the states having the identical orbital and spin quantum numbers. Under the LS scheme, the matrix elements of the operators in Eq.3.1 to Eq.3.4 are evaluated by means of the irreducible tensor operator method (see, e.g., [19, 20]) as follows:

(i) The electrostatic term

$$\langle \psi | H_{es} | \psi' \rangle = \sum_k < d^N \alpha S L \| f^k \| d^N \alpha' S' L' > F^k \delta_{LL'} \delta_{SS'} \delta_{M_S M_{S'}} \delta_{MM'} \qquad \text{Eq.3.5}$$

where the two-particle tensor operators are

$$f^k = \sum_{i<j}^N C_q^{(k)}(i) C_q^{(k)}(j)$$

The reduced matrix elements $<\|f^k\|>$ are evaluated according to the following formula (see, Ref. 21, p.275):

$$\triangleleft \| f^k \| \triangleright = \frac{1}{2} < d \| C^k \| d >^2 \left\{ \frac{1}{2L+1} \sum_{\alpha''L''S''} (-1)^{L+L''} < d^N \alpha S L \| U^k \| d^N \alpha'' S'' L'' > \right.$$

$$\times < d^N \alpha'' S'' L'' \| U^k \| d^N \alpha' S' L' > - \left. \frac{N}{2L+1} \delta_{\alpha \alpha'} \right\}$$

The Slater intergrals in Eq.3.5 F^K ($k = 0$, 2, and 4) are related to the Racah parameters A, B, and C [17] as follows,

$$A = F_0 - 49 F_4 \qquad B = F_2 - 5 F_4 \qquad C = 35 F_4,$$

and $F_0 = F^0$, and $F_2 = F^2/49$, $F_4 = F^4/441$. Usually A is set to zero since it will cause no energy level splittings apart from the shifting of the centroid of the whole spectrum.

(i)   The spin-orbit term

$$\langle \psi | H_{so} | \psi' \rangle = \zeta \times (-1)^{S+L-M_S-M} < d^N \alpha SL \parallel V^{(11)} \parallel d^N \alpha' S' L'>$$

$$[(2d+1)(d+1)d] \times \sum_{kq} (-1)^q \begin{pmatrix} S & 1 & S' \\ -M_S & q & M_S' \end{pmatrix} \begin{pmatrix} L & 1 & L' \\ -M & -q & M' \end{pmatrix} \qquad \text{Eq.3.6}$$

where $(\cdots)$ denotes the 3-j symbols and $V^{(11)} = \sum_{i=1}^{N} v^{(11)}(i)$ is the double tensor operator,

whereas the reduced matrix elements $<\parallel V^{(11)} \parallel>$ are obtained as [22]

$$<\parallel V^{(11)} \parallel> = N[(2L+1)(2S+1)]^{1/2}[(2L'+1)(2S'+1)]^{1/2} \times \sqrt{3/2} \sum_{\alpha''L''S''} (-1)^{L+L''+1+S+S'+1/2}$$

$$\times \begin{pmatrix} S & S' & 1 \\ 1/2 & 1/2 & S'' \end{pmatrix} \begin{pmatrix} l & l & 1 \\ L' & L & L'' \end{pmatrix} < d^N, \alpha SL\{| d^{N-1}\alpha''S''L''> < d^N, \alpha'S'L'\{| d^{N-1}\alpha''S''L''>$$

where the cofficients of the fractional parentage $< d^N, \alpha SL\{| d^{N-1}\alpha'S'L'>$ are tabulated by Nielson and Koster [23].

(ii)   The Trees correction

$$\langle \psi | H_{Trees} | \psi' \rangle = \alpha L(L+1)\delta_{LL'}\delta_{SS'}\delta_{M_S M_S'}\delta_{MM'} \qquad \text{Eq.3.7}$$

where α is a parameter for the Trees correction and should not be confused with the extra quantum number (seniority) (see above, Eq.3.5).

The crystal field term

$$\langle \psi | H_{CF} | \psi' \rangle = \sum_{kq} B_{kq}(-1)^{L-M} \begin{pmatrix} d & k & d \\ 0 & 0 & 0 \end{pmatrix} < d^N \alpha SL \parallel V^{(11)} \parallel d^N \alpha' S' L'> \delta_{SS'}\delta_{M_S M_S'}$$

$$\text{Eq.3.8}$$

where

$$< d^N \alpha SL \parallel C^{(k)} \parallel d^N \alpha'S'L'> = (-1)^d (2d+1) \begin{pmatrix} L & k & L' \\ -M & q & M' \end{pmatrix} < d^N \alpha SL \parallel U^k \parallel d^N \alpha'S'L'>$$

and $d = 2$, whereas the reduced matrix elements $<\parallel U^k \parallel>$ for the unit tensor operator U^k are obtained as [22]:

$$\langle\| U^k \|\rangle = N[(2L+1)(2L''+1)]^{1/2} \delta_{SS'} \sum_{\alpha''L''S''} (-1)^{L+L''+d+k} \begin{pmatrix} 1 & 1 & k \\ L' & L & L'' \end{pmatrix}$$

$$\times \langle d^N, \alpha SL\{| d^{N-1} \alpha'' S'' L'' \rangle \langle d^N, \alpha' S' L'\{| d^{N-1} \alpha'' S'' L'' \rangle$$

Practically, in the computer package (see, [10-12]) the spectroscopy coefficients used above for the reduced matrix elements $\langle\|f^k\|\rangle$, $\langle\|V^{(11)}\|\rangle$, $\langle\|U^k\|\rangle$, have been calculated numerically with double precision and stored in data files to be used for further calculations.

In the analysis of the experimental results, the input parameters for the CF parameters are considered as the adjustable parameters, which are varied to obtain the best agreement between theory and experiment. The parameters A, B, C, ζ, α, and B_{kq} provide important information on the atomic and electronic structure of the paramagnetic centres. Ideally speaking, the numerical values of the input parameters can either be obtained from similar earlier parameter fittings or from *ab initio* calculations. However, the linewidth of the spectral lines for the $3d$ ions is usually quite broad, rendering an insufficient number of well-identified energy levels to fit all the necessary parameters. On the other hand, the *ab initio* calculations [18, 22]) still cannot yield values of the CF parameters, especially for low symmetry cases, where too many non-zero CF parameters exist.

In practice, the idea of transferability of the parameters [24] is adopted to estimate the parameters of a given $3d$ ion doped in new host crystals, based on their values in a structurally similar and well-studied host crystal. This strategy is applied in a slightly different way for the free-ion parameters, i.e, A, B, C, ζ, and α. Since these parameters are less sensitive to the crystalline environment than the CF parameters, they can be taken directly from the relevant literature (see, e.g., Refs. 25 and 26). The CF parameters B_{kq}, on the other hand, depend strongly on the type of the ligand as well as on the site symmetry.

3.3.2. Spin Hamiltonian and zero-field splitting

For an ion with an orbital singlet ground state, it is assumed that the lowest set of energy levels is isolated from the higher lying levels. Then, the ground state can be characterized by an *"effective spin"* ($\tilde{S}$), the value of which follows from the multiplicity

of the system $2\tilde{S}+1$. The properties of such an isolated system can then be fully described by the effective spin Hamiltonian as introduced by Pryce [27] and Abragam & Pryce [28]. The effective Hamiltonian includes all relevant contributions to the energy dependence on the effective electron spin $\tilde{S}$ and the nuclear spin I. Depending on the complexity of the system, a different number of spin-Hamiltonian terms are required for a satisfactory description of experimental results. The overall structure of the spin Hamiltonian of interest here, i.e, for the S state ($L=0$) $3d$ ions (e.g., Mn^{2+}, Fe^{3+}) or the ions with an orbital singlet ground state (e.g., Cr^{3+}, Fe^{2+}, Fe^{4+}) can be represented in the consistent Extentent Stevens' notation (see, e.g. the review article [29]) as

$$\tilde{H} = \tilde{H}_{Ze} + \tilde{H}_{ZFS} = \mu_B B \bullet g \bullet \tilde{S} + \sum_{0<n\leq2S}\sum_{-n<m<n}B_n^m O_n^m \qquad \text{Eq.3.9}$$

where the first term $\tilde{H}_{ze}$ represents the Zeeman energy, g being the spectroscopic splitting factor. The second term accounts for the splitting of the ground state in a crystal field of symmetry lower than cubic one for most cases. This splitting is caused by the spin-orbit as well as spin-spin interaction and contributes to the so-called **fine structure** or the zero-field splitting (**ZFS**) since it appears in the absence of a magnetic field.

The point symmetry of the surroundings of an ion determines which parameters in Eq.3.9 must be zero. For the case considered in this thesis, the most important symmetry effects are: (i) all terms with odd n disappear due to time-reversal symmetry [30] and, (ii) when the highest rotational symmetry axis is p-fold then the only nonzero terms have $m=lp$ where l is integral or zero. However, in very low symmetry cases, negative m values are also required, which reflects the low symmetry effects [31]. For example, for Mn^{2+} ions at the C_3 symmetry sites in $LiNbO_3$, we have

$$\tilde{H}_{ZFS} = B_2^0 O_2^0 + (B_4^0 O_4^0 + B_4^3 O_4^3 + B_4^{-3} O_4^{-3}) \qquad \text{Eq.3.10}$$

and

$$b_2^q = 3B_2^q; \qquad b_4^q = 60B_4^q$$

The extra ZFS $B_4^{-3} O_4^{-3}$ term in Eq.3.10 is introduced by C_3 symmetry and vanishes for C_{3v} symmetry. Buckmaster and Shing [32] have given a complete discussion of the terms required for different point groups for S up to 7/2. Their result is applicable to all S

$\leq 7/2$ if it is remembered that the terms n in Eq.3.9 is strictly smaller than or equal to $2S$ for lower spins. Their formalism is given in terms of the tensor operator T_{nm} [33] which is related to the Extended Stevens' operators through $O_n^m(O_k^q) = constant \bullet [T_{nm} + (-1)^m T_{n-m}]$. The conversion relations between various tensor operators have been reviewed by Rudowicz [29]. The explicit form of the "imaginary" terms corresponding to $O_n^m(O_k^q)$ with m negative, has been given, e.g., by Newman & Urban [34].

There exist various choices of the (x,y,z) axes with respect to the symmetry axes, especially for the low symmetry cases, which results in different sets of the parameters B_n^m in Eq.3.9 and the corresponding conventional parameters [35, 36] especially for the low symmetry cases. Any transformation, which only "relabels" the axes $\pm x$, $\pm y$, $\pm z$ leaves the form of $\tilde{H}_{ZFS}$ in Eq.3.9 invariant. Thus the ratio $\lambda' = B_2^2 / B_2^0 = b_2^2 / b_2^0$ and $\lambda = E/D$ can always be limited to the range $0 \leq \lambda' \leq 1$ and $0 \leq \lambda \leq 1/3$, respectively, by a proper choice of the axis system. This is the underlying idea for the standardization of conventions for orthorhombic $\tilde{H}_{ZFS}$ [36, 37], which has been extended to the monoclinic symmetry cases for CF Hamiltonian [38].

In the higher symmetry cases, there are various other notations used by various authors for the parameters equivalent to $B_n^m(b_n^m)$ parameters, which leads to some confusion in the literature. The two systems of ZFS parameters, i.e., (b_2^m, b_4^m) and (D,F,a) have most often been used for 3d ions at axial symmetry [30, 39]. For completeness the conversion relations between these parameters in different notations are listed here [29, 40]. Coefficients of the second-order spin terms are defined by;

$$D = b_2^0 = 3B_2^0 \qquad E = b_2^2 = B_2^2/3 \qquad \text{Eq.3.11}$$

It is important to note that a and F are defined differently according to whether a tetragonal or trigonal axis is taken as the z axis. The relations between the parameters for the two symmetries are [29, 40, 41]

Trigonal

$$a = -9B_4^3 / \sqrt{2} = -3b_4^3 / \sqrt{20\sqrt{2}}$$
$$F = 9(20B_4^0 - B_4^3 / \sqrt{2}) = -3(b_4^0 - b_4^3 / \sqrt{20\sqrt{2}}) \qquad \text{Eq.3.12}$$
$$i.e., \ b_4^0 = (F - a)/3$$

Tetragonal

$$a = -24B_4^4 = 2b_4^4 / 5$$
$$F = 36(5B_4^0 - B_4^4) = 3(5b_4^0 - b_4^4)/5 \qquad \text{Eq.3.13}$$
$$i.e., \ b_4^0 = (a + 2F/3)/2$$

where in both cases $F = 0$ for cubic symmetry. Note the exception in definition $b_4^3 = 3B_4^3$ used by Buckmaster & Shing [32].

The b_n^m parameters are numerically more convenient to determine the zero-field energy levels by considering the interaction matrix in Eq.3.9 in terms of the effective spin states. The exact expressions for the ZFS energy levels summarized by Bramley & Strach [40] for high-spin $3d^5$ ions e.g., Mn^{2+}, Fe^{3+}, affect the cubic symmetry with both trigonal distortion and tetragonal distortion, respectively.

3.4 Crystal-field analysis for Cr^{4+} ions

For Cr^{4+} ions occupying D_{2d} sites in YAG, the CF interaction is parameterized by:

$$H_{CF} = B_{20}C_0^{(2)} + B_{40}C_0^{(4)} + B_{44}(C_4^{(4)} + C_{-4}^{(4)}) \qquad \text{Eq.3.14}$$

where B_{kq} are CF parameters and $C_q^{(k)}$ are the renormalized spatial tensor operators.

The matrix elements of the Hamiltonian, Eq.3.1, were evaluated using the basis of states in the LS coupling scheme, which is suitable for the ligand field of the weak and/or intermediate range, i.e., strength for most of the 3d transition metal ions in crystals. We used the CF computer package [42] for the simulation and analysis of the experimental data on the energy levels and state vectors for $3d^N$ ions ($N = 1$ to 9) at arbitrary symmetry sites. The input parameters are the Racah parameters B and C, the Trees-correction α, the spin-orbit coupling ζ as well as the CF parameters B_{kq}. The free-ion parameters (i.e., B, C,

α, ζ) are expected to be less sensitive to the crystal environment than the CF paramters B_{kq}, which depend strongly on the type of the ligand as well as on the site symmetry. These latter parameters provide important information on the atomic and electronic structure of laser active centres. In the analysis of the experimental results, the crystal field parameters are taken as adjustable input parameters, and varied to obtain the best agreement between theory and experiment. The CF package [42] has been carefully tested and successfully applied to the analysis of Fe centres in photorefractive $BaTiO_3$ crystal [43]. It is suitable for the analysis of the energy levels as well as the fine structure of Cr^{4+} at D_{2d} symmetry sites in YAG.

The calculation of the energy levels and state vectors is done by the diagonalization of the Hamiltonian of Eq.3.1 within the $3d^2$ configuration. A full set of the input parameters for the CF analysis has not yet been determined for Cr^{4+} in YAG. Data for Cr^{4+} in other crystals are also scarce, which makes the analysis difficult. Eilers et al. [6] have estimated from the Tanabe-Sugano diagram some parameters for Cr^{4+} in YAG, namely, $B = 515$, $C = 2163$ and the cubic CF parameter $Dq = 915$ (in cm^{-1}) in the tetrahedral (T_d) approximation. Correspondingly, we obtain the cubic CF parameters [42b] $B_{40} = -21D_q = -19215$, $B_{44} = \sqrt{5/14}\, B_{40} = -11483$ (in cm^{-1}). Even through the tetragonal distortion changes B_{40} and B_{44} from their cubic values, yet they can be still used as the input parameters [42b]. We have calculated the energy levels of the Cr^{4+} ions and compared the results with the experimental levels by varying one parameter at a time. This trial and error fitting of the energy levels to the experimental data must be done with care because of the large number of parameters involved, and moreover, the adjustment of input parameters must be kept within reasonable limits. The best fit parameters are $B = 530$, $C = 2147$, $\alpha = 70$, $B_{20} = 7270$, $B_{40} = -21450$, $B_{44} = -9803$ (in cm^{-1}).

In obtaining the cubic (T_d) approximate values, we used the rotation invariants s_k, defined as [44]:

$$s_k = [\ \sum_{q=-k}^{k} |\ B_{kq}\ |^2\ ]^{1/2} \qquad\qquad Eq.3.15$$

For the cubic approximation the crystal field parameters in Eq.3.14 are $B_{20} = 0$ and $B_{44} = \sqrt{5/14}\, B_{40}$. We then obtain $s_4 = \sqrt{12/7}\, B_{40}$. For tetrahedral coordination, $B_{40} < 0$ whereas

for the octahedral one, $B_{40} > 0$. For both cases, $B_{40} = 21D_q$ is expected. The cubic approximate values for CF parameters are $B_{40} = -\sqrt{7/12}\,s_4 = -19507$ and $B_{44} = -\sqrt{5/24}\,s_4 = -11657$ in cm^{-1}. Our CF parameters are comparable to the experimental ones for Cr^{4+} ions in BGO [45]: $B = 428.8$, $B_{40} = -17220$ and $B_{44} = -10291$ (in cm^{-1}); and those for Cr^{4+} in Mg_2SiO_4 (forsterite) [46]: $B = 860$, $C = 4220$, $B_{40} = -21210$ and $B_{44} = -12675$ (in cm^{-1}).

3.5 Results and discussions

The crystal-field calculations are carried out within the free-ion basis functions $|^{2S+1}L, M_S, M_L>$. The Cr^{4+} free-ion terms are ^3F, ^3P, ^1S, ^1D and ^1G with a total of 45 states. When the symmetry is lowered to T_d, the ^3F ground term splits into three crystal-field states $^3A_2$ (ground), $^3T_2$ and $^3T_1$, while the higher terms split as follows ^3P: $^3T_1$; ^1S: $^1A_1$; ^1D: $^1T_1$, ^1E; ^1G: $^1T_2$, ^1E, $^1T_1$, $^1A_1$. Lowering the crystal-field symmetry from T_d to D_{2d}, i.e. elongating the ideal tetrahedron along one of the [001] axes of YAG, yields a further splitting and a mixing of the sublevels. Taking the spin triplets as an example, the ground $^3A_2$ state becomes $^3B_1$, the $^3T_2(^3F)$ splits into $^3B_2$ and ^3E with $^3B_2$ the lowest, the $^3T_1(^3F)$ splits into $^3A_2$ and ^3E, whereas the $^3T_1$ (^3P) splits into $^3A_1$ and ^3E. The calculated energy levels for Cr^{4+} ions in D_{2d} symmetry and in the T_d approximation are given in Table.3.1 together with the available observed values. The mixtures of various free-ion states for each level in D_{2d} symmetry are also indicated.

The radiative transitions between pure $3d^N$ states normally occur only through a magnetic-dipole process due to parity violation. However, any deviation from inversion symmetry in the site occupied by the ion can cause a slight mixture of other p or f odd parity configurations into the $3d$ configuration, which will allow the electric dipole transition to occur. The tetrahedrally coordinated Cr^{4+} exhibits large transition probabilities due to the lack of inversion symmetry in T_d symmetry. From group theory considerations, the electronic-dipole operator transforms according to T_2 in T_d, so that the $^3A_2 \rightarrow ^3T_1$ transition is allowed, but $^3A_2 \rightarrow ^3T_2$ is forbidden [46]. The effect of the perturbation from the lower D_{2d} symmetry would also increase the transition probability somewhat, but, in any case, by less than an order of magnitude. The transition from the

ground to the $^3T_2(^3F)$ levels is expected to be weak, whereas that to the $^3T_1(^3F)$ energy levels is expected to be strong. For Cr^{4+}-doped materials such as forsterite (Mg_2SiO_4), the visible absorption around 600 nm is about an order of magnitude stronger than the NIR absorption. The strong visible absorption was assigned to a transition to the $^3T_1$ state and the NIR absorption was assigned to a transition into the $^3T_2$ state. However, in Cr^{4+}:YAG the visible absorption at about 640 nm and NIR absorption strength are of the same order of magnitude. Hence it is justified to ascribe these two broad bands to the D_{2d} symmetry components $^3A_2$ and ^3E of the $^3T_1$ state in T_d symmetry [6] as confirmed by our calculation.

In T_d symmetry, there are states that belong to the same irreducible representation and have the same spin quantum number, e.g., $^3T_1(^3F)$ and $^3T_1(^3P)$. The electrostatic interaction (Eq.3.2) admixes such states since it has nonvanishing matrix elements between them. The CF of D_{2d} symmetry further splits these levels, whereas the large value of B_{20} causes the $^3T_1(^3F)$ levels to intersperse with the $^3T_1(^3P)$ ones. In terms of the cubic approximation, such mixture of the cubic terms would make the analysis of the experimental data next to impossible. For T_d symmetry the transition from the ground state $^3A_2$ to pure $^3T_1(^3P)$ state is expected to be weak since it requires both electrons to change their crystal field state (from e to t_2) as shown in the Tanabe-Sugano diagram [47]. In D_{2d} symmetry, due to the strong mixing between $^3T_1(^3F)$ and $^3T_1(^3P)$ states, their crystal-field components, i.e., $^3A_2$ and ^3E states, are expected to have an absorption strength of the same order of magnitude. Our calculation supports the absorption band around 450 nm at low temperatures as due to the transition from the ground state $^3B_1$ to $^3E(^3T_1)$ of the ^3F terms. However, since this absorption band does not contribute to the excitation, there remain the possibilities that it is due to transitions of Cr^{3+} at octahedral sites [7] or to charge transfer transitions involving Cr^{3+} and Cr^{4+} ions.

Large orbital splittings of Cr^{4+} in YAG are also revealed in Table 3.1. The orbital splittings for $^3T_1(F)$ and $^3T_2(F)$ are about 5340 cm^{-1} and 1850 cm^{-1}, respectively while for the lowest excited state ^1E and the highest triplet $^3T_1(P)$, the splittings are 30 cm^{-1} and 2570 cm^{-1}, respectively. These quite large noncubic splittings imply a strong distortion of

Table 3.1 Crystal-field energy levels (without spin-orbit interaction) for Cr^{4+} ion in YAG at T_d and D_{2d} symmetry sites [in cm^{-1}(nm)]. The values of the parameters are: $B = 530$, $C = 2147$, $\alpha = 70$, $B_{40} = -19507$ and $B_{44} = -11657$ for T_d and $B = 530$, $C = 2147$, $\alpha = 70$, $B_{20} = 7270$, $B_{40} = -21450$, $B_{44} = -9803$ (in cm^{-1}) for D_{2d}.

T_d approximation	D_{2d} symmetry	Obs. (Ref.6)	Free-ion state mixing of D_{2d}
$^3A_2$ 0	$^3B_1$ 0	0	$1.00\ ^3F$
^1E 8258	A_1 8265(1210)	8264 (1210)	$0.609\ ^1D + 0.366\ ^1G + 0.025\ ^1S$
	$^1B_1$ 8294(1206)	8291 (1206)	$0.672\ ^1D + 0.328\ ^1G$
$^3T_2$ 9289	$^3B_2$ 7811 (1280)	7812 (1280)	$1.00\ ^3F$
	^3E 9664 (1035)		$0.980\ ^3F + 0.020\ ^1P$
$^3T_1(F)$ 13749	$^3A_2$ 9999 (1000)	10000 (1000)	$0.598\ ^3P + 0.402\ ^3F$
	^3E 15336 (652)	15385 (650)	$0.853\ ^3F + 0.147\ ^3P$
$^1A_1$ 14897	$^1A_1$ 15522 (644)		$0.768\ ^1G + 0.134\ ^1D + 0.098\ ^1S$
$^1T_2$ 17309	$^1B_2$ 15974 (626)		$0.722\ ^1D + 0.288\ ^1G$
	^1E 17507 (571)		$0.764\ ^1D + 0.236\ ^1D$
$^1T_1$ 20503	$^1A_2$ 16072 (622)		$1.00\ ^1G$
	^1E 22874 (437)		$0.938\ ^1G + 0.061\ ^1D$
$^3T_1(P)$ 21367	^3E 20839 (480)	20833 (480)	$0.833\ ^3P + 0.167\ ^3F$
	$^3A_2$ 23414 (427)		$0.402\ ^3P + 0.598\ ^3F$
^1E 28057	$^1A_1$ 24501 (408)		$0.696\ ^1G + 0.233\ ^1D + 0.071\ ^1S$
	$^1B_1$ 30750 (325)		$0.672\ ^1G + 0.328\ ^1D$
$^1T_1$ 28296	^1E 26861 (372)		$0.826\ ^1G + 0.174\ ^1D$
	$^1A_2$ 30878 (324)		$0.722\ ^1G + 0.278\ ^1D$
^1A 40744	$^1A_1$ 41515 (241)		$0.806\ ^1S + 0.170\ ^1G + 0.024\ ^1D$

the tetrahedron. The tetrahedral angle for an ideal tetrahedron is 54.7°, while it is 50.3° [48] for Cr^{4+} ions in the YAG lattice due to the elongation of the oxygen ligands along the crystallographic axes. Brik and Zhorin [49], based on the exchange model, suggested that the large splitting of $^3T_1(F)$ (5000 - 7000 cm^{-1}) in the D_{2d} crystal field is also enhanced by ^3P-^3F mixing.

For Cr^{4+} in the intermediate CF, the states ^1E and $^3T_2$ are quite close to each other, and hence the emission spectrum for $3d^2$ ions is more complicated as pointed out by Yen and Jia [1]. The transitions between the $^3T_2$ and $^3A_2$ states are electric-dipole forbidden, which makes the $^3T_2$ excited state metastable. The ^1E excited state is separated from the ground state by almost the same energy gap as the $^3T_2$ state, which is also metastable by virtue of the spin-forbiddenness of the electric-dipole transitions. Laser emission from Cr^{4+} in YAG is due to the $^3T_2 \to {}^3A_2$ transition, or precisely the $^3B_2 \to {}^3B_1$ transition in D_{2d} symmetry, while in isoelectronic Mn^{5+} in $Ba_3(VO_3)_2$ the laser emission is due to the $^1E \to {}^3A_2$ transition in T_d symmetry [8]. Mn^{5+}-doped $Ba_3(VO_3)_2$ is a high-field system, i.e., the first excited-state is a spin singlet while the ground-state is a spin triplet. The NIR emission is characterized by sharp emission peaks, due to the spin-forbiddingness of the transitions, typically with a lifetime of few hundreds of μs. The emission from Cr^{4+} in YAG is spectrally broader and has a lifetime in the range of several μs. Although the ^1E state is the lowest excited state in the T_d approximation, the strong distortion of the tetrahedron induces a large orbital splitting of the crystal-field components of $^3T_2$, resulting in the $^3B_2$ state becoming the lowest excited state. The two crystal-field components of the ^1E level are now between the $^3B_2$ and ^3E components of the $^3T_2$ level. The transition between the two spin triplets $^3B_1 \to {}^3B_2$ would therefore be spin-allowed and should show a shorter lifetime than for the Mn^{5+} case.

The presence of ESA for many Cr^{4+} tunable solid-state lasers is a limiting factor for efficient laser performance [11-13, 50]. Laser light can be either amplified by stimulated emission, where the ion drops to a lower energy level (usually the ground state), or it can be attenuated through ESA, in which case the ion makes the transition from an upper level to a higher-lying level. If the cross-section for ESA is greater than that for stimulated emission, no laser action will occur regardless of the power level of the pump. The energy

levels in Table 3.1 suggest that when the Cr^{4+}:YAG laser crystal is pumped by the 1064 nm radiation of Nd:YAG, the pump light may be absorbed to excite the Cr^{4+} ion from the ground-state to the $^3A_2$ level, which may nonradiatively drop to the $^3B_2$ level. The transition from $^3B_2$ to the ground state $^3B_1$ is responsible for the stimulated emission. ESA could occur also for transitions from $^3B_2(^3T_2)$ to $^3E(^3T_1)$, or possibly from $^3E\,(^3T_2)$ to $^1E(^1T_2)$ and/or $^1A_2(^1T_1)$. The pump ESA would occur due to transitions from $^3A_2(^3T_1(F))$ to $^3E(^3T_1(P))$. Unfortunately, theoretical calculation cannot provide an estimation of the ESA cross-section. Its experimental value can be obtained from laser performance, as described in Chapter 4, and it appears that the small gain of the Cr^{4+}:YAG laser (typical 2% per cavity pass) [13, 14] is due to the presence of various ESA mechanisms. In a Cr^{4+}:YAG laser, the transitions from the higher-lying levels (excited first either due to the ground state absorption or ESA) to $^3B_2(^3T_2)$ could be fast, so that their associated lifetimes are small (typical a few ps). The $^3B_2(^3T_2)$ fluorescence lifetime is known to be 3.6 µs at room temperature [7]. So under these conditions, only the ground-state $^3B_1(^3A_2)$ and the first excited state $^3B_2(^3T_2)$ are notably populated, causing the Cr^{4+} ions to lase.

Taking into account the spin-orbit coupling H_{so}, we can consider the zero-field splitting of the ground-state $^3B_1$ of Cr^{4+}, i.e., the splitting of the three spin levels with an *effective* spin $S = 1$. The zero-field splitting (**ZFS**) can be described by the following spin Hamiltonian:

$$\tilde{H}_{ZFS} = D(S_z^2 - \frac{1}{3}S(S+1)) + E(S_x^2 - S_y^2) \qquad Eq.3.16$$

where D and E are respectively the axial and rhombic ZFS parameters. The spin states of the orbital singlet $^3B_1$ ground state are split by $\tilde{H}_{ZFS}$, Eq.3.16, as follows: the $m_S = \pm 1$ levels are split by $2E$ and centred at energy D above the $m_S = 0$ level. The complete diagonalization of H, Eq.3.1, with H_{so}, yields $D = -1.55$ cm^{-1} and $E = 0$ for Cr^{4+} ions at D_{2d} symmetry sites in YAG. Our results agree well with the angular overlap model calculation by Kück et al. [48], where the ZFS of the ground state $^3A_2$ (T_d symmetry), actually $^3B_1$ (in D_{2d}), was predicted to be of the order of 2 cm^{-1}, with the doublet $m_S = \pm 1$ as the lowest state. The ZFS of the $^3B_1$ ground state cannot be resolved by optical spectroscopy due to various sorts of broadening mechanisms. Electron paramagnetic

resonance (EPR) would be a powerful tool for probing the ground-state structure. Since Cr^{4+} is a non-Kramers ion with a large ZFS parameter D, high-field and/or high-frequency EPR should be used to gain a full understanding of the Cr^{4+} ground-state structure in YAG. From 34 GHz EPR studies, Budil et al. [51] obtained $D = +2.14$ cm^{-1} and $E = -0.15$ cm^{-1} for Cr^{4+} ions at sites of orthorhombic symmetry in forsterite (Mg_2SiO_4), corresponding to the $m_S = \pm 1$ level higher than the ground $m_S = 0$ level. The ZFS of the $^3B_1(^3A_2)$ ground state in YAG is expected to be about 2 cm^{-1}, similar to that observed for the Cr^{4+} ions in forsterite but with D negative.

3.6 Summary

In this chapter, detailed investigations of the excited-state absorption in the Cr^{4+}:YAG gain medium have been described. ESA at the lasing wavelength occurs for the transition from the state $^3B_2(^3T_2)$ to $^3E(^3T_1(F))$, while the pump ESA comes from the transition from $^3A_2(^3T_2)$ to $^3E(^3T_1(P))$. It is found that the ESA introduces a significant loss to the Cr^{4+}:YAG laser. Using the laser efficiency data, the ESA cross-sections for the free-running mode are estimated and compared with the reported data. In Chapter 4, a broad cw tuning range of 1335 to 1557 nm is demonstrated using one set of mirrors and a birefringent filter. This broad tuning range makes the Cr^{4+}:YAG laser useful for the optical communication applications.

3.7 References

1. Yen W.M. and Jia W., "*in the spectroscopy of Cr^{4+}-doped laser materials*", J. Appl. Spectros. **62**, 966-212 (1995).

2. Pollock C.R., Barber D.B., Mass J.L. and Markgraf S., "Cr^{4+} *lasers: present performance and prospects for new host lattices*", IEEE J. Selected Topics in QE **1**, 62-6 (1995).

3. French P.M.W., "*Ultrafast solid-state lasers*", Contemporary Phys. **37**, 283-301 (1996).

4. Shestakov A.V., Borodin N.I., Zhitnyuk V.A., Ohrimtchynk A.G. and Gapontsev V.P., "*Tunable Cr^{4+}: YAG lasers*", in *Technical Digest of Conference on Lasers and Electro-Optics* (Optical Society of America, Washington, DC, 1991), paper CPDP11.

5. French P.M.W., Rizvi N.H. and J. R. Tayer, "*Continuous wave mode-locked Cr^{4+} :YAG laser*", Opt. Lett. **18**, 39-41 (1993).

6. Eilers H., Hommerich V., Jacobsen S.M. and Yen W.M., "*Spectroscopy and dynamics of $Cr^{4+}:Y_3Al_5O_{12}$*", Phys. Rev. B **49**, 15505-13 (1994).

7. Kück S., Petermann K., Pohlmann U. and Huber G., "*Electronic and vibronic transition of the Cr^{4+}-doped garnet $Lu_3Al_5O_{12}$, $Y_3Al_5O_{12}$, $Y_3Ga_5O_{12}$ and $Gd_3Ga_5O_{12}$*", J. Lumin. **68**, 1-14 (1996).

8. Merkle L.D., Pinto A., Vertun H.R. and McIntosh B., "*Laser action from Mn^{5+} in $Ba_3(VO_4)_2$*", Appl. Phys. Lett. **61**, 2386-9 (1992).

9. Ferracin L.C., Davolos M.R. and Nunes L.A.O., "*MnO_4^{3-} NIR luminescence in Ba_2SiO_4*", J. Lumin. **72-74**, 185-7 (1997).

10. Sandrez F. and Kellon A., "*Laser dynamics with excited-state absorption*", J. Opt. Soc. Am. B **14**, 1209-13 (1997).

11. Brunold T.C., Gudel H.U., Hazenkamp M.F., Huber G. and Kuck S., "*Excited state absorption measurements and laser potential of Cr^{4+}-doped Ca_2GeO_4*", Appl. Phys. B **64**, 647-50 (1997)

12. Kück S., Schepler K.L., Hartung S., Petermann K. and Huber G., "*Excited state absorption and its influence on the laser behavior of Cr^{4+}-doped garnets*", J. Lumin. **72-74**, 222-3 (1997).

13. Sennaroglu A., Pollock C.R. and Nathel H., "*Efficient continuous wave chromium-doped YAG laser*", J. Opt. Soc. Am. B **12**, 930-7 (1995).

14. Spalter S, Bohm M., Burk M., Mikulla M., Fluck R., Jung L.D., Zhang G., Keller U., Sizmann A. and Lenchs G., "*Self-starting soliton-modelocked femtosecond Cr^{4+}:YAG laser using an antiresonant Fabry-Perot sarurable absorber*", Appl. Phys. B **65**, 335-8 (1997).

15. Ballhausen C.J., *Introduction to ligand field theory*, (McGraw-Hill, New York, 1962).

16. Schlafer H.L. and Gilmann G., *Basic priciples of ligand field theory*, (Wiley-Interscience, New York, 1969).

17. Gerloch M. and Slade R.C., *Ligand field parameters* (Cambridge, London, 1973).

18. Hufner S., Optical Spectra of transition rare early components, (Academic Press, New York, 1978).

19. Wybrourne B.G., *Spectroscopic properties of rare-earth*, (Wiley, New York, 1965).

20. Morrison C.A., Augular momentum theory applied to interations in solids (Springer-Verlag, Berlin, 1992).

21. Zhao M.G. and Yu W.L., *Crystal field theory*, (Sichuan Education, Chengdu, 1988).

22. Condon E.U. and Odabasi H., *Atomic structures*, (Cambridge University press, London, 1980).

23. Nielson C.A. and Koster G.F., *Spectroscopic coefficients for p^n, d^n and f^n configurations*, (MIT press, Massachusetts, 1964).

24. Yeung Y.Y. and Rudowicz C., Computers Chem. **16**, 207 (1992).

25. Morrison C.A., *Crystal fields for transition-metal ions in laser host materials*, (Springer-Verlag, Berlin, 1992).

26. Newman D.J., Adv. Phys. **20**, 197 (1971).

27. Pryce M.H.L., Proc. Phys. Soc. A **63**, 25 (1950).

28. Abragam A. and Pryce M.H.L., Proc. Roy. Soc. (London) A **205**, 135 (1951).

29. Rudowicz C., Magn. Res. Rev. **13**, 1 (1987).

30. Abragam A. and Bleaney B., *Electron Paramagnetic resonance of transition ions.* (Dover New York, 1986).

31. Roitsin A.B., Phys. Status Solidi (b) **104**, 11 (1981).

32. Buckmaster H.A. and Shing Y.H., Phys. Status Solidi (a) **12**, 325 (1972).

33. Buckmaster H.A., Chatterjee R. and Shing Y.H., phys. status solidi (a) **13**, 9 (1972).

34. Newman D.J., and Urban W., Adv. Phys. **24**, 793 (1975).

35. Rudowicz C., J. Phys. C. solid state phys. **20**, 6033 (1987).

36. Rudowicz C. and Bramley R., J. Chem. Phys. **83**, 5192 (1985).

37. Pole C.P. Jr., Farach M.A. and Jackson W.K., J. Chem Phys. **61**, 2220 (1974).

38. Rudowicz C., J. Chem. Phys. **83**, 5192 (1986).

39. Pilbow J.R., *Transition ions electron paramagnetic resonance*, (Oxford University press, Oxford, 1990).

40. Bramley R. and Strach S.J., Chem. Rev. **83**, 49 (1983).

41. Hutchings M.T., Solid State Phys. **16**, 227 (1964).

42. (a). Chang Y.M., Rudowicz C. and Yeung Y.Y., *"Crystal-field analysis of the $3d^N$ ions at low symmetry sites involving imaginary terms"*, Computers in Phys. **48**, 583-8 (1994).

    (b) Yeung Y.Y. and Rudowicz C., *"Ligand field analysis of the $3d^N$ ions at orthorhombic or higher symmetry sites"*, Comput. Chem. **16**, 207-16 (1992).

43. Chang Y.M, Wang H.F. and Rudowicz C., *"Crystal-field energy levels of deep Fe centers at orthorhombic and higher symmetry sites in $BaTiO_3$"*, J. Opt. Soc. Am. B **9**, 544-52 (1995).

44. Morrison C.A., *"Possible hosts for quadruply ionized $3d^N$ transition metal ions: Na_2TiSiO_5, $Y_2SiBe_2O_7$, $Bi_4X_3O_{12}$ and $Bi_4X_3O_{12}$ (X= Si, Ge)"*, Report HDL-TM-91-1 (1991).

45. Wardzynski W., Szymczak H. and Pataj K., *"Light induced charge transfer processes in Cr-doped BGO and BSO"*, J. Phys. Chem. Solids **43**, 767-9 (1982).

46. Jia W., Liu H., Jeffe S. and Yen W.M., *"Spectroscopy of Cr^{3+} and Cr^{4+} ions in forsterite"*, Phys. Rev. B **43**, 5234-42 (1991).

47. Henderson B. and Imbusch G.F., *Optical Spectroscopy of Inorganic Solids* (Clarendon, Oxford, 1989), p.128.

48. Kück S., Pohlmann U., Petermann K., Huber G. and Schonberr T., "*High resolution spectroscopy of Cr^{4+} doped $Y_3Al_5O_{12}$*", J. Lumin. **60&61**, 192-6 (1994).

49. Brik M.G. and Zhorin V.V., "*Energy levels of Cr^{4+} in YAG*", J. Lumin. **72-74**, 149-151 (1997).

50. Eiler H., Hommerich U., Jacobsen S.M. and Yen W.M., "*Spectroscopic properties of $Cr^{4+}:Lu_3Al_5O_{12}$*", Opt. Lett. **18**, 1928-30 (1993).

51. Budil D.E., Park D.G., Burlitch J.M., Geray R.F., Dieckmann R. and Freed J.H., "*9.6 GHZ and 34 GHZ EPR studies of chromium-doped forsterite*", J. Chem. Phys. **101**, 3538-48 (1994).

Chapter 4

Continuous-wave laser performance of Cr^{4+}:YAG laser

4.1 Introduction

The fluorescence spectrum of an isolated ion is different from that associated with the ion when incorporated into a crystal host because of the influence of the crystal field on its energy levels. Among the transition-metal-ion candidates for tunable laser operation, chromium has been frequently used because of its chemical stability, broad pump bands and other favorable characteristics. Tunable chromium lasers utilizing Cr^{3+} as the lasing centres include alexandrite [1], emerald [2], Cr^{3+}:LiCAF, and Cr^{3+}:LiSAF [4]. These lasers have tuning ranges extending roughly between 700 and 900 nm. Lasing action with the Cr^{4+} ions has been demonstrated in a number of hosts including Cr^{4+}:forsterite [5], Cr^{4+}:YAG [6] and Cr^{4+}:Y_2SiO_5 [7], the latter having been only cryogenically operated to date.

The Cr^{4+}:YAG tunable solid-state laser, first reported by Angert et al. [6] in 1988 is unique as a source of coherent radiation since it can be tuned over the 1.55 µm wavelength range of optical telecommunications. The YAG crystal has a lattice constant larger than that of other hosts. The surrounding ions in the lattice are further away from the Cr^{4+} centres and the crystal field experienced is weaker. Hence Cr^{4+}:YAG lases at wavelengths (1.34 ~ 1.58 µm) longer than those of the other Cr^{4+} media. The YAG crystal has excellent optical and thermal properties and can be grown to a very high optical quality. It is the most important laser crystal for almost 30 years.

To date, various modes of operation employing the Cr^{4+}:YAG gain medium have been demonstrated. As a saturable absorber with an absorption band in the 0.9 to 1.1 µm region, it has been used to passively Q-switch Nd:YAG lasers operating at 1.06 µm [8]. As an optical gain medium, Q-switched [6,9,10], cw [11,12], cw mode-locked [13], and self-mode-locked operation [14-20] have been demonstrated. Dual wavelength operation

at both 1.06 and 1.44 μm have also been demonstrated by simultaneously employing a Cr^{4+}:YAG crystal as a Q-switch and a laser gain medium [21].

In this chapter, a detailed design and characterization of a cw Cr^{4+}:YAG laser is presented. The experiments performed concentrate primarily on a systematic study of the cw performance of this gain medium as a function of pump power, output wavelengths, output coupling, saturable absorption and thermal loading. Such data clearly show the sensitivity of the output power to the variation of a number of related operating parameters and will offer useful guidelines about how to design an efficient Cr^{4+}:YAG laser system. For the sake of completeness, Section 4.2 gives some backgound on the properties of the Cr^{4+}:YAG crystal. This is followed by simulations of the cavity stability criterion using the Gaussian-beam $ABCD$ theory. The experimental setup and alignment procedure are described in Sections 4.4 and 4.5. In the sections that follow, the performance of the Cr^{4+}:YAG laser is presented including the details of slope efficiency, tuning range, saturable absorption and thermal effects. The estimation of the stimulated emission and excited-state absorption (ESA) cross-sections for the free-running mode is presented in Section 4.7. Finally, it should be noted that the broadest tuning range of the Cr^{4+}:YAG laser to this date achieved in our experiments was obtained with one set of cavity mirrors.

4.2 Pump light absorption in Cr^{4+}:YAG

Extensive spectroscopic studies [21, 22] show that the active Cr^{4+} sites give rise to the 1.4 μm fluorescence. Because the preferred charge state of the substitutional chromium ions for laser action differs from that of the trivalent aluminum ions, YAG crystals are simultaneously codoped with divalent earth ions (magnesium or calcium) for charge compensation. The chromium-doped YAG crystal codoped with magnesium or calcium can be routinely grown by using the Czochralski technique and the preferred tetravalent charge state of the chromium ions can be enhanced by subsequently annealing the crystals in an oxidizing environment.

Chapter 3 theoretically investigated the spectroscopic and lasing properties of a Cr^{4+}:YAG gain medium assuming that the active Cr^{4+} ions are tetrahedrally coordinated with D_{2d} site symmetry [23, 24]. It should be noted that the presence of ESA, overlapping with the emission spectrum of the centre and originating from the $^3T_2$ state, is a major drawback for efficient laser operation, not only increasing the laser threshold but also putting a fundamental limit to the highest efficiency attainable from the laser. Later in Section 4.7, the effects of ESA on the cw laser performance will be delineated.

Table 4.1 shows the physical properties of the Cr^{4+}:YAG gain medium compared to those of the Ti:sapphire crystal. The important laser parameters for Cr^{4+}:YAG are almost the same as those of a $Ti:Al_2O_3$ crystal except for the existence of excited-state absorption and a lower thermal conductivity. Therefore a similar laser performance should be expected.

The fluorescence of Cr^{4+}:YAG is polarized and the effect depends on the orientation of the pump polarization relative to the crystal axis [24, 25]. Polarized spectroscopy spectra show that the maximum emission intensity is obtained when the pump and emission electric fields are parallel to the [001] axis, or equivalently the [010] direction in the crystal. In the laser experiments, Brewster-angled Cr^{4+}:YAG rods were used and they were cut with the [001] crystal direction in the horizontal plane. This ensures that more energy is channeled into the horizontal polarization such that the lasing efficiency of the rods is maximized.

Table. 4.1 Physical properties of Ti:sapphire and Cr^{4+}:YAG

	Ti:sapphire	Cr^{4+}:YAG	Units
Chemical formula	Ti^{3+}:Al_2O_3	Cr^{4+}:$Y_3Al_5O_{12}$	-
Site symmetry	C_{3v}	D_{2d}	-
Tunable range (max.)	0.6 – 1.1	1.34 – 1.58	μm
Density of active ions	~ 3.3	~ 0.4	10^{-19} cm^{-3}
Absorption coefficient	6.5	1.2 ~ 1.8	cm^{-1}
Upper state lifetime @300K	3.2	3.6	μs
Saturable signal intensity	4	4.2	10^5 W/cm^2
Index of refraction	1.76	1.81	-
Nonlinear index of refraction	3	1.9	10^{-16} cm^2/W
Absorption cross section		1.3	$10^{-18}cm^2$
Emission cross section	3.8	0.75	10^{-19} cm^2
Peak gain cross-section	3.9	3	10^{-19} cm^2
Linear thermal dispersion (dn/dT)	1.2	9.86	10^{-6} K^{-1}
Thermal conductivity	0.34	0.13	W/(cm K)
ESA cross section	N/A	0.2	10^{-19} cm^2

4.3 Cavity simulation using Gaussian-beam *ABCD* theory

Attainment of the stability criterion of laser cavities requires a careful calculation of the beam parameters inside the cavity. This section gives a brief outline of the numerical method used to calculate the laser spot size inside the laser cavity. The technique is based on the assumption that the precise location of at least one collimated beam waist is predetermined. This is usually satisfied. By transferring this beam across a set of optical elements which are characterized by *ABCD* matrices, one can calculate the spot size and the position of the next collimated beam in a systematic way using simple algebraic equations. Appendix II presents the basic equations of the *ABCD* theory and lists the forms of the ABCD matrices for frequently occuring situations including the elements in our cavity. In the case of the laser cavities used in this thesis, there is always one flat high-reflector and one output coupler, which is the location of the waist by definition.
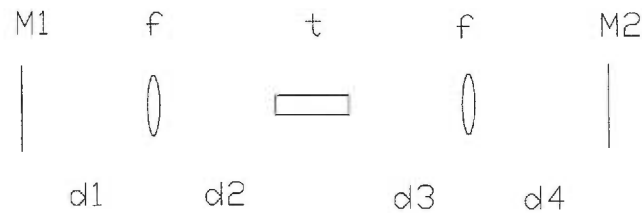
Fig. 4.1 Schematic of a linear laser cavity with the intracavity focusing lenses

Fig. 4.1 shows a typical cavity, consisting of two flat end mirrors M1 and M2, two equal focal-length intracavity lenses *f* and a gain medium *t* of high index of refraction. The Z-fold cavity configuration used in the later experiments can be readily reduced to this linear configuration. Because of the presence of the flat-end high-reflector (HR) M1, a collimated beam is guaranteed at this location, hence satisfying the assumption of the procedure. The equation for the Rayleigh range z_1 at M1 can be derived from the self-consistency requirement on the Gaussian beam that has completed one round trip. Having

calculated the transformation matrix M_c for the cavity, starting from M1 and making a complete round-trip, the Rayleigh range z_1 at M1 is given by:

$$z_1 = \frac{|B_c|}{\sqrt{1 - (\frac{A_c + D_c}{2})^2}}$$ Eq.4.1

for

$$\frac{A_c + D_c}{2} < 1$$ Eq.4.2

Eq.4.1 for z_1 shows that z_1 depends on the elements of the transformation matrix M_c. The Rayleigh range z_1 is related to the beam spot radius w_1 through

$$z_1 = \frac{n\pi w_1^2}{\lambda}$$ Eq.4.3

where n is the index of refraction and λ is the wavelength of the propagation beam. The Rayleigh range is the distance over which the beam remains relatively collimated expanding in radius by no more than a factor of 1.44. General properties of Gaussian beams and their propagation characteristics may be found in standard laser textbooks [26, 27].

Eq.4.2 is the resulting stability criterion on the invariant trace of the cavity round-trip transformation matrix M_c. The subscript 'c' indicates that the *ABCD* coefficients are calculated for a given cavity. Once z_1 at M1 is obtained, one can transform this beam and calculate the beam spot size and the position of the beam waist from the crystal edge using the transformation matrix that will image this collimated beam to the front face of the crystal.

Using this procedure, the characteristics of a symmetric cavity have been simulated. Fig. 4.2 shows respectively the variation of stability $(A+D)/2$, the spot size at M1, the position of beam waist from crystal edge and the beam spot size in the crystal as a function of d_2. The parameters are $d_1 = d_4 = 26$ cm, $d_3 = 4.65$ cm, $t = 2$ cm, $n = 1.81$ and $\lambda = 1.45$ μm. (Note that the spot size is defined as the beam spot diameter $2w$). It is shown that, with all the other dimensions kept fixed, only one stable region for the values of d_2 exists.
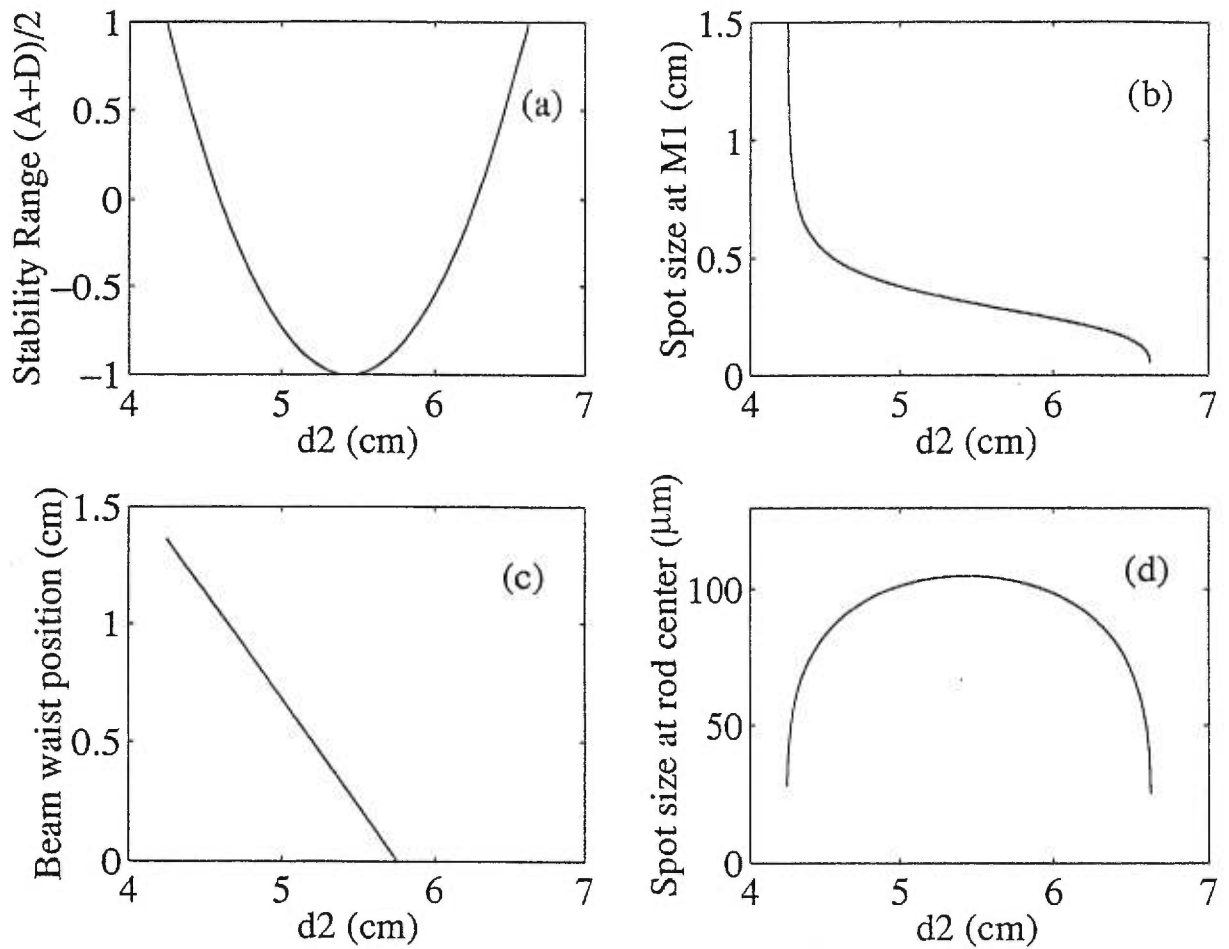
Fig. 4.2 Variation of (a) stability range $(A+D)/2$, (b) spot size at M1,

(c) beam waist position of the focussed beam from the crystal edge, and

(d) spot size at the crystal center, as a function of d_2.
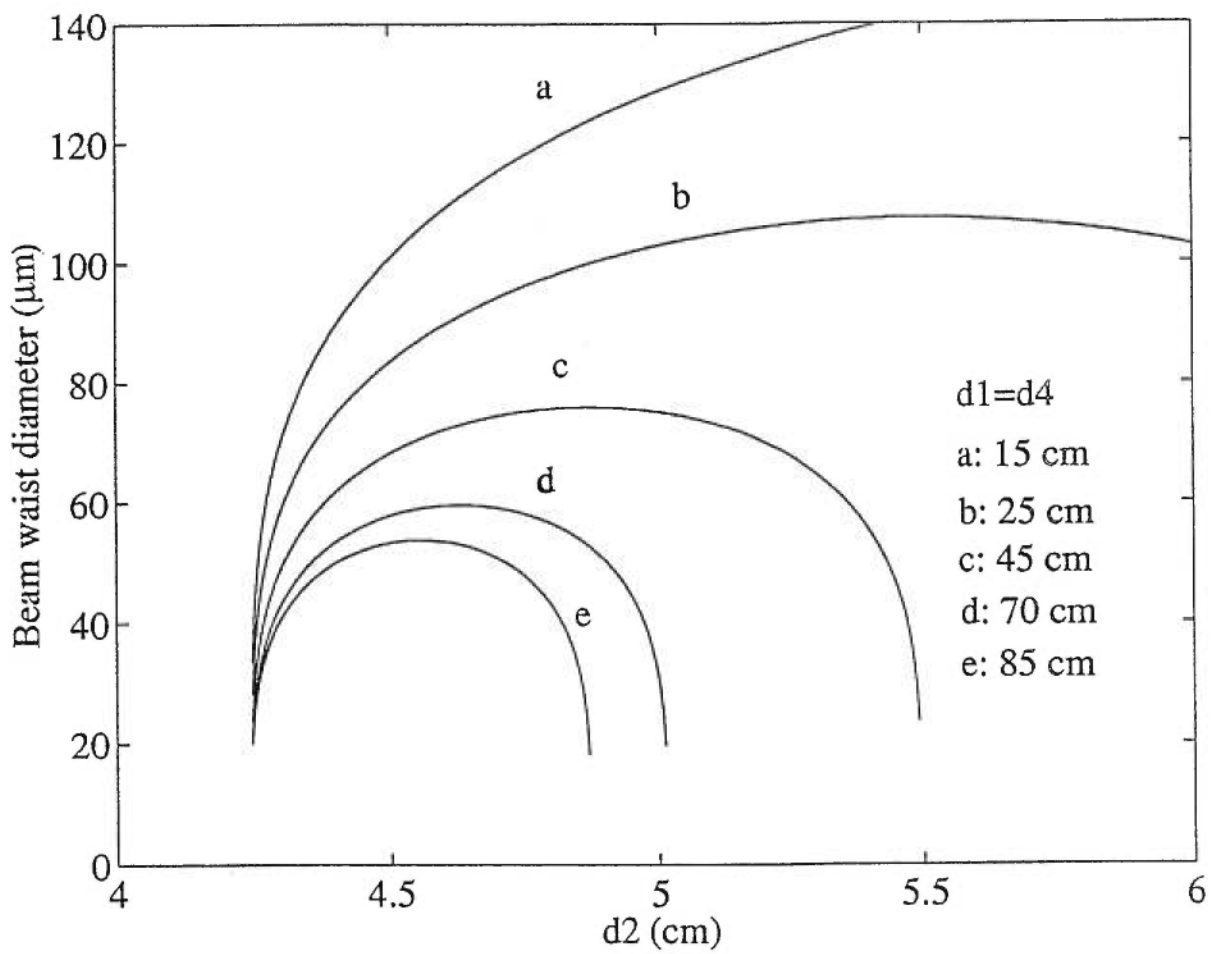
Fig. 4.3 Variation of the focused beam diameter inside the crystal for symmetric cavity of different lengths.

Fig. 4.3 shows the variation of the focused beam diameter in μm at the centre of the crystal for symmetric cavities of different cavity lengths as a function of d_2. In this case, as the total cavity length increases, the beam waist inside the cavity becomes tighter and the stability condition more stringent.

In practice, in the stable region of the laser cavity, the pump beam parameters have to be adjusted in such a way as to have the maximum overlap of the lasing and pump volumes in the gain medium. That is, careful mode matching of the pump and laser cavities is essential in order to obtain the best CW performance from the Cr^{4+}:YAG laser (Refer to Fig. 2.3 in Chapter 2).

4.4 Design of an astigmatically compensated cavity

A schematic of the experimental setup used to characterize the cw Cr^{4+}:YAG laser is shown in Fig. 4.4. The laser is pumped by a cw Nd:YAG laser (Spectra-physics, Model 3600) through an AR-coated, mode-matching lens of 10 cm focal length. The resonator is a symmetrical, astigmatically compensated, Z-fold cavity of approximately 65 cm in total length, similar to that of a standard Ti:sapphire laser. The Brewster-angled, cylindrical Cr^{4+}:YAG laser crystal with 5-mm-diameter and 2-cm-long was obtained from the IRE-POLUS. The Cr^{4+}:YAG laser rod was surrounded with indium foil and tightly clamped between two copper holders which exchanged heat with a lower copper heat sink and maintained at about 18°C by circulating chilled water.

The laser crystal was positioned between two highly reflecting focusing mirrors, each with a radius of curvature of 10 cm. The laser cavity was completed with a flat high reflector (HR) and a flat output coupler (OC). The cavity mirrors for the high reflectors, obtained from Excel, were nominally 100% reflecting over the spectral range 1350-1550 nm, while the output couplers, obtained from NRC, had a transmission of 1% or 2% from 1350 to 1550 nm.

For the astigmatically compensated cavity, the two focusing mirrors are tilted based on the requirements of tight focusing and on the cavity length. To achieve a small tight focused beam-waist, a simple two focusing mirror cavity must have a short focusing length,

which makes the overall cavity length small. The focusing mirrors are tilted so that the cavity length can be adjusted as required and other elements can be added into the cavity. When the focusing mirrors are used to focus light off axis, they introduce astigmatism because of the different paths encountered by the ray bundles in the sagittal and tangential planes [28, 29]. On the other hand, the Brewster-angled gain medium also introduces astigmatism. Astigmatism will distort the laser mode and affect stability. Fortunately, it is found that the mirror astigmatism is opposite to that introduced by the Brewster-angled gain medium. For a four-mirror laser system, the two focusing mirrors having both the same radius of curvature will each provide half of the astigmatism compensation for the Brewster-angled rod. The condition for exact astigmatic compensation is [29]

$$\cos\theta = \frac{t}{R}\left(\sqrt{\frac{N^2}{4} + \frac{R^2}{t^2}} - \frac{N}{2}\right) \qquad \text{Eq.4.4}$$

where θ is the folding angle, R is the fold mirror radius of curvature, t and n are the thickness and refractive index of the Brewster-angled medium, respectively and $N = (n^2 - 1)\sqrt{n^2 + 1}/n^4$. Hence, in order to fully compensate for the astigmatism induced by the tilted 2-cm-long Cr^{4+}:YAG crystal having an index of reflection of 1.81, the folding angle of the cavity was carefully chosen to be 33.5°
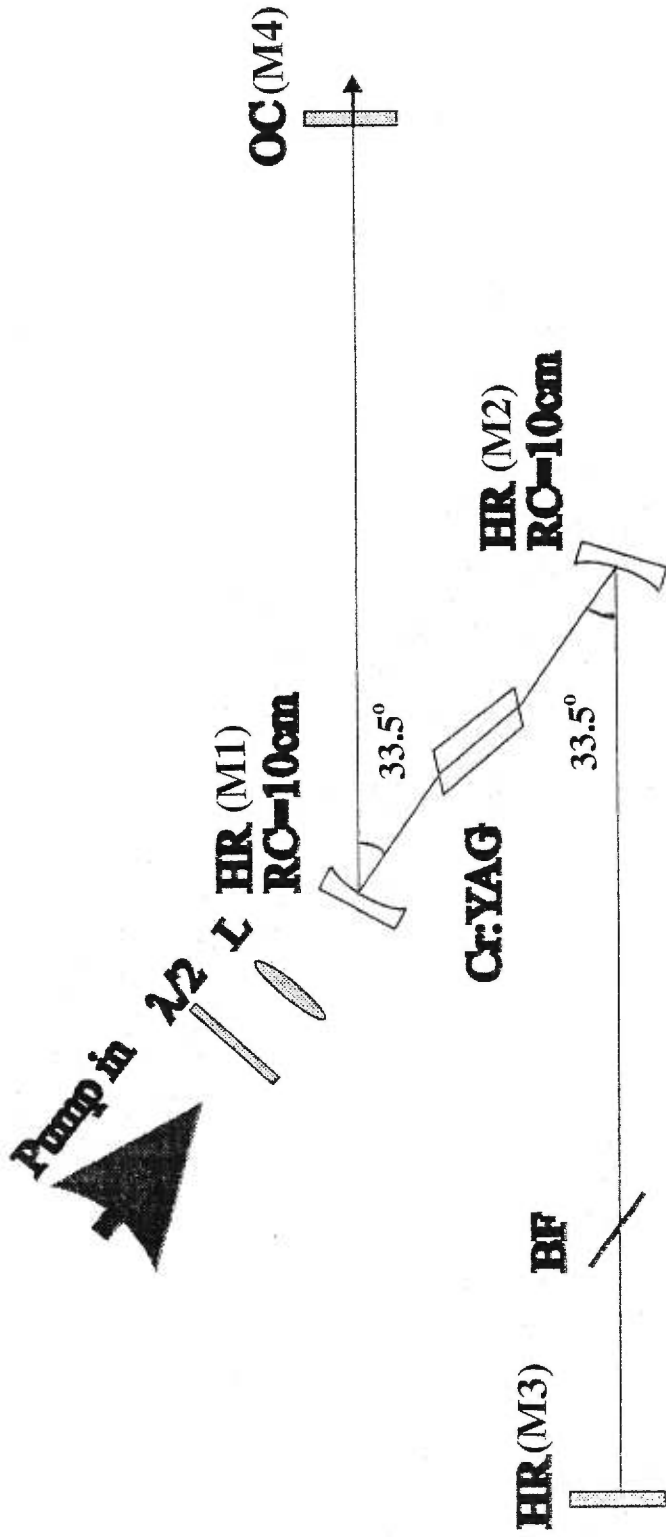
Fig. 4.4. Experimental setup of the cw Cr^{4+}:YAG laser. OC-output coupler; HR-broadband high reflector; BF-birefringent filter; RC-radius of curvature.

4.5. Laser cavity alignment

Compared with a Ti:sapphire laser, alignment of a Cr^{4+}:YAG cavity is more difficult. First, for the Ti:sapphire laser, the fluorescence ($\lambda = 780$ nm) from the pumped crystal, which is partially visible to the naked eye as red and can be seen clearly with an infrared viewer, is quite different from the blue pump Ar^+ laser ($\lambda = 488$ or 514.5 nm). This radiation can be used to adjust focusing mirrors, to collimate and retro-reflect the fluorescence to construct an efficient cavity. However, for a Cr^{4+}:YAG laser, its fluorescence (peak at 1450 nm) is invisible, and much dimmer since Cr^{4+}:YAG is a lightly doped crystal. Moreover, such a fluorescence is very hard to detect since the sensitivity of Ge detectors decreases when the wavelengths become longer. Both the Nd:YAG pump beam and Cr^{4+}:YAG fluorescence are infrared and invisible. The intensity of the unabsorbed pump beam is usually very high and the detectors are much more sensitive at 1.06 μm than at about 1.45 μm. So the Nd:YAG pump beam tends to swamp any Cr^{4+}:YAG fluorescence, which makes the Cr^{4+}:YAG laser hard to start.

Second, the thermal loading in a 2-cm Cr^{4+}:YAG crystal is more severe than in Ti:sapphire. The output power usually does not respond in a predictable way as expected from a Ti:sapphire due to the thermal lensing effect. The correct alignment can be easily missed if thermal lensing delays the onset of lasing. Third, since the absorption coefficient of Cr^{4+}:YAG is smaller than in Ti:sapphire, the laser crystal is usually 2 cm long in order to achieve an efficient (> 90%) absorption of the pump beam in the crystal. The gain medium placed at the Brewster angle shifts the laser beam by about 1 cm, which makes it difficult to collimate.

Since the fluorescence from the Cr^{4+}:YAG crystal is not easily detectable, the alignment of the cavity elements relies more on the Nd:YAG pump beam. In the laser cavity shown as Fig. 4.4, the pump beam is first aligned to be about 4.5" (i.e., about 11 cm) horizontally over the optical table along the center of the translation stages. Then, the mode-matching lens L and the first curved mirror M1 are added and adjusted to make no deviation of the beam when translated. The mirror M1 is set at the astigmatism correction angle of 33.5°. The Brewster-cut Cr^{4+}:YAG crystal is positioned such that the pump beam

is incident at the Brewster angle of about 61° (n = 1.81). To ensure that this is the correct angular orientation of the crystal, the reflection off the crystal surface for the p-polarized pump beam is set to be minimum. The distance between the front surface of the crystal and M1 is set to be about 4.65 cm, such that the laser beam waist is at the center of the Cr^{4+}:YAG crystal as calculated. Next, the second curved HR (M2) and the end-mirror output-coupler (M4) are put into position. The distance between M2 and the rear surface of the Cr^{4+}:YAG crystal is set to be 4.65 cm, while the distance between M1 and M4 is 26 cm. Mirror M2 retro-reflects the cavity beam and mirror M1 collimates the light to M4. The mirror M4 can be adjusted by retro-reflecting the residual pump light reflected off mirror M1. Once the mirror M4 is aligned, M2 is tilted parallel to M1 with an astigmatism correction angle of 33.5°. The end high reflector (M3) is then added and aligned to retro-reflect the residual pump beam.

Initial lasing is achieved by operating the pump at 50% duty cycle using an electronic-mechanical chopper. In order to ease up the alignment, a red He-Ne laser beam is sent collinear with the pump beam. Various optical elements in the cavity are then positioned and centered along the optical axis defined by the He-Ne beam. In this configuration, the approximate 1.4 μm fluorescence signal, monitored with a Ge detector, positioned at the back of the output coupler, is maximized by adjusting the positions of the two curved mirrors (M1 and M2) in the stability region of the cavity. Further improvement of this signal is straightforward by adjusting the two end flat mirrors (M3) and (M4) causing an overlap with the fluorescence signal. Lasing action is readily observed once all the mirrors are correctly positioned. Once lasing is obtained, further optimization of the laser output power can be carried out without chopping the pump beam. Critical positioning of the curved focusing mirrors and the pump focusing lens are essential for obtaining the best output power. The pump focusing mirror is adjusted in such a way as to have the maximum mode-matching of the pump and laser beams in the gain medium. During the optimization of the cw Cr^{4+}:YAG laser, special care was also taken to keep all the optics as clean as possible by occasionally cleaning every intracavity surface with lens tissue soaked in ethanol or methanol.

4.6 Characterization of the cw laser performance

4.6.1 Output power and slope efficiency

The crystal temperature was found to affect the laser performance significantly. Before the Cr^{4+}:YAG was operated, the laser crystal was left undisturbed for several minutes with circulating water, until thermal equilibrium was established. Special care was taken to ensure that the cooling water maintained the crystal at about $18°C$ during the laser experiments. The efficiency measurements were carried out with the Cr^{4+}:YAG operated in the free-running mode with no intracavity elements (such as the birefringent filter) other than the gain medium. The efficiency data were obtained by measuring the output power as a function of the input pump power. The pump laser power was varied by rotating a half-wave plate in combination with a cubic calcite polarizer. The pump and laser powers were measured by a calibrated power meter (Newport).
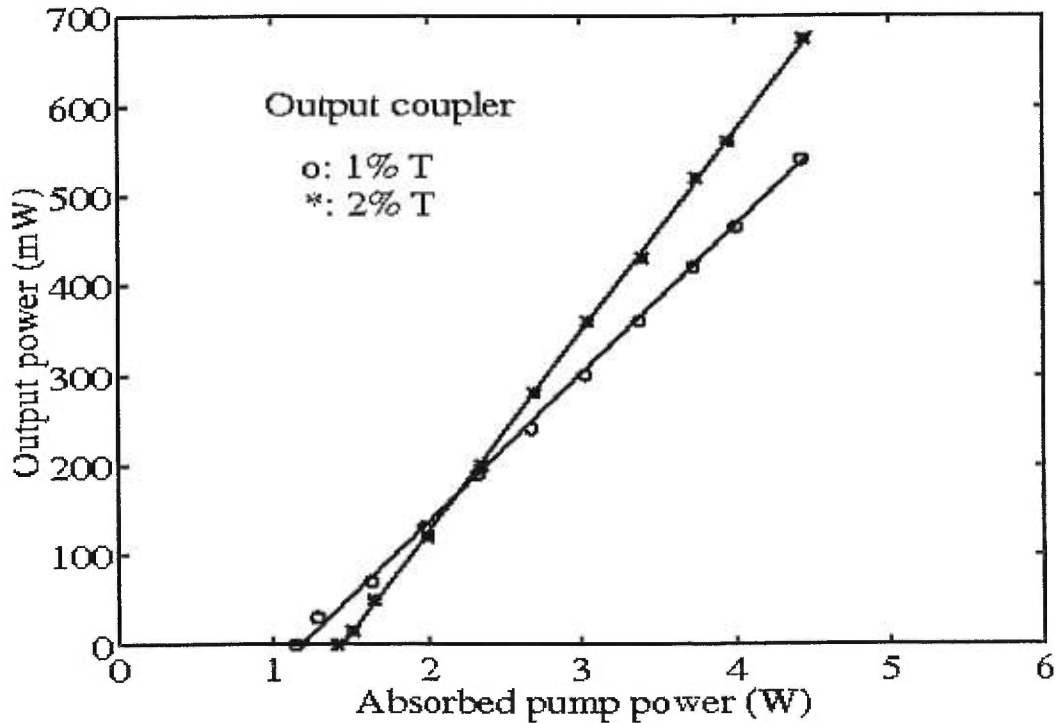
Fig. 4.5 The laser efficiency for Cr^{4+}:YAG at 1464 nm.

The laser emission in the free-running mode peaked at approximately 1.46 μm with a measured linewidth of 1.8 Å. Fig. 4.5 shows the variation of the output power as a function of the absorbed pump power for the 2% output coupler at room temperature. An output power of 590 mW was obtained at 1464 nm with a 1% output coupler at a pump power of 6.8 W, 4.9 W of which is absorbed. The absorbed threshold pump power was 1.13 W. A higher output power of 730 mW was obtained with 2% output coupling. The slope efficiency obtained for 2% output coupler was 22.3%, while that obtained for the 1% output coupler was 16.5%. These measurements were repeatable within 1%.

4.6.2 Laser tunability

The low output coupler for Cr^{4+}:YAG laser is needed because of the low gain nature of the gain medium, which makes the CW laser operation very susceptible to even small amounts of loss introduced into the cavity. The laser was tuned with a 0.75 mm birefringent plate which was inserted into the laser cavity at the Brewster angle ($\sim 56.8°$ for quartz). The birefringent filter obtained from Virgo Optics was a 45°-cut quartz plate, 0.75 mm thick and with a 30 mm diameter. It was custom-designed to tune the laser wavelength from 300 to 2000 nm, as shown from the simulated curves in Fig. 4.6. The birefringent plate gave a wavelength-dependent polarization rotation creating a wavelength dependent loss at the Brewster-angled surface in the cavity. The laser was tuned by adjusting the orientation of the plate (at the Brewster-angled surface) to change the wavelength which experiences the minimum loss. A Rees 202 laser spectrum analyzer served to conveniently identify the output wavelength for each setting of the birefringent filter.

Fig. 4.7 shows the tuning curve for two different output couplers (1% and 2%, respectively) using a 0.75 mm thick quartz birefringent filter. It is seen that the tuning range extends from at least 1345 nm to 1557 nm for a 1% output coupler. It is noted that this is the broadest range yet reported with one set of mirrors for a CW Cr^{4+}:YAG laser. For example, the results reported by Conlon et al. [16] for a similar laser cavity show a tuning range of 1.34 to 1.52 μm.
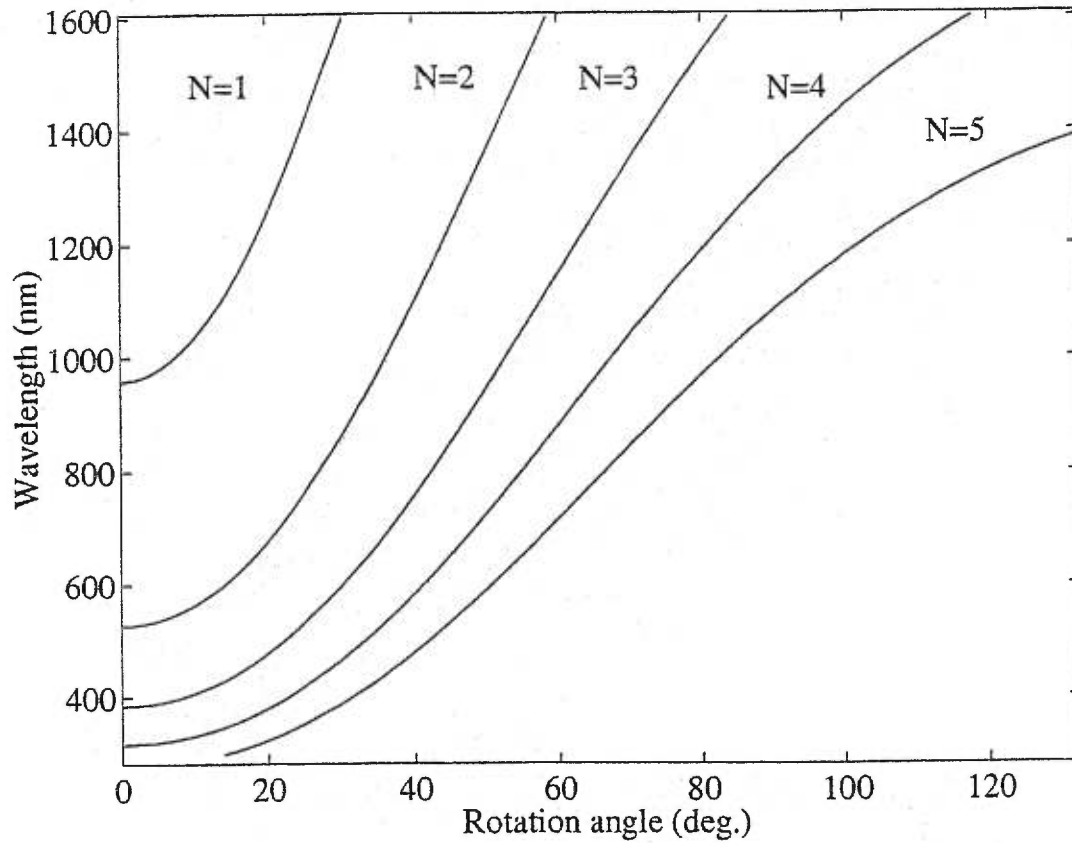
Fig. 4.6 Design curves for the 0.75-mm-thick birefringent filter. N is the order number related to the orientation of the optic axes and plate thickness.

The wavelengths on the shorter wavelength side are limited by the water absorption lines. The wavelength cannot be tuned smoothly and the laser cannot be forced to operate at certain wavelengths below about 1.47 μm, corresponding to the strong vibrational and rotational water absorption lines [31]. This was attributed to the absorption of the cavity beam by water vapour in ambient air. The strong dip in the vicinity of 1.38 μm in the tuning curve, Fig. 4.7, corresponds to the resonance of OH ions [16]. On the other hand, the laser could be tuned smoothly at wavelengths longer than 1.48 μm.
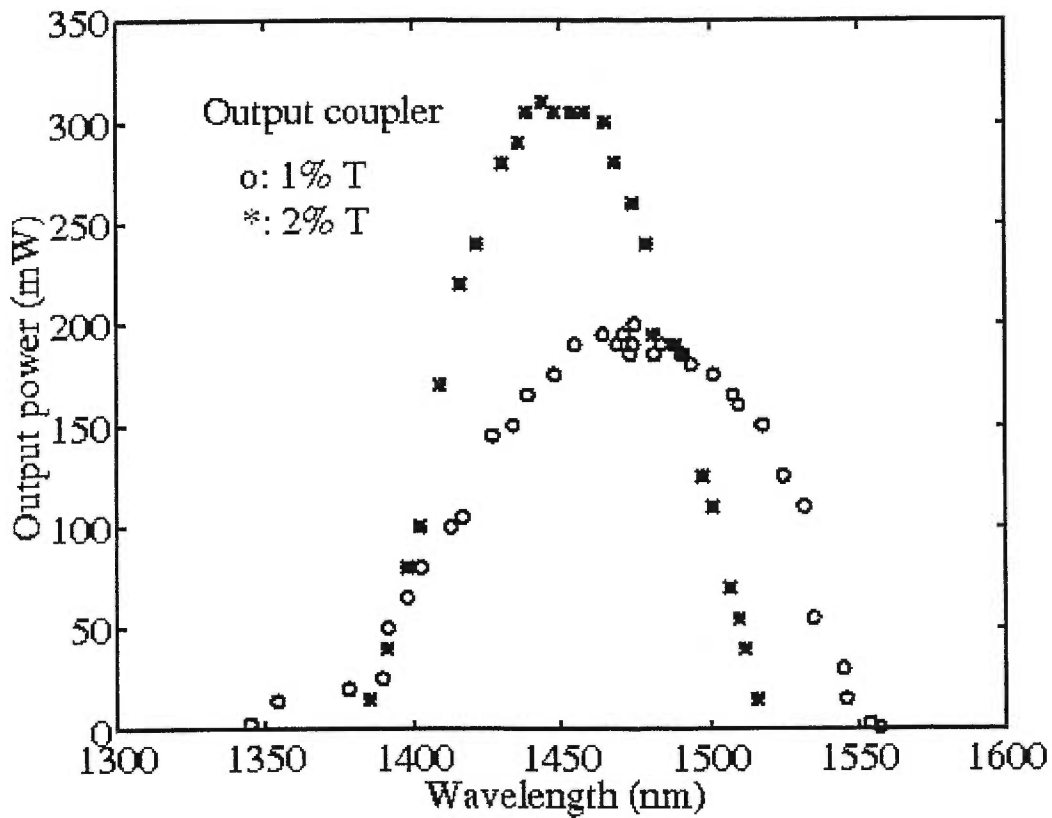
Fig. 4.7 The tuning curves of Cr^{4+}:YAG for two different output couplers.

4.6.3 Absorption saturation

In Cr^{4+}:YAG, a large number of chromium ions are in the 3+ valence state such that the concentration of Cr^{4+} active centres is relatively low. Because of the low doping of Cr^{4+} and the relatively long upper state lifetime (3.6 μs at 300 K), the pump beam will saturate the absorption of the crystal. The Cr^{4+}:YAG crystal has been previously used as a saturable absorber to passively Q-switch Nd lasers [8]. In the cw performance of the Cr^{4+}:YAG laser, the same pump saturation absorption phenomenon induces a decreasing absorption in the gain medium with an increasing pump power leading to output saturation.

The saturation absorption in Cr^{4+}:YAG can be demonstrated by measuring the transmission of the pump through the crystal. Fig. 4.8 shows the output pump power after the output coupler against the incident pump power. The slope of the curve gradually increases as the pump power increases, such that a smaller fraction of the pump beam is absorbed at higher powers.

The pump light absorption in Cr^{4+}:YAG also depends on whether the crystal is lasing or not. Fig. 4.8 compares the output pump power after the output coupler against the incident pump power both when the crystal is lasing and when it is not. The full circles were taken with the laser cavity blocked to prevent lasing while the open circles were taken with the system lasing. It is obvious that the absorption of the pump beam is significantly greater when the crystal rod is lasing. This is also confirmed by the absorption coefficient curve as shown in Fig. 4.9. The absorption coefficient of the crystal at small signal was determined to be 1.38 cm^{-1} at the pump wavelength 1.064 μm.

Such a change in absorption can be explained as follows. When the crystal is not lasing, the excited Cr^{4+} ions decay down to the ground state by non-radiative processes and spontaneous emission (fluorescence); when the crystal is lasing, stimulated emission provides another channel through which the excited Cr^{4+} centres can lose energy. The rate of stimulated emission depends on the intensity of the intracavity beam passing through the crystal and does not have a fixed lifetime associated with it like spontaneous emission. The extra decay channel provided by the lasing increases the population of the ground state
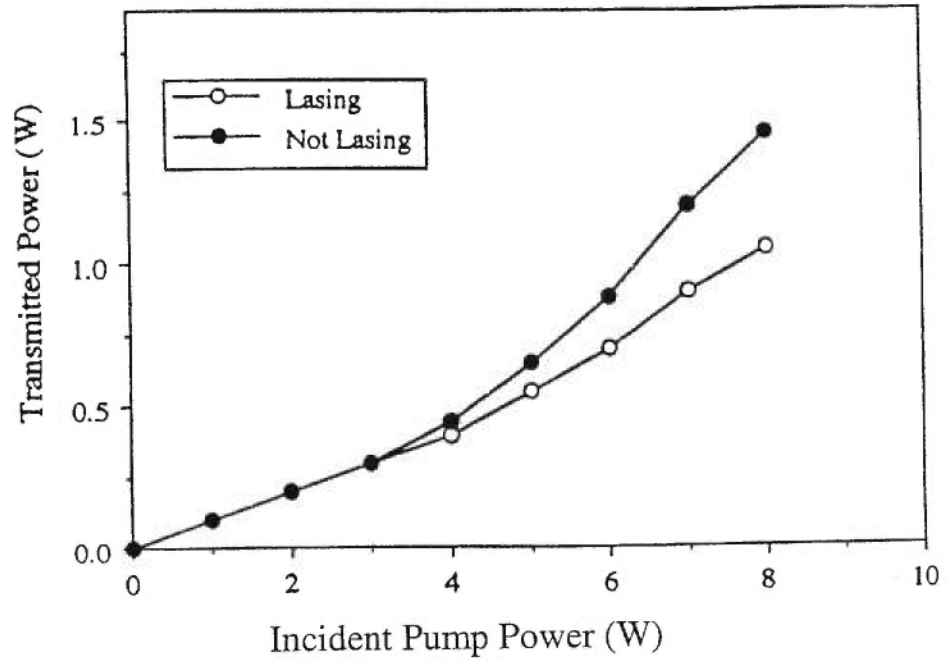
Fig. 4.8 Variation of the transmitted pumped power in the Cr^{4+}:YAG crystal when lasing and not lasing.
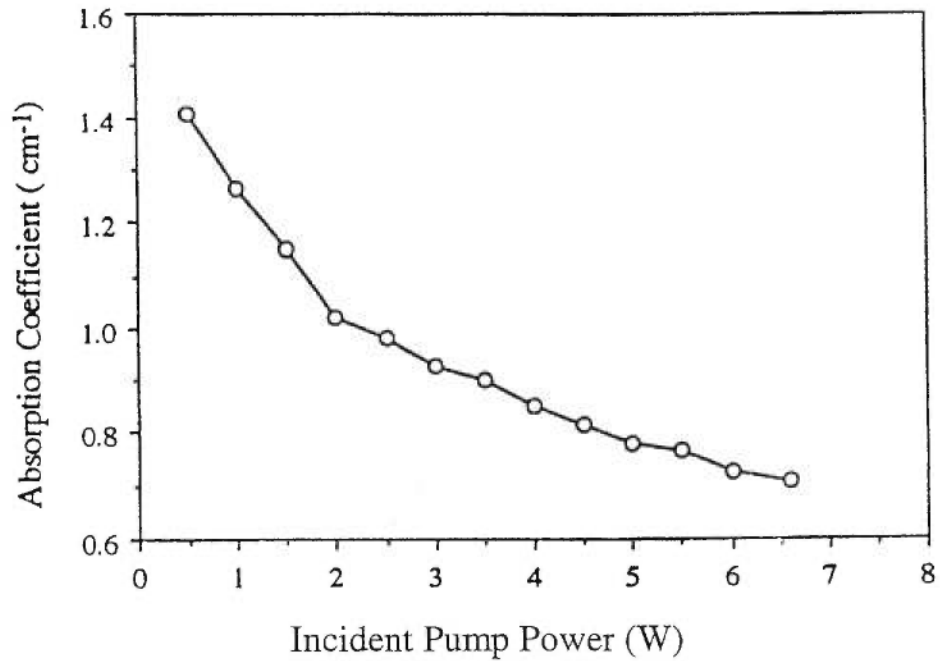
Fig. 4.9 Variation of the absorption coefficient as a function of the pump power in the Cr^{4+}:YAG laser.

compared to the non-lasing case such that the absorption of the pump beam becomes greater.

4.6.4 Thermal lensing effect in Cr^{4+}:YAG

For our Cr^{4+}:YAG laser, the 2-cm-long cylindrical gain medium is heated in the centre by the pump Nd:YAG beam and cooled at the periphery by the circulating water. This creates a radial temperature gradient. This temperature gradient sets up a stress pattern which produces a radial refractive index variation that acts like a lens, the so-called *thermal lens*. Thermal lensing is particularly troublesome when carrying out the cavity alignment. An adjustment which initially increases the power may settle down to give a lower power once the thermal lens of the crystal has adjusted itself. However, the effect that pump-induced thermal lensing has on the operation of a Cr^{4+}:YAG laser has received relatively little attention.

Thermal effects in Cr^{4+}:YAG can be demonstrated by comparing the performance of the laser when pumped by a CW beam and by a chopped beam. With the chopped beam (duty cycle of 50:1), the heat deposited by each flash of the pump light has enough time to disperse before the next one arrives, but with the unchopped beam, heat accumulates and a temperature gradient is set up. Fig. 4.10 shows the laser output power with a chopped pump beam (open circles) and a CW beam (asterisks). As the pump power increases, the difference between the output power with the chopped and unchopped pump beams becomes larger. The Cr^{4+}:YAG laser has an incident power threshold of about 2.5 W with the chopped beam. With the CW pump beam, the threshold becomes slightly higher approximately at 2.8 W, and the slope efficiency declines as the pump power increases. The laser output power could be increased slightly by adjusting one of the cavity focusing mirrors.

The thermal lensing effect was found to depend, not only on the pump power, but also on the laser power. If the cavity beam was interrupted for a moment when operating in the CW mode, the output power of the laser did not immediately return to the level it was at
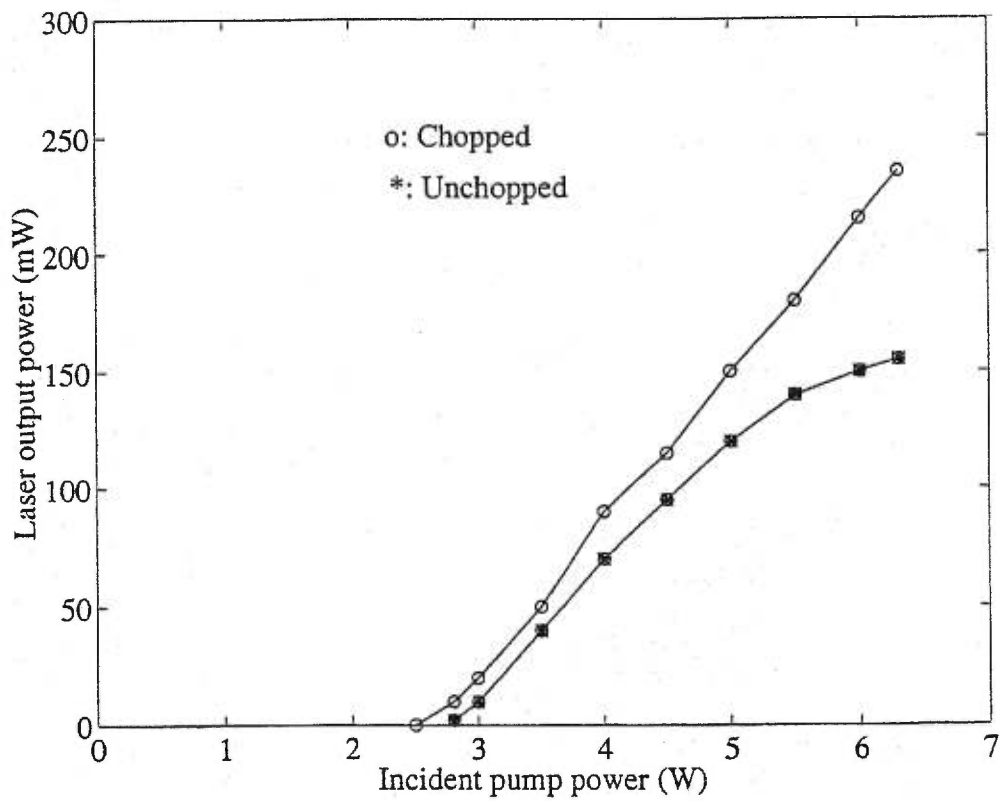
Fig. 4.10 Variation of the output power as a function of pump power for the
Cr^{4+}:YAG laser with a cw beam and a chopped beam.

before the interruption, but increased slowly taking between a few seconds and 1 minute to recover. On the contrary, if the pump beam was first chopped and then returned to CW, the lasing would usually recover. Such a phenomenon can be explained as follows. The pump power incident upon the crystal is not changed by blocking the laser beam and therefore the thermal gradient is not expected to change at all. The gradual recovery of the laser output power suggests that the thermal condition in the crystal is slowly changing and depends also on the lasing power.

For a solid-state laser rod longitudinally pumped by a second cw laser, an effective focal length for the rod can be estimated according to the model proposed by Innocenzi et al. [30] as follows

$$f = \frac{\pi k_c w_p^2}{P_{ph}(dn/dT)} \left(\frac{1}{1 - e^{-\alpha l}} \right) \qquad \text{Eq.4.5}$$

where k_c is the thermal conductivity of the laser rod, w_p is the $1/e^2$ Gaussian radius of the pump beam, P_{ph} is the pump power converted to heat, and α is the absorption coefficient. Employing $K_c = 0.13$ W/(cm K), $w_p = 100$ μm, $P_{ph} = 1$ W, dn/dT(YAG) $= 7.3 \times 10^{-6}$ K^{-1}, α $= 1.3$ cm^{-1}, $l = 2$ cm, a value of $f = 6.04$ cm is obtained. It is noted that this focal length is comparable to the tight focusing length in the Cr^{4+}:YAG laser cavity.

4.7 Estimation of the emission and ESA cross sections

As discussed previously, the presence of ESA due to the Cr^{4+} ions constitutes an intrinsic limit to the laser performance. The best output coupling was determined to be 1.7% by Spälter et al. [32]. This low-gain nature of Cr^{4+}:YAG gain medium is believed to be due to the existence of the ESA. The ESA cross-section can be estimated from laser performance. We adopted the laser model accounting for ESA reported by Payne et al. [33], describing the laser output depending on the material, cavity and pump-beam parameters. The laser output power P_o above the threshold pump power P_{pa}^{th} from a cw laser can be described as

94

$$P_o = \left[(\frac{\lambda_p}{\lambda_l})\eta_p(\frac{\sigma_e - \sigma_{esa}}{\sigma_e})(\frac{T}{T+L}) \right](P_{pa} - P_{pa}^{th})$$

$$= \eta_s(P_{pa} - P_{pa}^{th}), \qquad \text{Eq.4.6}$$

where η_s is the slope efficiency, and λ_p and λ_l are the wavelengths of the pump and the lasing beam, respectively. The ratio λ_p/λ_l represents the quantum-defect-limited slope efficiency, η_p is the pumping efficiency, i.e. the fraction of the absorbed pump photons that populate the upper level. η_p is taken to be 1 since there is only a single type of Cr^{4+} centre and no nonradiative decay comparable with the fluorescence lifetime. σ_e and σ_{esa} are the stimulated-emission and ESA cross-section at the lasing wavelength. The term σ_e-σ_{esa} represents an effective cross-section. T is the transmission of the output coupler, L is the total round-trip passive-cavity loss, and P_{pa} is the pump power absorbed by the sample.

The threshold absorbed pump-power P_{pa}^{th} is described by [33]

$$P_{pa}^{th} = \frac{\pi(w_p^2 + w_l^2)h\upsilon_p(T + L)}{4(\sigma_e - \sigma_{esa})\tau_f\eta_p}, \qquad \text{Eq.4.7}$$

where τ_f is the emission lifetime, $h\upsilon_p$ the pump photon energy, and w_p and w_l, the waists of the pump and lasing beams, respectively. From the slope efficiency in Eq.4.6 and the threshold power in Eq.4.7, one can see that, with the increasing excited-state absorption σ_{esa} and total loss L, the slope efficiency decreases, whereas the threshold power increases. Also the threshold power depends explicitly on the parameters w_p and w_l, whereas the slope efficiency is independent of them.

Using Eqs.4.6 and 4.7, one can easily find the emission and the ESA cross-sections, in terms of the threshold power and slope efficiency for given cavity, pump and material parameters. Based on the fact that the threshold power is proportional to the sum of the output-coupler transmission and round-trip cavity loss, the round-trip cavity loss is calculated to be 2.48%. We assume a constant beam profile inside the gain medium. The pump and laser beam radii have average values about 70 μm and 60 μm, respectively. Table 4.2 lists the calculated values of σ_e and the ratio σ_{esa}/σ_e. For a 2% output coupler,

the ESA cross-section is approximately 30% of the emission cross-section, in agreement with previously reported values [13, 34].

Table 4.2 The emission cross-section σ_e and the ratio of the ESA cross-sections to σ_e calculated for two sets of the cw laser efficiency data.

Temp(°C)	$T(\%)$	P_{pa}^{th} (W)	η_s (%)	$\eta_0(\%)$	σ_e (10^{-19}cm^2)	σ_{esa}/σ_e
23	1.0	1.124	16.5	57	1.48	0.209
23	2.0	1.447	22.3	50	1.69	0.312

In order to consider the effect of ESA explicitly, one may rewrite η_s in terms of the intrinsic slope efficiency η_0 as:

$$\eta_s = \eta_0 \frac{T}{T + L} \qquad \text{Eq.4.8}$$

where the passive loss was separated out. Using the experimental values of T and η_s, η_0 is calculated to be 50% for the 2% output coupler. Compared with the quantum-defect-limiting value of 73%, the measured intrinsic slope-efficiency of 50% suggests that the ESA provides a non-negligible loss in Cr^{4+}:YAG laser.

4.8 Summary

In this chapter, the cw power performance of a Cr^{4+}:YAG laser is characterized and several unique properties are identified. A broad tuning range of 210 nm, i.e, from 1345 to 1557 nm, are demonstrated by means of one set of mirrors with useful cw output power of as high as 730 mW at 1.46 μm (the Nd:YAG pump power of about 6.5 W). The lasing action is found to be strongly influenced by the temperature of the crystal and the combined effects of thermal lensing and saturable absorption of the pump beam.

4.9 References

1. Walling J.C., Benson H.P., Morris R.C., O'Dell E.W. and Peterson D.G., Opt. Lett. **4**, 182 (1979).

2. Shand M.L. and Lai S.T., IEEE J. Quantum Electron. **20**, 105 (1984).

3. Dayne S.A., Chase L.L., New K.K., Smith L.K. and Kmpke W.F., IEEE J Quantum Electron. **24**, 2243 (1988).

4. Dayne S.A., Chase L.L., Smith L.K., Kway W.L. and Newkirk H.W., J. Appl. Phys. **66**, 1051 (1989).

5. Petricevic V., Gayen S.K. and Alfano R.R., Appl. Phys. Lett. **52**, 1040 (1988).

6. Angert N.B., Borodin N.I., Garmash V.M., Zhitnyuk V.A. and Okirimchuk A.G., Sov. J. Quantum Electron. **18**, 73 (1988).

7. Chai B.H.T., Shimony Y., Deka C., Zhang X.X., Munin E. and Bass M., in *OSA proceedings on advanced solid state lasers*, L.L. Chase and A.A. Pinto eds. (OSA, Washington D.C., 1992), **13**, p.28.

8. Miller I.J., Alcock A.J. and Bernard J.E., in *OSA Proceedings on Advanced Solid State Lasers*, L.L. Chase and A.A. Pinto eds. (OSA, Washington D.C., 1992), **13**, p.322.

9. Borodin N.I., Zhitnyuk V.A., Okhrimchuk A.G. and Shestakov A.V., Izv. Akad. Nank. SSSR Ser. Fiz. **54**, 1500 (1990).

10. Jia W., Eilers H., Dennis W.M., Yen W.M., and Shestakov A.V., in *OSA proceedings on advanced solid state lasers*, L.L. Chase and A.A. Pinto eds. (OSA, Washington D.C., 1992), **13**, p.31.

11. Sennaroglu A, Pollock C.R. and Nathel H., J. Opt. Soc. Am. B **12**, 930-7 (1995).

12. Shestakov A.V., Borodin N.I., Zhitnyuk V.A., Ohrimtchynk A.G. and Gapontsev V.P., *"Tunable Cr^{4+}: YAG lasers"*, in *Technical Digest of Conference on Lasers and Electro-Optics* (Optical Society of America, Washington, DC, 1991), paper CPDP11.

13. French P.M.W., Rizvi N.H., Taylor J.R. and Shestakov A.V., Opt. Lett. **18**, 391 (1993).

14. Ishida Y. and Naganuma K., Opt. Lett. **19**, 2003 (1994).

15. Sennaroglu A., Pollock C.R. and Nathel H., Opt. Lett. **19**, 390 (1994).

16. Colon P.J., Tong Y.P., French P.M.W., Taylor J.R. and Shestakov A.V., Opt. Lett. **19**, 1468 (1994).

17. Tong Y.P., Sutherland J.M., French P.M.W., Taylor J.R., Shestakov A.V. and Chai B.H.T., Opt. Lett. **21**, 644 (1996).

18. Collings B.C., Bergman K. and Knox W.H., Opt. Lett. **22**, 1098 (1997).

19. Hayduk M.J., Johns S.T., Krol M.F., Pollock C.R. and Leavitt R.P., Opt. Commun. **137**, 55 (1997).

20. Chang Y., Maciejko R., Leonelli R. and SpringThorpe A., Appl. Phys. Lett. **73**, 2098 (1998).

21. Spaniosu K., Chen W., Stultz R., Birnbaum M. and Shestakov A.V., Opt. Lett. **18**, 814 (1993).

22. Kück S., Petermann K. and Huber G., in *OSA Proceedings on Advanced Solid State Lasers*, L.L. Chase and A.A. Pinto eds. (OSA, Washington D.C., 1991), **10**, p.92.

23. Eilers H., Hommerich V., Jacobsen S.M. and Yen W.M., Phys. Rev. B **49**, 15505 (1994).

24. Borodin N.I, Okhrimchuk A.G. and Shestakov A.V., in *OSA Proceedings on Advanced Solid State Lasers*, L.L. Chase and A.A. Pinto eds. (OSA, Washington D.C., 1992), **13**, p.42.

25. Okhrimchuk A.G. and Shestakov A.V., Opt. Mater. **3**, 1 (1994).

26. Siegman A.E., *Lasers*, (University Science Books, Mill Valley, 1986).

27. Gerrard A and Burch J.M., *Introduction to matrix method in optics*, (John Wiley & Sons, 1994).

28. Hanna D.C., IEEE J. Quantum Electron. **5**, 483 (1969).

29. Kogelink H.W., Ippen E.P., Dienes A. and Shank C.V., IEEE J. Quantum Electron. **8**, 373 (1972).

30. Innocenzi M.E., Yura H.T., Fincher C.L. and Fields R.A., Appl. Phys. Lett. **56**, 1831 (1990).

31. Gilmore, O.A., Cvijin P.V. and Atkinson G.H., "Intracavity laser spectroscopy in the 1.38 - 1.55 µm spectral region using a multimode Cr^{4+}:YAG laser", Opt. Commun. **103**, 370-4 (1993).

32. Spälter S., Bohm M., Burk M., Mikulla M., Fluck R., Jung L.D., Zhang G., Keller U., Sizmann A. and Lenchs G., "*Self-starting soliton-modelocked femtosecond Cr^{4+}:YAG laser using an antiresonant Fabry-Perot saturable absorber*", Appl. Phys. B **65**, 335-8 (1997).

33. Payne S.A., Chase L.L., Newkirk H.W., Smith L.K. and Krupke W.F., "*$LiGaAlF_6$:Cr^{3+}: a promising new solid state laser material*", IEEE J. Quantum Electron. **24**, 2243-52 (1988).

34. Borodin N.I., Zhitnynk V.A., Okhrimchuk A.G. and Shestakov A.V., "*Oscillation of a $Y_3Al_5O_{12}$:Cr^{4+} laser in wavelength region of 1.34 - 1.6 µm*", Izv. Akad. Nauk SSSR Ser. Fiz. **54**, 1500-6 (1990).

Chapter 5

Self-starting tunable Cr^{4+}:YAG laser passively mode-locked by saturable Bragg reflector

In this chapter, a self-starting passive mode-locked Cr^{4+}:YAG laser using a saturable Bragg reflector with a single prism for dispersion compensation, instead of the standard prism pair, was investigated. For mode-locking, a strained InGaAs/InAlAs saturable Bragg reflector (**SBR**) was fabricated from layers grown by molecular beam epitaxy (**MBE**). The device consisted of nominally 25 periods of a GaAs/AlAs Bragg-reflector structure incorporating double InGaAs/InAlAs quantum-wells which are latticed-matched to InP. The SBR was more than 99.5% reflecting from 1410 to 1525 nm. We observed over 230 mW average output power with a pulse width of 400 fs at centre wavelengths shorter than 1.5 μm. The tuning range for cw laser operation extended from 1345 to 1557 nm. The modelocked pulses were self-starting and tunable from 1420 to 1510 nm by means of lossless prism tuning without aperture. The structural parameters for the sample were obtained using high-resolution x-ray diffraction rocking curves. The quantum-wells contained partially relaxed interfaces with the relaxation characterized by misfit dislocations. The photoluminescence measurements showed a lack of well-defined band edges and exciton structure at room temperature, indicating poor linear optical response. The fast recovery of the SBR nonlinear response was explained by the dislocations which act as non-radiative recombination centres.

5.1 Introduction

Recently, there has been a great interest in mode-locking Cr^{4+}:YAG lasers for ultrashort pulse generation at the telecommunications wavelength 1.5 μm with possible applications to the study of nonlinear phenomena in optical fibers and high-speed photonic devices. Sub-100 fs pulses from Cr^{4+}:YAG lasers have been demonstrated using Kerr-lens mode-locking (KLM) with an external initiative action, such as a regenerative modelocker

[1] or a shaking mirror [2,3]. Based on the critical-cavity alignment technique of Gerullo et al. [4], self-starting KLM has also been observed with 50-fs long pulses at 1.54 μm [5], but with low stability and in the presence of a cw component. KLM has been achieved by an intensity-dependent gain modulation based on the self-focusing effect, which requires critical cavity design and alignment. This approach is normally subject to environmental perturbations, such as mechanical vibrations and pump power fluctuations. More recently, an alternative method of mode-locking has received increasing attention. It relies on semiconductor saturable absorbers with Bragg-reflector mirrors. This technique, which eliminates the need for critical cavity alignment, simplifies the mode-locking operation of the Cr^{4+}:YAG laser, rendering it a practical ultrafast laser source. Demonstrated structures include saturable Bragg-reflectors (SBR) [6-8] and antiresonant Fabry-Perot saturable absorbers (A-FPSA) [9]. Sub-200 fs pulses at output powers less than 100 mW were achieved with centre wavelengths above 1.5 μm with the help of a prism pair for dispersion compensation. The use of only one intracavity prism for wavelength tunability and compensation has been demonstrated for a dye ring laser [10] and a Nd:glass laser [11]. Compared with the standard prism-pair cavities, a single-prism laser cavity is much simpler to align and the losses are reduced as a result of fewer intracavity elements and lossless wavelength tunability. This new dispersion compensation technique can be very useful for the development of novel compact and high repetition-rate femtosecond sources, as demonstrated in Ti:Sapphire by using a prismatic output coupler [12]. In this chapter, we report a cavity design which incorporates the one intracavity prism configuration and uses a saturable Bragg-reflector to mode-lock a Cr^{4+}:YAG laser. We demonstrate self-starting and stable subpicosecond pulses widely tunable from 1420 to 1510 nm with an output power as high as 230 mW.
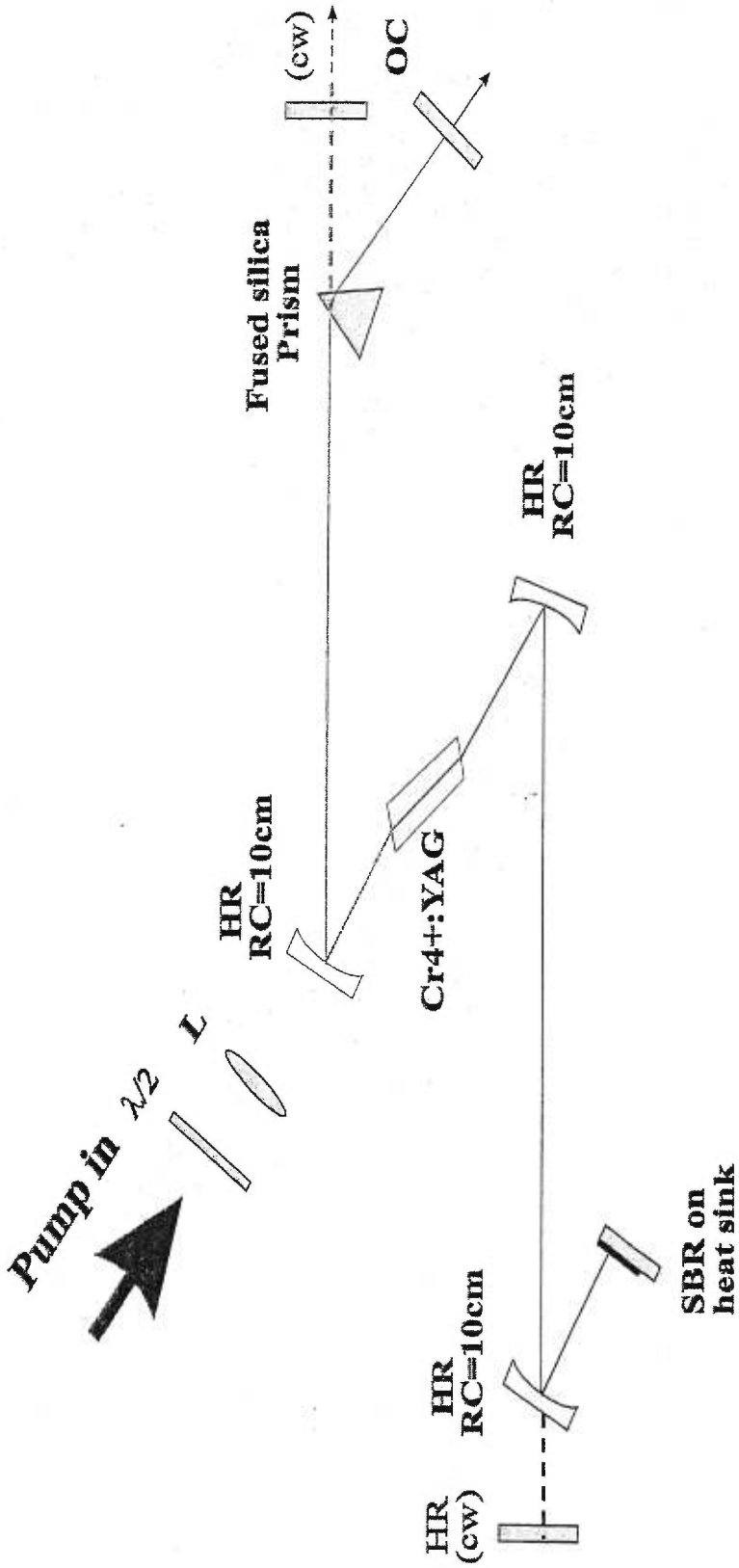
Fig. 5.1 Schematic of the self-starting Cr^{4+}:YAG laser with the SBR. OC, output coupler;

HR, broadband high reflector; RC, radius of curvature.

102

5.2 Experimental setup

The layout of the Cr^{4+}:YAG laser resonator is shown in Fig. 5.1. The Brewster-cut, 5 mm x 20 mm Cr^{4+}:YAG crystal rod (IRE-Polus) is placed between two 10-cm radius concave mirrors for tight focusing. The crystal is wrapped with indium foil and clamped to a water-cooled copper heat sink, and the crystal holder temperature is maintained at about 18°C. At one end of the cavity, a flat-wedged output coupler (NRC) of either 1% or 2% transmission from 1350 to 1550 nm is used. At the other end, the SBR is placed at the focus of a concave high reflector (**HR**). A 3-inch-diameter SBR wafer is cleaved into small pieces, and soldered with indium to a copper mount for heat sinking. The high reflectors (Excel) are normally 100% reflecting from 1350 to 1650 nm. A cw Nd:YAG laser (Spectra Physics M3460) delivering about 7 W of linearly polarized 1064 nm pump power is focused onto the laser crystal by a 10 cm focal length, AR coated plane-convex lens. The lens makes an angle of about 5° with respect to the normal in order to improve the overlap between the pump beam and the cavity mode. A small-signal absorption coefficient of 1.35 cm^{-1} for the gain medium was measured at the pump wavelength. A total of 72% of the pump power is estimated to be absorbed. The resonator is roughly symmetrical with an overall cavity length of approximately 0.98 m, corresponding to a repetition rate of 152 MHz.

5.3 Structure of the saturable Bragg-reflector (SBR)

The device structure is shown in Fig. 5.2(a), which is similar to the design first proposed by Hayduk et al. [7]. The slight difference is that we design the heavy hole exciton absorption of this device at 1.5 µm instead of 1.52 µm. It was grown by molecular beam epitaxy (**MBE**) on an undoped (100) GaAs substrate using a VG-Semicon V80-H MBE system (Nortel). The cracked AsH_3 and PH_3 were used as the group V sources while the group III sources were elements in nature. The Bragg reflector consists of 25 periods of alternating quarter-wave layers of AlAs (low index) and GaAs (high index). GaAs (lattice a = 5.6533 Å) and AlAs (a = 5.6622 Å) are almost lattice matched and have a high

ratio of refractive indices (on the order of 0.34 at 1.5 μm). Moreover, since GaAs and AlAs are transparent from 1.0 to 1.6 μm, a relatively wide reflectivity band can be obtained. GaAs/AlAs Bragg reflectors have been widely used for long wavelength (1.3/1.55 μm) vertical surface emitting lasers, which exhibit a low threshold current and cw operation [13]. To produce the nonlinear reflectivity required for mode-locking, two quantum wells are introduced into the Bragg reflector. They are located on the top of the GaAs/AlAs high-low index layers and embedded in an $Al_{0.48}In_{0.52}As$ quarter-wave layer. They consist of two 6.7 nm $Ga_{0.47}In_{0.53}As$ QWs separated by an 8 nm $Al_{0.48}In_{0.52}As$ barrier [14]. $Ga_{0.47}In_{0.53}As/Al_{0.48}In_{0.52}As$ QWs are lattice matched to InP (a = 5.8689 Å). Their excitonic resonances vary from 1.0 to 1.6 μm depending on the $Ga_{0.47}In_{0.53}As$ well thickness. To provide the saturable absorption nonlinearity for the Cr^{4+}:YAG laser, the $Ga_{0.47}In_{0.53}As$ well width is chosen to have its heavy hole exciton absorption at 1.5 μm. For a low saturation intensity due to bandfilling, the double QW layers are located near the distribution peak of the electric-field standing-wave at the top layer. A low temperature growth technique is employed such that an interface containing a high number of dislocations is formed between the Bragg reflector structure and the QW barrier buffer layer. Low temperature growth has been demonstrated to substantially reduce the recombination carrier-lifetime from the nanosecond to subpicosecond regime [11]. The reflectivity spectrum of the resulting SBR is shown in Fig. 5.2(b). The measured reflectance is larger than 99.5% from 1410 to 1525 nm. The peak reflectance is centred at 1470 nm, slightly blue shifted compared with the design due to strain effects. Even through there is a mismatch of 3.7% between GaAs/AlAs and $Ga_{0.47}In_{0.53}As/Al_{0.48}In_{0.52}As$, in the experiments, such strain is believed to result in a fast recovery of the SBR nonlinear response as discussed below. However, surface degradation with reduced reflectivity as a result of the induced strain is not observed [7]. The unsaturated insertion loss was estimated to be 2.4%. The saturation intensity was approximately 0.6 pJ/μm^2.
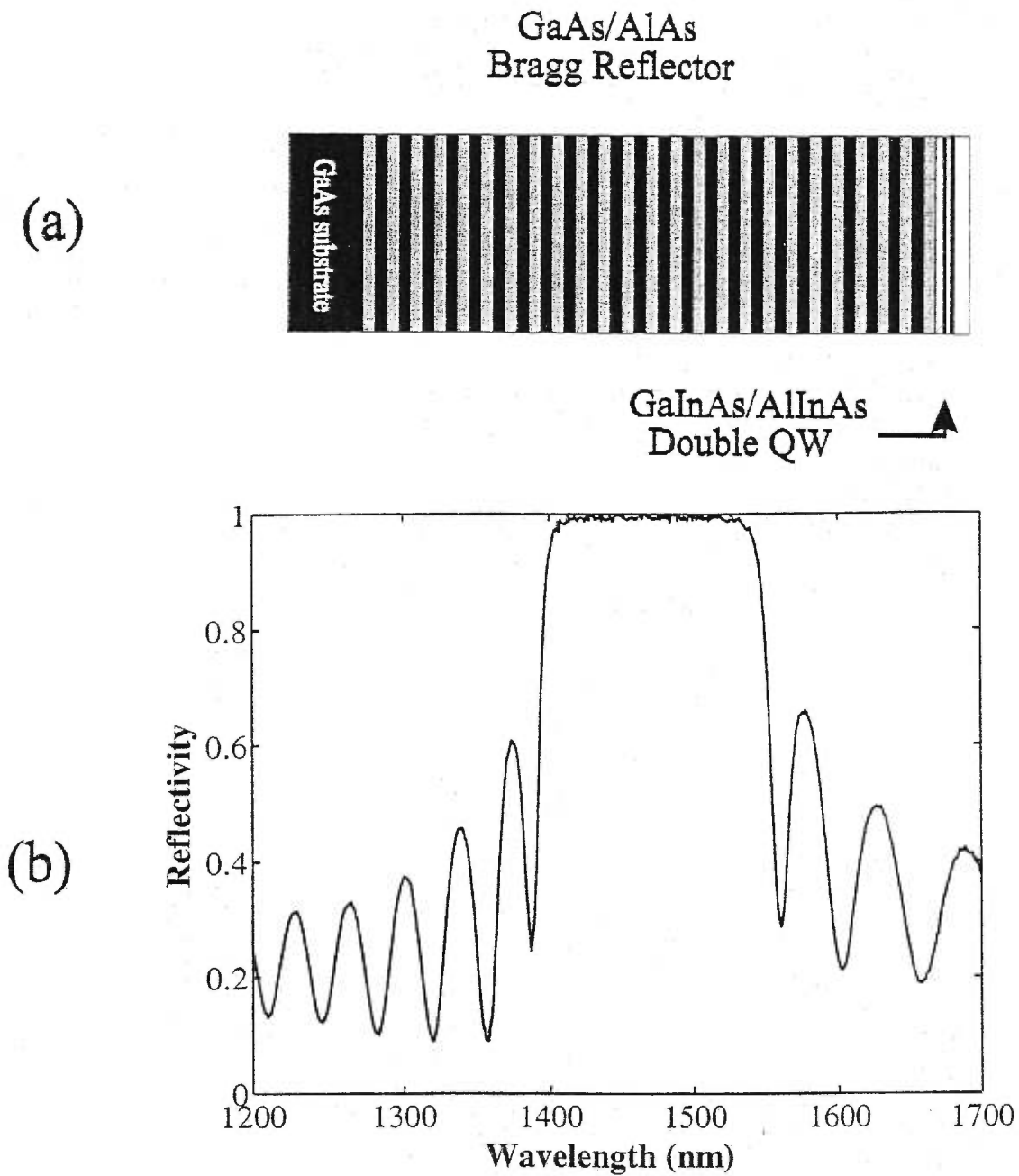
Fig. 5.2 (a) Low-loss SBR structure with a stack of GaAs/AlAs high-low index pairs and double $Ga_{0.47}In_{0.53}As/Al_{0.48}In_{0.52}As$ quantum wells buried in the top layer and (b) the reflection spectrum. The SBR has a peak reflectivity of more than 99.5% from 1410 to 1525 nm.

5.4 Dispersion analysis and control in the Cr^{4+}:YAG cavity.

The ability to control dispersion in a femtosecond resonator is important because of the wide bandwidths associated with ultrashort pulses. If the different spectral components travel at different speeds, the dispersion can broaden a pulse and limit the minimum duration that can be achieved. Therefore a thorough knowledge of the gain medium dispersion charateristics is required. Appendix I lists the dispersion equations for the Cr^{4+}:YAG medium. By calculating the second- and third-order dispersion constants with these data, the correct prism configuration to provide compensation for the phase distortion can be chosen. The variation of n_{YAG} as a function of wavelength (in μm) is provided in Fig. 5.3. Based on this equation, Fig. 5.4 shows the variation of the second-order phase distortion ϕ'', for a 2 cm long YAG crystal, calculated with the relation

$$\phi '' = \frac{d^2\phi}{d\omega^2} = \frac{\lambda^3}{2\pi c^2} l_c \frac{d^2 n_{YAG}}{d\lambda^2} \qquad \text{Eq.5.1}$$

In Eq.5.1, l_c is the length of the YAG crystal for one cavity round trip and c is the speed of light. Fig. 5.4 shows that Cr^{4+}:YAG is positively dispersive over its lasing range (see Chapter 2) with a zero at around 1.581 μm, such that negative dispersion compensation is required to generate femtosecond pulses.

Martinez et al. [16] first showed that the angular dispersion of a prism is negative irrespective of the material dispersion. Gorden et al. [17] later suggested that the dispersion could be continuously varied by translating the prism along its bisector to adjust the glass path and use the positive material dispersion to counter some of the negative angular dispersion. Fig. 5.5 shows a prism pair, consisting of two identical dispersive prisms made of the same material. As shown by Fork et al. [18], such a configuration can be used for obtaining an adjustable amount of dispersion from positive to negative without changing the path of the laser beam in the cavity.
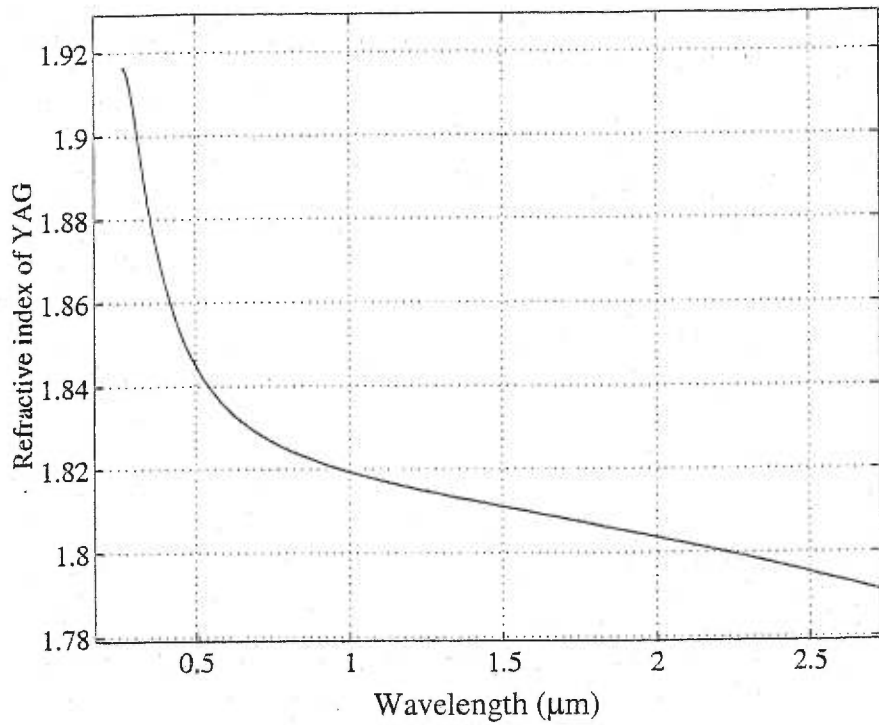
Fig. 5.3 Variation of the index of refraction of the YAG crystal as a function of wavelength.
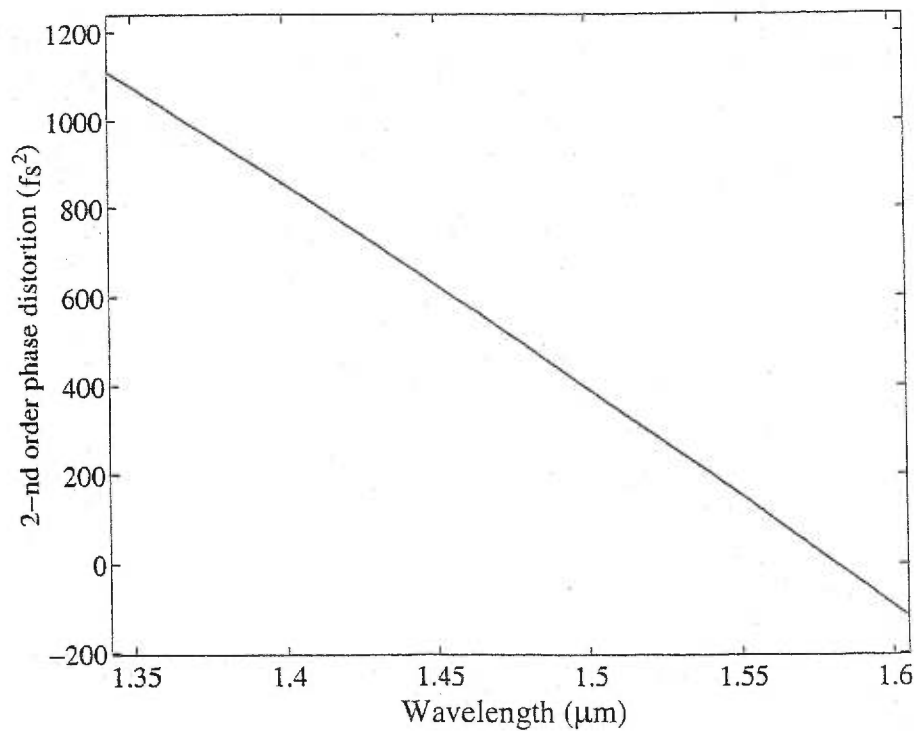
Fig. 5.4 Variation of the second-order phase distortion for a 2-cm-long YAG crystal for one cavity round-trip as a function of wavelength.

If the prisms are Brewster-cut and positioned at minimum deviation (which also ensures incidence at Brewster's angle), the second- and third-order wavelength derivatives of the path length for one cavity round trip are given by [18-19].

$$\frac{\partial^2 P}{\partial \lambda^2} = 4l\left\{[\frac{d^2 n}{d\lambda^2} + (2n - \frac{1}{n^3})(\frac{dn}{d\lambda})^2]\sin\beta - 2(\frac{dn}{d\lambda})^2\cos\beta\right\}$$

$$\frac{\partial^3 P}{\partial \lambda^3} \cong 4l\left\{\frac{d^3 n}{d\lambda^3}\sin\beta - 6\frac{dn}{d\lambda}\frac{d^3 n}{d\lambda^3}\cos\beta\right\}$$

Eq.5.2

where n is the index of refraction of the prism material, β is the angular spread of the dispersed beam, and l is the separation of the prisms (see Fig. 5.5). From the relationship between the acquired phase of a pulse and the optical path, i.e, $\phi = \frac{2\pi}{\lambda}P$, the second- and third- order phase distortions are given by [18, 19].

$$\frac{\partial^2 \phi_P}{\partial \omega^2} = \frac{\lambda^3}{2\pi c^2}\frac{\partial^2 P}{\partial \lambda^2}$$

$$\frac{\partial^3 \phi_P}{\partial \omega^3} \cong \frac{-\lambda^4}{4\pi^2 c^3}(3\frac{\partial^2 P}{\partial \lambda^2} + \lambda\frac{\partial^3 P}{\partial \lambda^3})$$

Eq.5.3

Usually, $l\sin\beta$ is of the order of twice the spot size of the beam, and $l\cos\beta \sim l$. With these approximations, one sees that the terms containing $\cos\beta$ dominate, and give a negative contribution to GVD for sufficiently large prism separation.

Fig. 5.5 Schematic of prism pair configuration to provide adjustable negative GVD

The length of the prism sequence is an important constraint when building a femtosecond laser. Fig. 5.6 shows the variation of the net second- and third-order phase distortion ϕ_{net}'' and ϕ_{net}''' for one cavity round trip at 1.5 μm as a funct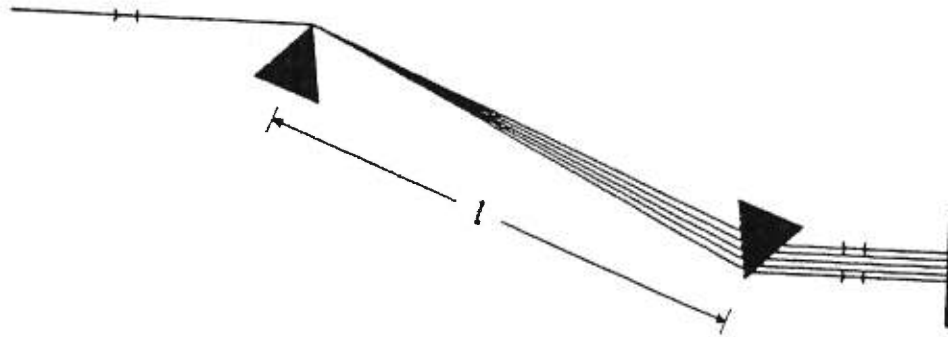ion of fused silica prism separation l_p. In Fig. 5.6, ϕ_{net}'' and ϕ_{net}''' take into account the contributions of the fused silica prism pair and the gain medium according to

$$\phi_{net}'' = \phi_{prism}'' + \phi_{YAG}'' \text{ and } \phi_{net}''' = \phi_{prism}''' + \phi_{YAG}''' \qquad \text{Eq.5.4}$$

In the experiments described below, stable mode-locked operation was readily achieved equvalently for prism separation in the neighbourhood of 30 cm. The calculated net second-order cavity dispersion for a 30-cm prism separation at 1.5 μm (for synthetic fused silica material) was − 2000 fs², comparable to what is observed in Ti:sapphire lasers operating with similar pulsewidths. Fig. 5.7 shows the variation of the net second-order and third-order phase distortion ϕ_{net}'' and ϕ_{net}''' for one cavity round trip at fused silica prism separation of 30 cm as a function of wavelength. The major problem with the fused silica prisms in this wavelength region has to do with their positive third-order phase distortion. This quantity, being of the same sign as that of the gain medium, gives rise to a large net third-order phase distortion in the cavity without any cancellation, as depicted in Fig. 5.6(b).

For the work described in this chapter, the positive dispersion, e.g. approximately +10 fs²/mm for the Cr⁴⁺:YAG material at 1.5 μm, was compensated by a single Brewster prism. The use of a single prism for adjustable compensation was analyzed by Kopf et al. [11]. The single prism cavity exhibits net negative dispersion because the propagation axes of different wavelengths follow spatially self-consistent optical paths [12]. This relative displacement of the propagation axes results from the wavelength dependence of the angular deviation at the Brewster surface of the gain medium in terms of simple ray optics. The general outline of the single prism cavity is shown in Fig. 5.8. The cavity is divided into two sections. One side has a single dispersive prism close to a flat end mirror (EM) (normally an OC or high reflector). The rest of the cavity optics does not contain any angularly dispersive elements and can be analyzed with a standard ABCD matrix

approach. The second cavity EM is also flat. The lasing cavity EM is at normal incidence for all wavelengths.
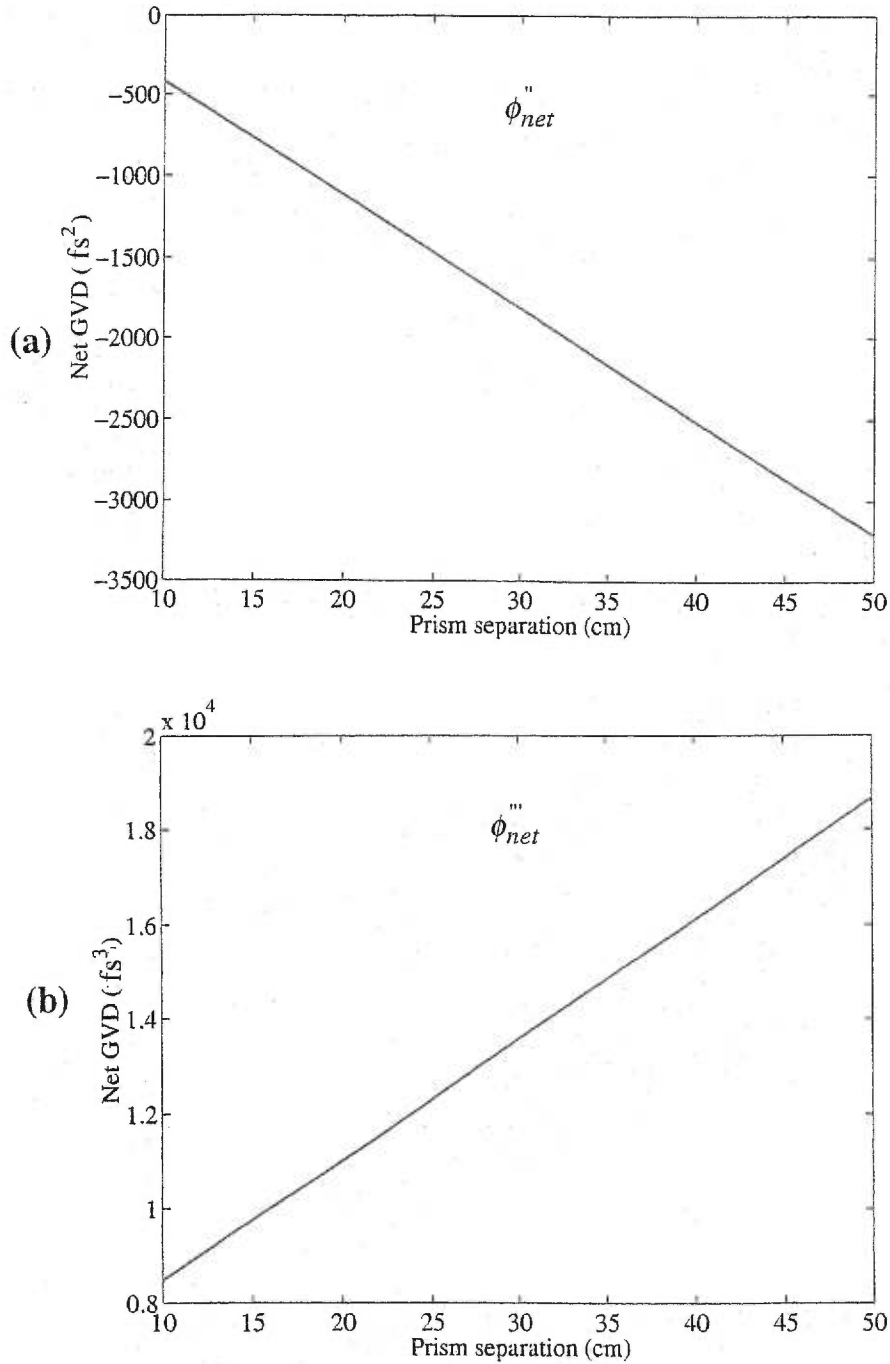
Fig. 5.6 Variation of the net second- and third-order phase distortion $\phi_{net}^{''}$ and $\phi_{net}^{'''}$ as a function of fused silica prism separation l_p for one cavity round trip at 1.5 µm.
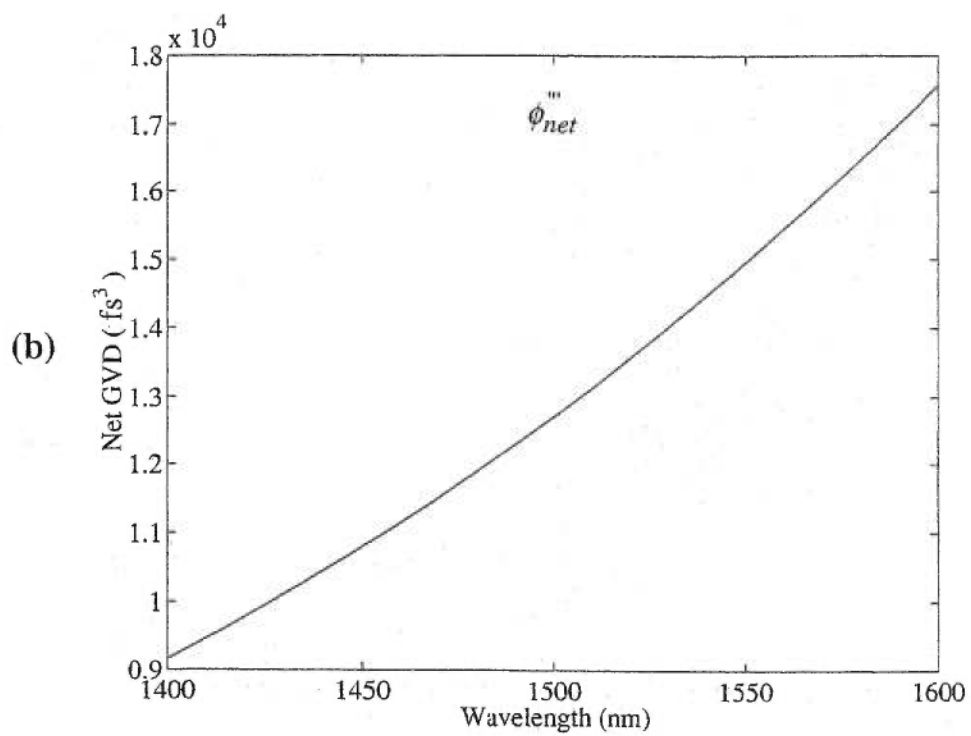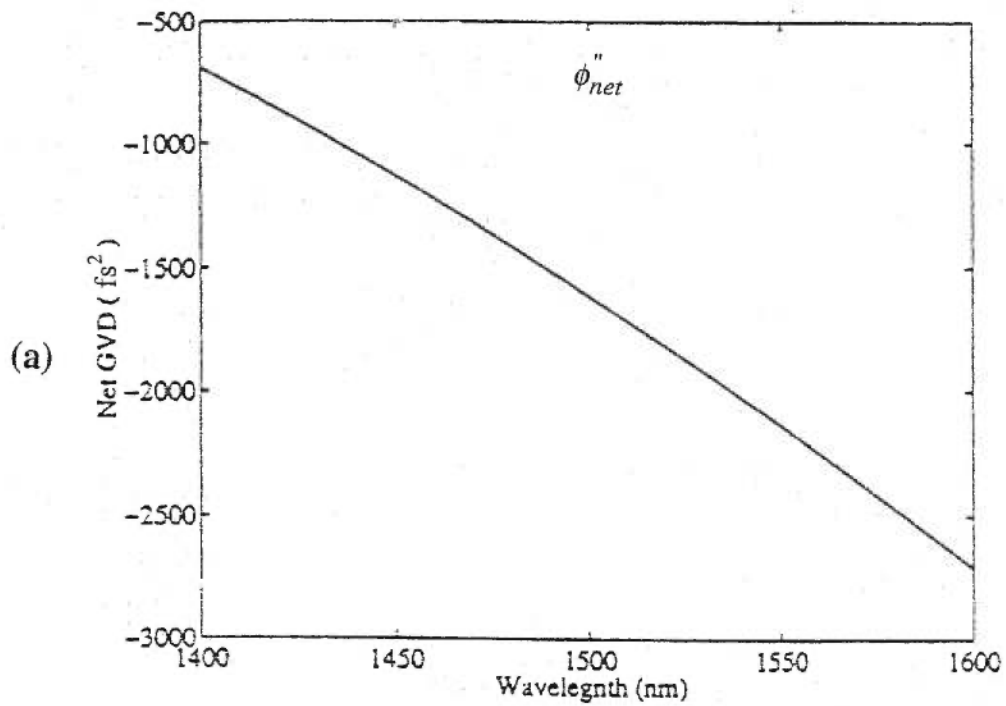
Fig. 5.7 Variation of the index of refraction of the net second-order and third-order phase distortion $\phi_{net}^{''}$ and $\phi_{net}^{'''}$ as function of wavelength for one cavity round trip and fused silica prism separation of 30 cm.

The optical axes can be traced through the laser cavity with standard ray optics (i.e., ideal plane optics). As indicated in Fig. 5.8, the angular dispersion of the prism causes different frequencies to follow different optical axes throughout the cavity, in contrast to the prism-pair setup. Two possible optical axes are labeled blue for the shorter and red for the longer wavelength in the optical spectrum of the laser. If the cavity optical elements are properly chosen, there is an intersection point X. Note that X is generally not a beam waist of the Gaussian cavity mode. After passing through the point X, light at a longer wavelength follows a longer optical path through the prism inside the cavity than at a shorter wavelength, thus generating negative GVD. So, given this intersection point X, one can obtain negative dispersion in the cavity section between OC and X with only one single prism, in full analogy to a two-prism configuration with the apex of the first prism P1, at point X (see Fig. 5.8(b)). So one can thus still use Fork et al.'s formula for the GVD calculation. Next section describes the experimental results on mode-locked laser performance with a single prism for dispersion compensation.
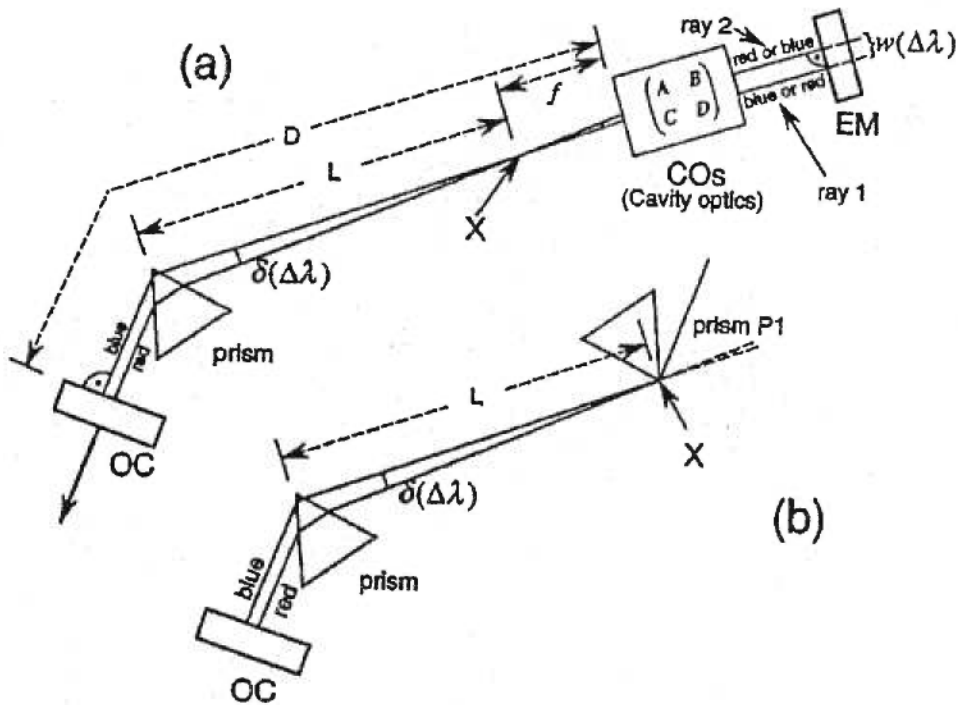
Fig. 5.8 (a) Single prism laser cavity. (b) The prism-pair approach with the first prism, P1, at intersection point X has GVD equivalent to the single-prism setup. OC's Output Coupler [11].

5.5 Experimental results on mode-locked laser performance

As described in Chapter 4 for CW operation, the prism and the SBR are removed. A flat HR mirror is placed in the cavity at one end, and an output coupler at the other. An output power of 590 mW is obtained at 1464 nm with a 1% output coupler at a pump power of 6.8 W, 4.9 W of which is absorbed. The absorbed threshold pump power is 1.13 W. A higher output power of 730 mW is obtained with 2% output coupling. The optimal output coupling is 1.7% according to Spälter et al. [9]. For wavelength tuning, a 0.75-mm thick quartz birefringent tuning plate with its optical axis tilted at 45° from the plane of the plate is inserted into the laser cavity at the Brewster angle. As shown in Fig. 5.9(a), the tuning range extends from 1345 nm to 1557 nm for a 1% output coupler, the broadest yet reported with only one set of mirrors. The wavelength cannot be tuned smoothly and the laser cannot be made to operate at certain wavelengths below 1.47 μm, because of the strong vibrational and rotational absorption lines of water present in the open cavity in form of vapor [12]. One can see a strong dip in the vicinity of 1.38 μm in the tuning curve of Fig. 5.9(a) corresponding to the resonance of the OH ion [2, 3]. In contrast, the laser can be tuned smoothly at wavelengths longer than 1.48 μm. These absorption lines also have an effect on the performance of cw optical parametric oscillators operating in this spectral range.

For pulsed operation, the end HR mirror is replaced by the SBR at the focus of a 10-cm focusing mirror, which provides a 40 μm focal waist at the SBR surface. The purpose of the concave mirror is to reduce the diameter of the beam reaching the SBR in order to obtain sufficient bleaching of the saturable absorber. However, its addition slightly changes the stability region of the resonator. A flat-wedged 1% output coupler is used. A UV-graded fused-silica prism with low water content is Brewster-cut with an apex angle of 69.38° and a base width of 15 mm. This prism follows the dispersion equation for the refractive index as given in Appendix I. The birefringent tuning plate is removed from the mode-locked laser cavity because it is a dispersive bandwidth-limiting component. Once lasing with the SBR is achieved, self-starting mode-locked operation is always obtained.

For the characterization of the mode-locked pulses, a number of diagnostic tools are employed. The mode-locked pulse train is monitored using a high-speed InGaAs detector (Antel Optoelectronic, Model AR-G10) in conjunction with an oscilloscope, and a RF spectrum analyzer is used to register the pulse repetition rate. The mode-locked laser output is analyzed using a scanning spectrum analyzer with approximately 0.2-nm wavelength resolution and an intensity autocorrelator with a 1 mm thick and 24°-cut $LiIO_3$ doubling crystal.

For ease of alignment, a flat HR, instead of the SBR, is initially inserted at the focus of the focusing mirror. Passive mode-locking with long subnanosecond pulses (~ 300 ps) is then observed [3]. Once the SBR is inserted back into the cavity, a self-starting strongly chirped pulse is observed with a pulse width of about 9 ps without any element for dispersion compensation inside the cavity. The optimized position of the SBR relative to the focusing mirror is found to be 4.9 cm. The Brewster prism is inserted into the cavity at minimum deviation with a separation of about 31 cm from the tightly focusing mirror next to the output coupler. The optical spectrum then broadens and the pulse width is reduced substantially. After further adjusting the path length by translating the intracavity prism, femtosecond pulses with self-starting and long term mode-locked behavior are observed with an average output power of over 220 mW and a repetition rate of 152 MHz. Fig. 5.10 shows a typical intensity autocorrelation and optical spectrum at a center wavelength of 1458 nm and an output power of 230 mW. The pulse width and spectrum bandwidth are 390 fs and 7 nm at FWHM, respectively. The time-bandwidth product is 0.38, 1.2 times the transform limit. Compared to a bandwidth of about 20 nm for a spectrum centered at 1.5 μm [7], we attribute the pulse broadening to the limitation imposed by water absorption. Mode-locking is maintained even during pump power fluctuations. The pulse train observed with an oscilloscope shows less than 5% pulse energy fluctuation, mainly due to the pump power instability. It should be noted that double pulses or even multiple pulses are observed with center wavelengths between 1.44 to 1.48 μm when the output power exceeds 250 mW, corresponding to a pump power of 6.5 W. Spälter et al. [9] explained the multiple pulsing with the saturable behavior of the saturable absorber.

By rotating the prism at different Brewster angles, we are able to tune the mode-locked laser from 1440 to 1510 nm, as shown in Fig. 5.9(b). It is obvious that the SBR together with the output coupler limit the spectral bandwidth of the Cr^{4+}:YAG laser, such that the mode-locked pulse cannot be tuned beyond 1.51 µm. We find that femtosecond mode-locked operation depends greatly on the center wavelength. About 400 fs long pulses are obtained at certain centre wavelengths below 1.5 µm, such as 1449, 1458, 1462, 1472, 1476, 1488 nm etc. Outside these centre wavelengths, femtosecond pulses are severely broadened, or even collapse to the picosecond regime. Compared with picosecond pulses, femtosecond pulses seem more sensitive to environmental perturbations.

At this point, further consideration is given to the effect of the water absorption line on the self-starting mode-locking of the laser in a cavity open to ambient air. As picosecond pulses are relatively long, their spectral bandwidths are less than 2 nm. The pulse spectra are therefore narrow enough to fit between the water absorption lines, and are unaffected by them. However, femtosecond pulses require much wider bandwidths, e.g., a 200 fs pulse at 1.5 µm corresponds to a bandwidth of at least 12 nm. Therefore the femtosecond pulses can only be obtained between major absorption lines with larger separations. The spectrum centered at 1458 nm, as shown in Fig. 5.10(a), for instance, fits between the 1453 nm and the much weaker 1464 nm absorption lines [21]. A larger broadening spectrum would be distorted by the water absorption lines. The rapid change of the dispersion associated with the absorption lines [2] also limits further broadening of femtosecond pulses.
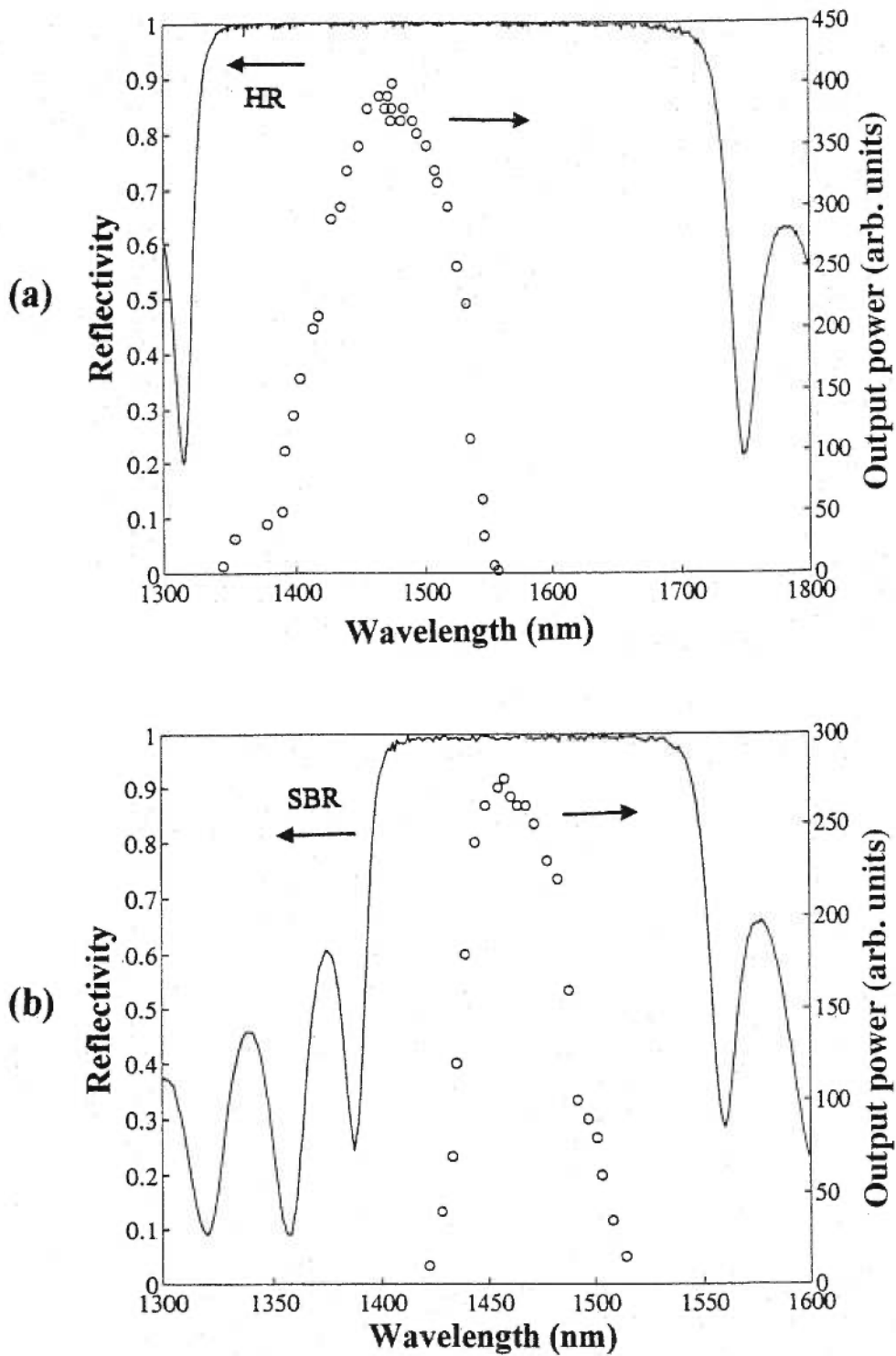
Fig. 5.9 Measured tuning curves for (a) cw and (b) SBR mode-locked Cr^{4+}:YAG laser. The measured reflectance spectrum for the high reflector and SBR are also given.
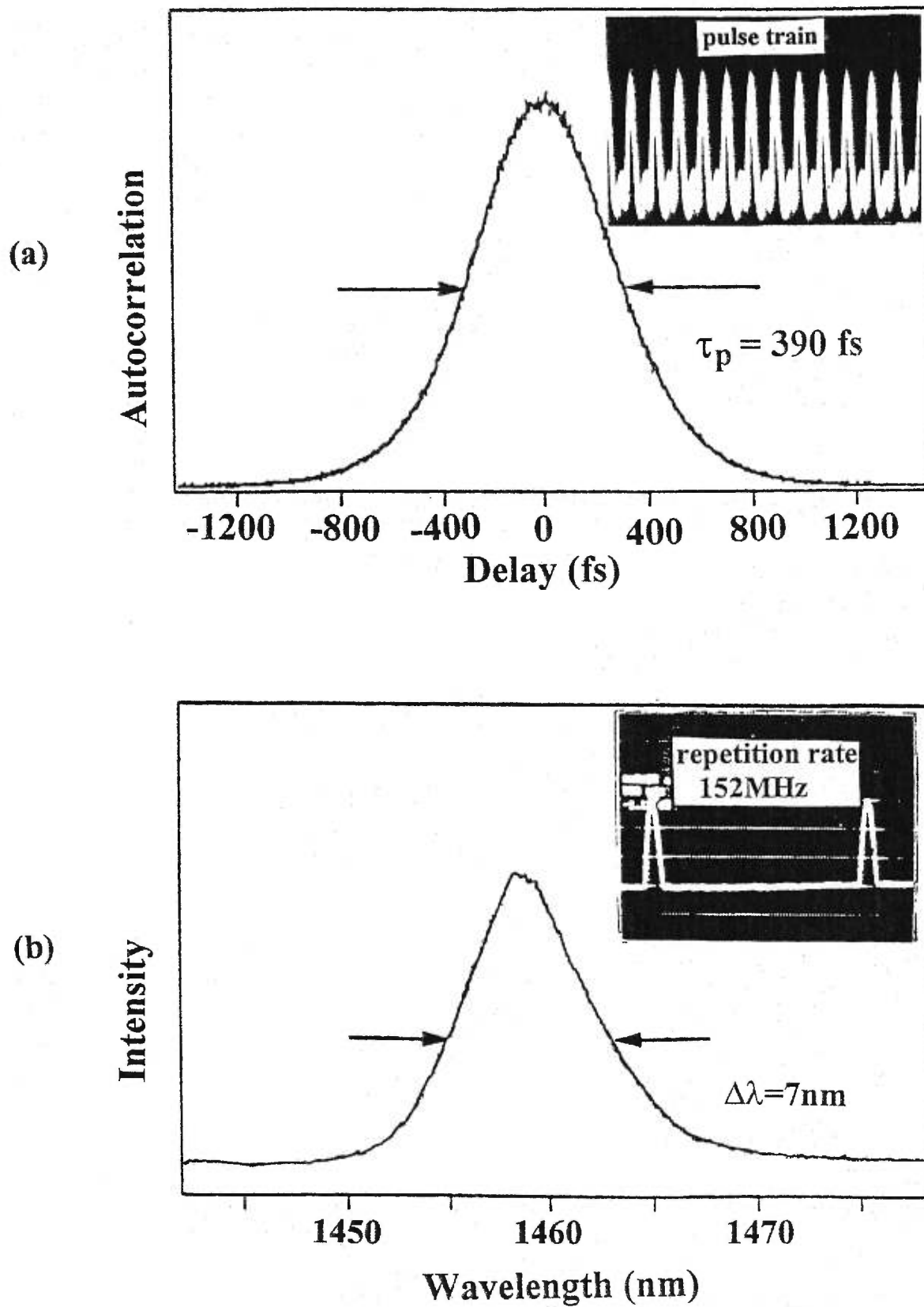
Fig. 5.10 Measured intensity autocorrelation (a) and corresponding optical spectrum (b) of the mode-locked pulses generated by the Cr^{4+}:YAG laser. The insets show the pulse train and frequency spectrum, respectively.

5.6 Characterization of the strained InGaAs/InAlAs saturable Bragg reflector

A semiconductor saturable Bragg reflector (**SBR**) is an intensity dependent reflector mirror for use in mode-locking low-gain solid state lasers for the generation of ultrashort optical pulses. The SBR structure comprises a highly reflective mirror stack (> 99%) and one or two quantum wells (**QW**) acting as the saturable absorbing medium. Thus, this structure actually acts as a low-loss saturable absorber that can be employed directly within the main lasing cavity of a laser. The use of a SBR to passively mode-lock solid state lasers has recently been shown to be particularly attractive in obtaining stable ultrashort optical pulses in a self-starting manner [22]. The SBR, which is fabricated by the monolithic growth of the saturable absorber together with the Bragg reflectors by using advanced semiconductor growth techniques, has a relatively simple structure and requires no post-growth processing. Advantageously, it can be designed to operate in a wide spectral range, is relatively alignment-insensitive, has a fast response time, and exhibits a large nonlinear reflectivity response. A SBR structure incorporating a single AlAs/AlGaAs QW was successfully employed to mode-lock a diode pumped Cr:LiSAF laser yielding 100 fs pulses at 850 nm [23]. However, the fabrication of SBRs capable of mode-locking a laser operating at the much longer wavelengths associated with the telecommunication applications (e.g., 1300 nm and 1550 nm) presents severe challenges due to the unavailability of lattice-matched QW materials. Recently, an InGaAs/InP SBR structure was proposed by Knox's group at Lucent Technologies to mode-lock 1.5 μm lasers such as Cr^{4+}:YAG [8] and Er-Yb fibre lasers [24]. Preferably, strained GaInAs/AlInAs SBRs, which were fabricated by growing double GaInAs/AlInAs QWs within a GaAs/AlAs Bragg reflector stack, are particularly interesting for ultrafast pulse generation in the range of 1.0 to 1.6 μm. Their self-starting mode-locked operation has been demonstrated in Cr^{4+}:forsterite lasers at 1.3 μm [25] and Cr^{4+}:YAG lasers at 1.5 μm [7]. The strain effects seem responsible for the improvement in the fast nonlinear response, which is beneficial for the mode-locking performance. Dislocations resulting from relaxation are present in many strained-layer devices and understanding how they

affect overall device performance is of prime importance. For example, the dislocations in the active layers of semiconductor lasers are efficient non-radiative recombination centres and play a role in both the rapid and gradual degradation processes [27, 28]. Despite the great success of the mode-locking properties of SBR, to our knowledge, there are few structural and optical characterizations reported so far. In this section, we report on the design and the characterization of such a mode-locking device structure by means of high-resolution x-ray diffraction (**HRXRD**) and photoluminescence measurements. This device was used as the intracavity mode-locking element used in our self-starting mode-locked Cr^{4+}:YAG laser system [26] to produce 390 fs pulses with an output power as high as 240 mW as described above.

5.6.1 Experimental description

HRXRD has been used to determine precisely the structural parameters of the grown samples. The high resolution was achieved with a four-crystal Ge monochromator in the (220) reflection mode on a high resolution Philips diffractometer. The Cu $K\alpha_1$ beam ($\lambda =$ 1.54056 Å) was incident on the sample through a slit of 1 x 1 mm^2 cross section at the end of the monochromator. For the optical measurements, the sample was mounted strain-free in a helium flow cryostat. The photoluminescence was excited using the 514.5 nm line of an Ar^+ laser. The signal was dispersed by a 1-m spectrometer (0.5 meV resolution) and detected by a liquid-nitrogen-cooled Ge p-i-n photodiode using conventional lock-in techniques. The PL spectra were taken with excitation density of about 100 mW/cm^2.

5.6.2 Experimental results and discussions

Fig. 5.11 shows the symmetric (004) and asymmetric (113$^+$/113$^-$) HRXRD diffraction rocking curves of the SBR. The experimental (004) rocking curves in Fig. 5.11(a) show up to 10 satellite peaks around the main GaAs and AlAs Bragg peaks. The small linewidths of these satellite peaks indicate the good quality of this Bragg reflector, because any fluctuation in either the thickness of each period or in the lattice constant of

the material would lead to a broadening of the x-ray diffraction peaks, especially the satellite peaks. The measured FWHM of the main peaks and the first-order satellite peaks are about 30 arc sec. Varying the positions of the x-ray beam does not change the linewidth across the sample for an area of about 5 x 5 mm^2. However, due to the large lattice-mismatch of 3.7%, the double QW (004) Bragg peaks are broad and no thickness interface fringes are visible, suggesting that significant strain relaxation occurred. Such strain is normally relaxed by misfit dislocations at the interface between the lattice-mismatched buffer layer and the substrate. The lattice distortion near the dislocated interface leads to variations in the tilt of the diffraction planes across the area irradiated by the x-ray beam causing the broadening of the QW peaks and loss of the thickness fringes. In order to determine the relaxation, one can measure the parallel mismatch from any set of inclined lattice planes. Fig. 5.11(b) shows that the 113 rocking curves with high and low angle of incidence recorded from the SBR sample. The QW Bragg peaks in the 113$^+$ and 113$^-$ rocking curves have different separations with respect to the GaAs (113) peaks. The 113$^+$ rocking curve has a higher incident angle of 52.1°, and is less sensitive to the small angle change. Hence, the 113$^+$ spectrum lost the thickness fringes and the AlAs Bragg peak. Since no dislocations are detected in the GaAs/AlAs multilayers, the relative displacements of the QW Bragg peaks with respect to the GaAs substrate in the 113 rocking curves can be used to determine the lattice parameters parallel, $a_{//}$, and perpendicular, $a_\perp$, to the substrate surface. The relaxation, R, representing how far the multilayer is from the completely coherent ($R = 0$) to the completely relaxed ($R = 100\%$) situations, is calculated from the differences between the in-plane strain and the strain for a completely relaxed QW layer deposited on the GaAs substrate, i.e.:

$$R = \frac{(a_{//} - a_{GaAs})}{(a_{InP} - a_{GaAs})} \qquad \text{Eq.5.5}$$

From Fig. 5.11(b), the QW layer is found to be 94% relaxed.

The in-plane strain in each layer of the strained interface $\varepsilon^{A,B}$ is calculated from the measured $a_{//}$ and the undistorted lattice parameters of the layer, $a^{A,B}$, as

$$\varepsilon^{A,B} = \frac{(a_{//} - a^{A,B})}{a^{A,B}} \qquad \text{Eq.5.6}$$

where *A* and *B* refer to the GaAs and InAlAs buffer layers, respectively. The tensile strain at room temperature in the GaAs layer is about 3.6×10^{-2} for the SBR sample. Similarly, the compressive strain in the InAlAs buffer layer is about -2.2×10^{-3}.

The PL measurements were carried out at various temperatures. At room temperature, the SBR sample exhibits a high intense photoluminescence peak at 867 nm, ascribed to the GaAs electron-hole recombination [29]. The full width at half maximum (FWHM) of the peak is found to be 16 meV at room temperature, and about 24 meV at liquid nitrogen temperature. This is in agreement with previous results [29]. The PL emission of GaAs corroborates the high crystal quality of the GaAs/AlAs Bragg reflector structure, as evidenced by HRXRD. However, we were unable to obtain any quantitative information on the spectral position and shape of the actual QW band-edge around 1.5 μm at room temperature, even down to liquid nitrogen temperature. The PL signal from the double GaInAs layers was obtained only at much lower temperatures (typically less than 20 K). It was thought to be due to the small exciton binding energy in QW structures. Fig. 5.12 shows the PL spectra obtained from the SBR sample at 6 K. As is readily apparent from Fig. 5.12(a), sharp resonance peaks, associated with heavy-hole (HH) and light hole (LH) excitons near the n = 1 and n = 2 quantized subband edges, were observed [30]. The FWHM of the PL peaks at 6 K is ~ 20 meV, which is comparable to the results from the lattice-matched GaInAs/AlInAs QW systems [31-32]. Note that no other structure indicative of any other defects was observed in the wavelength range between the GaAs and the GaInAs QW emissions. More interestingly, Fig. 5.12(b) compares the PL spectrum with the room temperature transmission spectrum of the SBR (derived from the reflection spectrum as shown in Fig. 5.2(b)). As shown in Fig. 5.12(b), there exists a large similarity in shapes between the PL spectrum and transmission spectrum. This led to the possibility that sharp resonance peaks, as shown in Fig 5.12(a), might come from the Fabry-Perot effect of the Bragg reflector other than the QW structures.

The SBR sample showed an excellent nonlinear optical absorption response in our experiment [7] on ultrafast pulse generation with a response time of an order of a few ps. The dominating mode-locking dynamics [22] are apparently those of quantum-well saturation, instead of the pure Bragg reflection. The ultrafast recovery of the saturation

absorption is explained as follows: the low temperature growth of the SBR structure introduces a sufficient concentration of misfit dislocations at the interface close to the strain-relief layer. Such dislocations resulting from the strain relaxation act as efficient non-radiative recombination centres, such as those found in semiconductor lasers [27, 28]. Fast absorption recovery is achieved by thermally activated detrapping of photoexcited electrons from the wells into the barriers, followed by recombination in the barriers. The temporal response of the nonlinearity is determined by the carrier combination time, which is reduced from a few nanoseconds to picoseconds by low temperature growth [33, 34]. In the laser experiment, the non-radiative recombination sources remove the carriers in the QW before the next optical pulse arrives in the cavity, thus causing the ultrafast pulse generation at a high repetition rate. Mace et al. [35] demonstrated that an intensity of 15 kWcm^{-2} is required to reduce the absorption by one half, which is well below the intracavity intensity at the SBR surface through tight focusing in the laser cavity [26].
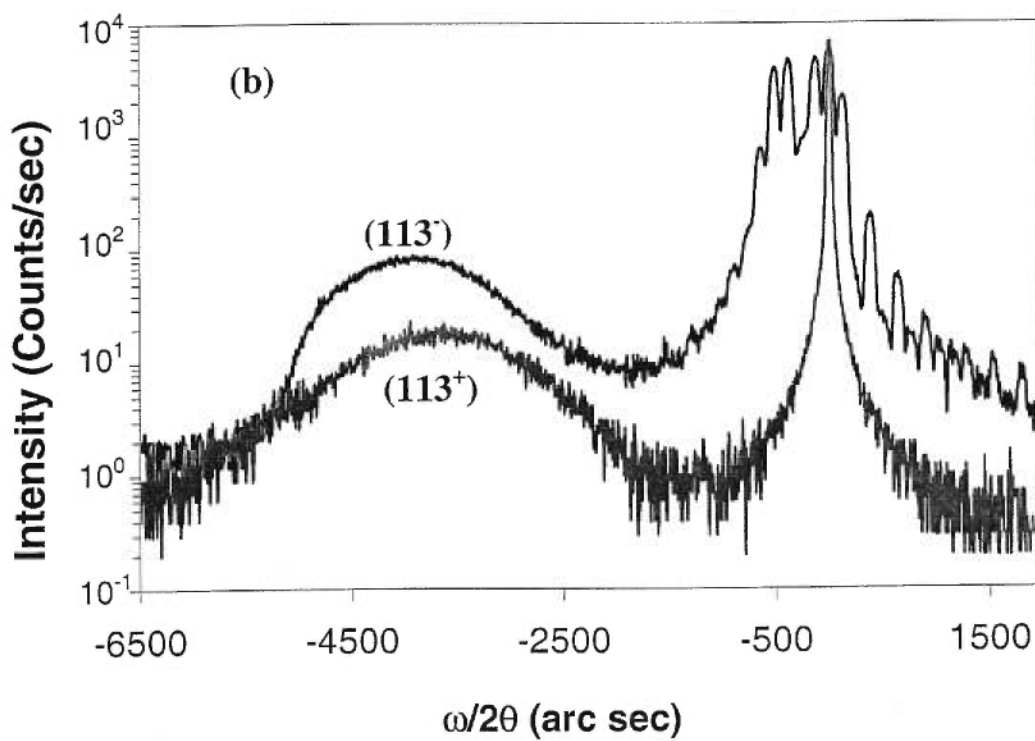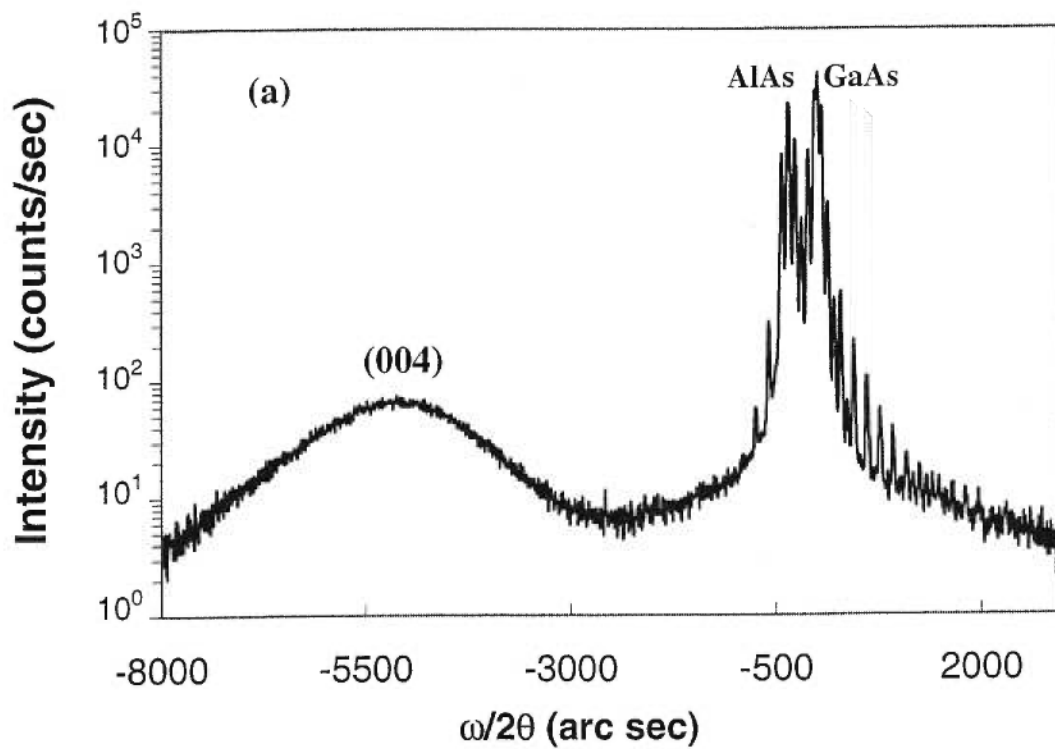
Fig. 5.11 (a) Symmetric (004) and (b) asymmetric $(113^+/113^-)$ diffraction rocking curves of the SBR.

123

(a)

(b)
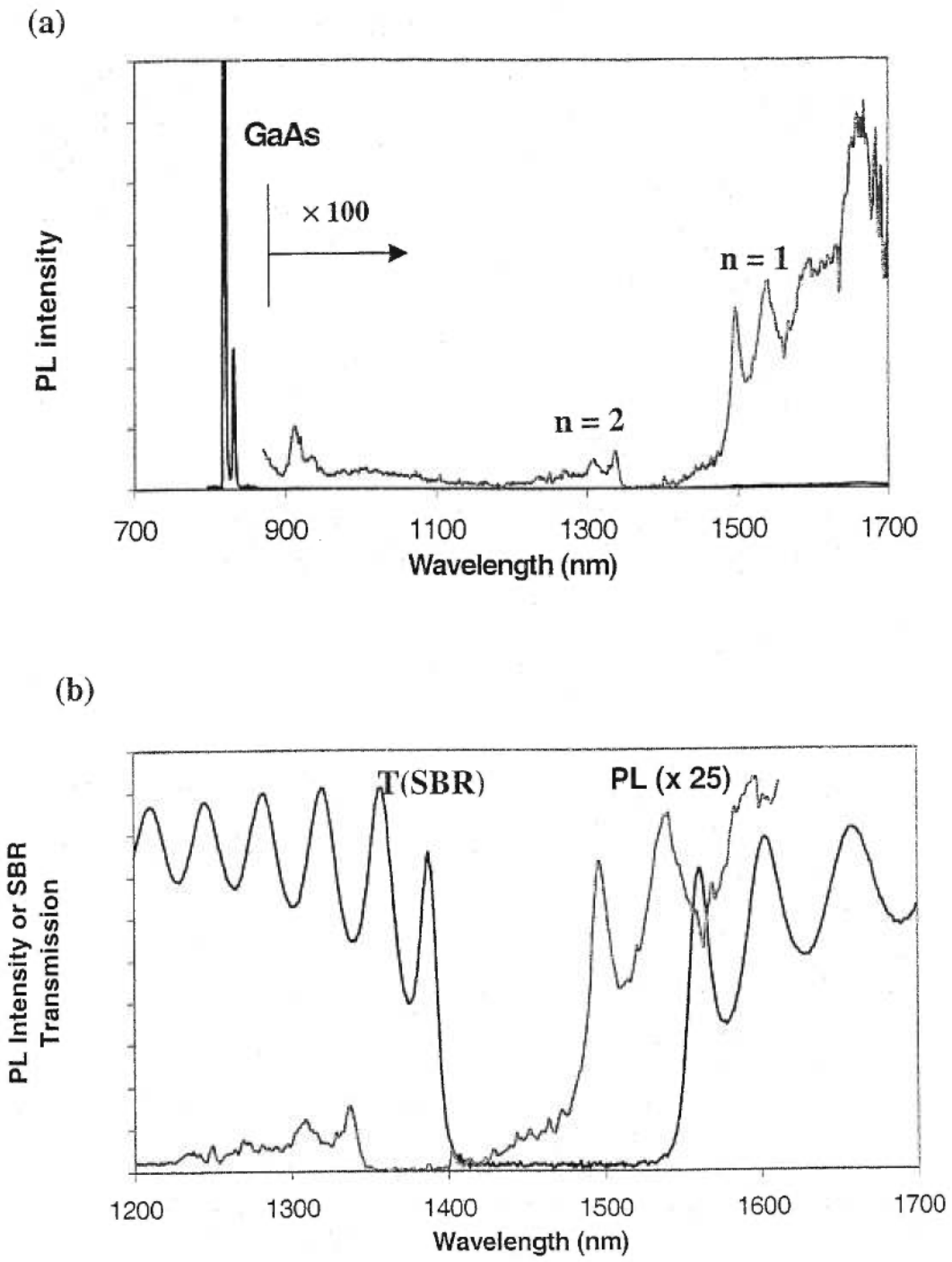
Fig. 5.12 (a) Photoluminescence spectrum of the SBR at 6 K and (b) comparison of the photoluminescence with transmission spectrum of the SBR from 1200 to 1700 nm.

124

5.7 Summary

In summary, we have demonstrated a self-starting passively mode-locked Cr^{4+}:YAG laser with a SBR as an intracavity mode-locking device and with a single prism to achieve net negative intracavity dispersion. 390 fs pulses with an output power of 230 mW were obtained at a repetition rate of 152 MHz with centre wavelengths shorter than 1.5 μm. With pulse energies of up to 1.5 nJ and a corresponding peak power of 4 kW, this laser can be used for the study of the nonlinear response of high-speed photonic devices for the demanding 10 Gb/s data rates [36]. Moreover, the single prism configuration has important implications for compact cavities with prismatic output couplers [12], where the prism and the output coupler are combined into one intracavity element.

A strained InGaAs/InAlAs saturable Bragg reflector was fabricated in industry following our specifications from layers grown by molecular beam epitaxy. The device consisted of nominally 25 periods of a GaAs/AlAs Bragg reflector structure incorporating double InGaAs/InAlAs quantum wells lattice-matched to InP. The SBR was measured to be more than 99.5% reflecting from 1410 to 1525 nm. The structural parameters for the sample were obtained from high resolution x-ray diffraction rocking curves. The quantum wells contained partially relaxed interfaces where the relaxation was characterized by misfit dislocations. The photoluminescence measurements showed a lack of well-defined band edges and exciton structure, indicating a poor linear optical response at room temperature. The fast recovery of the SBR nonlinear response was explained by the presence of dislocations which act as non-radiative recombination centers.

5.8 References:

1. A. Sennargolu, C.R. Pollock and H. Nathel, Opt. Lett. **19**, 390 (1994).

2. P. J. Colon, Y.P. Tong, P.M.W. French, J. R. Taylor and A.V. Shestakov, Opt. Lett. **19**, 1468 (1994).

3. Y. Ishida and K. Naganuma, Opt. Lett. **19**, 2003 (1994).

4. G. Gerullo, S. De Siverstri and V. Magni, Opt. Lett. **19**, 1040 (1994).

5. Y. P. Tong, J.M. Sutherland, P.M.W. French, J.R. Taylor, A.V. Shestakov and B.H.T. Chai, Opt. Lett. **21**, 644 (1996).

6. B.C. Collings, J.B. Stark, S.Tsuda, W.H. Knox, J.E. Cunmingham, W.Y. Jan, R. Pathak and K. Bergman, Opt. Lett. **21**, 1171 (1996).

7. M.J. Hayduk, S.T. Johns, M.F. Krol, C.R. Pollock and R.P. Leavitt, Opt. Comm. **137**, 55 (1997).

8. B.C. Collings, K. Bergman and W.H. Knox, Opt. Lett. **22**, 1098 (1997).

9. S. Spälter, M Bohm, M. Burk, B. Mikulla, R. Fluck, I.D. Jung, G. Zhang, U. Keller, A. Sizmann and G. Leuchs, Appl. Phys. B **65**, 335 (1997).

10. J. J. Fontarine, W. Dietel and J. C. Deels, IEEE J. Quantum Electron. **19**, 467 (1983).

11. D. Kopf, G.J. Spuhler, K.J. Weingarten and U. Keller, Appl. Opt. **35**, 912 (1996).

12. M. Ramaswamy-Prye and J.G. Fujimoto, Opt. Lett. **19**, 1756 (1994).

13. D.I. Babic, K. Streubel, R.P. Mirin, N. M Margulit, J.E. Bowers, E.L. Hu, D.E. Mars, L. Yang and K. Carey, IEEE Photonics Tech. Lett. **7**, 1225 (1995).

14. S. Nojima and H. Asahi, J. Appl. Phys. **63**, 479 (1988).

15. R. Takahashi, Y. Kawamura, T. Kagawa and H. Iwamura, Appl. Phys. Lett. **65**, 1790 (1994).

16. O.E. Martinez, J.P. Gordon and R.L. Fork, J. Opt. Soc. A **1**, 1003 (1984).

17. J.P. Gorden and R.L. Fork, Opt. Lett. **9**, 153 (1984).

18. R.L. Fork, C.H. Brito Cruz, H.C. Becker and C.V. Shank, Opt. Lett. **12**, 483 (1987).

19. R.L. Fork, O.E. Martinez and J.P. Gordon, Opt. Lett. **9**, 150 (1984).

20. H. Kogelink and T. Li, Appl. Opt. **5**, 1550 (1966).

21. D.A. Gilmore, P.V. Cvijin and G.H. Atkinson, Opt. Commun. **103**, 307 (1993).

22. S. Tsuda, W.H. Knox, S.T. Cundiff, W.Y. Jan and J.E. Cunningham, IEEE J. Selected Topics QE **2**, 454-64 (1996).

23. S. Tsuda, W.H. Knox, E.A. de Souza, W.Y. Jan and J.E. Cunningham, Optt. Lett. **20**, 1406 (1995).

24. B.C. Collings, K. Bergman, S. Tsuda and W.H. Knox, CLEO'97, CThH2, (1997).

25. P.T. Guerreiro, S. Ten, E. Slobodchikov, Y.M. Kim, J.C. Woo and N. Peyghambarian, Opt. Comm. **136**, 27 (1997).

26. Y. Chang, R. Maciejko, R. Leonelli and A. SpringThorpe, Appl. Phys. Lett. **73**, 2098 (1998).

27. S.N.G. Chu, S. Nakahra, M.E. Tuigg, L.A. Koszi, E.J. Flynn, A.K. Chin, B.P. Seger and W.D. Johnston, J. Appl. Phys. **63**, 611 (1988).

28. B.C. de Cooman, C.W.T. Bulle-lienloma, J.A. de Poorter and W. Nijman, J. Appl. Phys. **67**, 3919 (1990).

29. D.A Harrison, R Ares, S.P. Watkins, M.L.W. Thewalt, C.R. Bolognesi, D.J.S. Beckett and A.J. SpringThorpe, Appl. Phys. Lett. **70**, 3275 (1997).

30. S. Nojima and H. Asahi, J. Appl. Phys. **63**, 479 (1988); Y. Kawamura, K. Wakita and H. Asahi, Electron. Lett. **21**, 1168 (1985).

31. D.F. Welch, G.W. Wicks and L.F. Eastman, Appl. Phys. Lett. **46**, 991 (1985).

32. W.Z. Shen, S.C. Shen, Y. Chang, W.G. Tang, J.X. Chen and A.Z. Li, J. Appl. Phys. Lett. **80**, 5348 (1996).

33. R. Takahashi, Y. Kawamura, T. Kagawa and H. Iwamura, Appl. Phys. Lett. **65**, 1790 (1994).

34. E.L. Delpon, J.L. Oudar, N. Bouche, R. Raj, A. Shen, N. Stelmakh and J.M. Lourtioz, Appl. Phys. Lett. **72**, 759 (1998).

35. D.A.H. Mace, M.A. Fisher, M.G. Burt, E.G. Scott and M.J. Adams, Opt. Lett. **15**, 189 (1990).

36. C. Rolland, L.E. Tarof and A. Somani, IEEE lts **3**, 16 (1992).

Chapter 6

CONCLUSIONS

6.1 Summary of the thesis

The previous chapters detailed some of the experimental work carried out to generate ultrashort optical pulses for high capacity optical communications. The principal objective was to produce a testing laser source and identify the most versatile mode-locking scheme that has the potential for commercialization and long lifetime reliable operation. In carrying out the task, we critically examined the effectiveness of self-starting and passive mode-locking with a novel saturable Bragg reflector structure.

The work presented in this thesis demonstrated that Cr^{4+}:YAG is a potentially useful source of ultrashort pulses over the wavelength range from 1.33 to 1.56 μm. Useful cw and mode-locked output powers of several hundred millwatts were routinely achieved. A broad cw tunable range from 1.34 to 1.56 μm was demonstrated. With the cavity simplicity and the possibility of more compactness, the Cr^{4+}:YAG laser provides a competitive alternative to conventional cryogenic colour centre lasers at this wavelength such as NaCl:OH⁻ or complex optical parametric oscillators synchronously pumped by a Ti:sapphire laser.

The experiments revealed that Cr^{4+}:YAG has a number of laser properties which are unique amongst vibronically broadened gain media. The low number of active Cr^{4+} ions in the crystal, and hence the low gain density, makes Cr^{4+}:YAG particularly susceptible to atmospheric absorption effects, and also leads to a saturation of the pump absorption at modest pump power levels so that the pump energy deposited in the gain medium depends on the laser flux in the cavity. Thermal lensing in Cr^{4+}:YAG therefore depends on the rate of stimulated emission, and as the laser beam is established, thermal lensing shifts with the pattern of the heat deposited in the crystal. This effect manifests itself in the Cr^{4+}:YAG laser in a number of different ways including the slow recovery of the laser output power after a brief interruption of the cavity beam.

The intrinsic excited-state absorption for Cr^{4+} centres further identified Cr^{4+}:YAG as a low-gain medium. The novel saturable Bragg reflector provides a self-starting mode-locking mechanism with minimum cavity loss enabling an efficient mode-locking mechanism of such low-gain lasers. This technique eliminates the need for a critical cavity alignment. A single prism cavity is much easier to align and losses are further reduced as a result of fewer intracavity elements and lossless wavelength tunability. Over 230-mW average output power with a pulse width of 390 fs at centre wavelengths shorter than 1.5 µm was routinely observed. Most importantly, our design has important implications for compact laser sources for the demanding 10 Gb/s data rates.

6.2 Future trends toward compact ultrafast Cr^{4+}:YAG lasers

The limit on the shortest pulse duration that can be achieved is set by the lasing bandwidth. The water vapour absorption restricts the mode-locking tuning range of the Cr^{4+}:YAG laser from 1420 to 1510 nm and therefore pulses shorter than 100 fs can in principle be generated. Even shorter pulses could be achieved by compressing the pulses outside the cavity.

When the laser was mode-locked to give 390 fs pulses, the average output power was about 240 mW and this corresponds to a peak power of over 4 kW. If the pulse train was focused and coupled into the core of a fiber, the high peak intensity would generate significant self-modulation and the spectrum would broaden. The group velocity dispersion of silica glass is negative at a wavelength longer than 1.3 µm such that the pulses would compress through the soliton effect. With a careful choice of the length of the fiber, pulse compression by a factor of three or four could be possible with minimal power loss.

Even shorter pulses can be generated by removing the atmospheric effects which limit the mode-locked tuning range. Gilmore et al. [1] mapped the absorption bands of atmospheric water around 1.45 µm with a Cr^{4+}:YAG laser using intracavity absorption spectroscopy and they found a complex set of absorption lines. In Gilmore's experiments, the laser cavity was sealed in a container which was purged with dry nitrogen gas to

remove all traces of the atmospheric water vapour. This removed the water absorption lines from the Cr^{4+}:YAG tuning spectrum. If a dispersion compensated Cr^{4+}:YAG laser resonator was similarly purged to remove the water vapour, it is likely that mode-locking would be possible across the full tuning range of the laser from 1.34 to 1.56 μm.

The development of compact and inexpensive femtosecond solid state laser systems is pursued actively because it enables the range of practical applications for ultra-short pulse technology to be widened. Diode laser pumped Cr^{4+}:LiSrAlF$_6$ systems have been demonstrated [2]. They deliver femtosecond pulses with components which cost only a few thousand dollars. This is inexpensive compared to the several tens of thousands of dollars needed to set up a conventional main frame laser pumped femtosecond system.

Much greater efficiency in the conversion of electrical power to optical power can also be achieved with a diode pumped laser. A diode laser which can deliver an optical output power of 10 watts typically only consumes 50 – 100 watts of electrical power. This compares favorably to the several kilowatts of electrical power which a frame laser requires to produce an equivalent optical output power. Running and maintenance costs are also lower with a diode pump laser. Complete femtosecond solid state laser systems could be made compact and portable.

There are two key requirements for developing a diode pumped femtosecond Cr^{4+}:YAG laser system. The first one is to determine if the absorption band extends to the 780 – 880 nm range where AlGaAs diode lasers are capable of delivering several watts of optical power. The second requirement is to reduce the Cr^{4+}:YAG laser threshold as much as possible. High output powers are available from broad area diode lasers but the transverse mode beam quality is usually poor thus reduces the pumping efficiency when compared with a TEM$_{00}$ pump beam. Lower laser thresholds can be achieved using a shorter laser rod. An alternative to the direct diode laser pumping of Cr^{4+}:YAG is to use a high power Nd or Yb diode-pumped fibre laser. The fibre laser can be constructed with a double cladding such that it can present a large numerical aperture to the multimode pump light from the laser diodes but still maintain single transverse mode lasing in the Nd doped core and inner cladding [3]. The pump light is trapped within the outer cladding and irradiates the inner core and cladding to pump the 1.06 μm lasing transition. The diode-

diode-pumped fibre laser is compact and slope efficiencies of over 50 % can be achieved. The power consumption is small. This type of fibre laser produces a high quality TEM_{00} beam at 1.06 μm which can pump the Cr^{4+}:YAG laser much more efficiently than laser diodes.

The Cr^{4+}:YAG cavity configuration shown in Fig. 6.1 has recently been investigated by Mellish et al. [4] as a potential diode-pumped system. The CW Cr^{4+}:YAG gave a 90 mW maximum output power when pumped with 2.2 W from the Yb fiber laser (with approximately 1.8 W being absorbed in the rod). Mode-locking the laser by adjusting mirror M2 (Kerr-lens mode-locking) produced a pulse train at a 525 MHz repetition rate. The mode-locked laser was tunable from 1.508 to 1.54 μm, and produced pulses with a duration of less than 210 fs across this range (assuming a $sech^2$ pulse profile). The corresponding laser average output power varied from 88 to 40 mW.
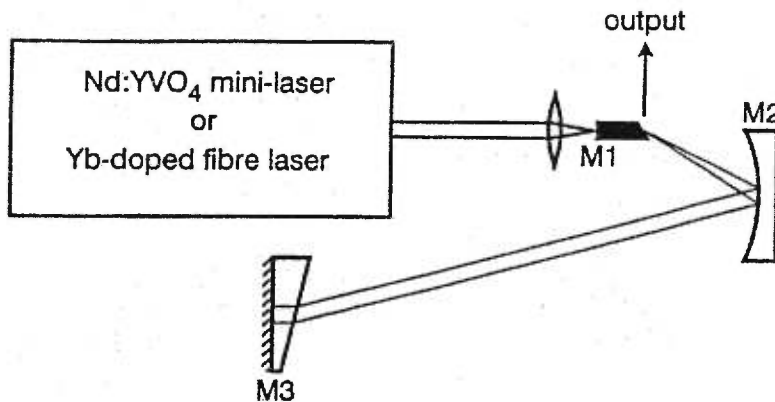
Fig.6.1 Schematic of a compact cavity configuration. [4]

Recent work by Stingl et al. [5] has demonstated negative dispersion compensation using specially designed cavity mirrors. Standard highly reflecting laser mirrors are made by laying down a stack of λ/2 thick layers of dielectric material of alternating high and low refractive index. The reflections from the layer boundaries add together constructively because of the λ/2 spacing. The overall structure can have a reflectivity of over 99.9%.

individual dielectric layers increases from the air interface at the front surface of the mirror coating to the substrate at the back. The shorter wavelengths are reflected from the upper layers of the mirror while the longer wavelengths are reflected from layers deeper in the mirror near the substrate. The 'red' light is therefore delayed with respect to the 'blue' light such that the structure has a negative dispersion.

The dispersive chirp acquired after one reflection is relatively small such that the cavity beam must bounce between the mirrors several times on each round trip to give the required GVD. Dispersive mirrors do not suffer from the third-order dispersion associated with prisms. This has enabled the generation of as short as 7.5 fs pulse [7] from a Kerr-lens mode-locked Ti:sapphire laser. This method of dispersion compensation eliminates the cavity-length constraint introduced by having to incorporate a prism pair and should enable higher repetition rates to be achieved.

Such a dispersion compensation technique has been extended to saturable Bragg reflector mirrors, which combine saturable absorption and negative GVD in one element. Kopf et al. [8] reported a mirror design with an $Al_{0.06}Ga_{0.94}As$ bulk saturable absorber intergrated into a chirped GaAs/AlAs Bragg reflector structure. A simple and compact diode-pumped mode-locked Cr^{3+}:LiSAF [8] laser was demonstrated with 160 fs pulses at 25 mW average output power. In the near future, a possible consequence of such a design may be the development of scaled-down solid-state femtosecond lasers, as small as the size of a shoe box.

6.3 References:

1. Gilmore D.A., Cvijin P.V. and Atkinson G.H., Opt. Commun. **103**, 307 (1993).

2. Mellish R., Chernikov S.V., French P.M.W., Taylor J.R., Delfyett P.J., Florez L.T. and Wigley P.J., CLEO'94, Anaheim Californian, paper CWI1 (1994).

3. Po H., Cao J.D., Laliberte B.M., Minns R.A., Robertson R.F., Rockney B.H., Tricca R.R. and Zhang Y.H., Electron. Lett. **29**, 1500 (1993).

4. Mellish R, Chernikov S.V., French P.M.W. and Taylor J.R., Electron. Lett. **34**, 552 (1998).

5. Stingl A., Spielmann Ch., Krausz F. and Szipöcs R., Opt. Lett. **19**, 204 (1994).

6. Szipöcs R., Ferencz K., Spielmann Ch. and Krausz F., Opt. Lett. **19**, 201 (1994).

7. Xu L., Spielmann Ch., Krausz F. and Szipöcs R., Opt. Lett. **21**, 1259 (1996).

8. Kopf D., Zhang G., Fluck R., Moser M. and Keller U., Opt. Lett. **21**, 486 (1996).

Appendix I

Dispersion equations for various optical materials

This appendix lists the dispersion equations of various optical materials used in this thesis to design various optical components. Glass BK7 constitutes the substrate windows for the high reflecting mirrors (including the flat and curved high reflectors, as well as output coupler) in the Cr^{4+}:YAG laser cavity. Quartz crystal is used to fabricate the birefringent filter for tuning the cw laser wavelengths. Fused silica is used for the Brewster-angled prism. The expression for the refractive index of the YAG crystal in the form of a Laurent series formula is used to analyse the dispersion characteristic of the femtosecond laser cavity. As for the refractive indices of the semiconductors constituting the saturable Bragg reflectror, there exists a large discrepancy in literature.

For fused silica and glass BK7, a Sellmeir equation is used (wavelength λ in μm).

$$n^2 = 1 + \frac{B_1 \lambda^2}{\lambda^2 - C_1} + \frac{B_2 \lambda^2}{\lambda^2 - C_2} + \frac{B_3 \lambda^2}{\lambda^2 - C_3}$$

	Fused silica	BK7
B_1	0.6961663	1.039612120
B_2	0.4079426	0.231792344
B_3	0.8974794	1.01046945
C_1	0.0684043	$6.00069867 \times 10^{-3}$
C_2	0.1162414	$2.00179144 \times 10^{-2}$
C_3	9.8961610	$1.03560653 \times 10^{-2}$

For YAG and quartz, a Laurent series formula is used (wavelength λ in μm).

$$n^2 = A_0 + A_1 \lambda^2 + \frac{A_2}{\lambda^2} + \frac{A_3}{\lambda^4} + \frac{A_4}{\lambda^6} + \frac{A_5}{\lambda^8}$$

	YAG	Crystal quartz	
		n_o	n_e
A_0	3.295827	2.3849	2.35728
A_1	-0.012381	-1.259×10^{-2}	-1.17×10^{-2}
A_2	0.026109	1.079×10^{-3}	1.054×10^{-2}
A_3	-5.720369×10^{-5}	1.6518×10^{-4}	134143×10^{-4}
A_4	0.000166	-1.94741×10^{-6}	-4.45368×10^{-7}
A_5	-1.122854×10^{-5}	9.36476×10^{-8}	5.92362×10^{-8}

For the semiconductors GaAs, AlAs and $Ga_{0.47}In_{0.53}As/Al_{0.48}In_{0.52}As$ multi-quantum wells (MQW), the dispersion equation is based on a single-oscillator model formulated as, (wavelength λ in μm).

$$n^2 = 1 + \frac{E_0 E_d}{E_0^2 - (1.24 / \lambda)^2}$$

	GaAs	AlAs	GaInAs	AlInAs	GAInAs/AlInAs MQW
E_0	3.65	4.70	2.02	6.4842	2.21x+2.02
E_d	36.1	33.65	20.9 (well)	27.236 (barrier)	13.2x+20.9 $x = 0.48 l_b/(l_b+l_z)$*

*: l_b denotes the thickness of the barrier while l_z denotes the thickness of the well.

Sources:

1. CVI laser optics and coating catalogue. (Fused silica, BK7, Quartz)
2. Bond W.L., J. App. Phys. **36**, 1674 (1965). (YAG)
3. Palik E.D., *Handbook of optical constants of solids*, (Academic, Boston, 1985). (GsAs)
4. Afromowitz M.A., Solid State Comm. **15**, 55 (1974). (AlAs)
5. Nojima S. and Asahi H., J. Appl. Phys. **63**, 479 (1988). (InGaAs/InAlAs)

Appendix II

ABCD theory of ray optics

According to the Gaussian beam theory, the complex beam parameter for a Gaussian beam is defined as:

$$\frac{1}{q} = \frac{1}{R} - j\frac{\lambda}{\pi n \omega^2} = \frac{1}{R} - j\frac{1}{z_0}$$

where R is the radius of the curvature of the wave front, ω is the radius of the beam, and $z_0 = n\pi\omega^2/\lambda$ is called the Rayleigh range. The real part of $1/q$ represents the divergence of the surface of constant phase and the imaginary part is a measure of $1/\omega^2$, the degree of power concentration in the axial region of the beam.

After passing through an optical system, the complex Gaussian beam parameter is transformed according to *ABCD law* as

$$q_2 = \frac{Aq_1 + B}{Cq_1 + D}$$

A, B, C and D are the resultant matrix elements characterising the optical system and $(AD-BC)=1$.

Table II.1 summarises the ray-transfer matrices corresponding to eight frequently occurring situations [1]. For optical systems that represent a combination of the above situations, one multiplies together the appropriate matrices, remembering to work backward from output to input. And check that the determinant of the resultant overall matrix is unity.

References:

1. Gerrard A and Burch J.M., *Introduction to matrix method in optics*, (John Wiley & Sons, 1994)

Table II.1 Ray-transfer matrices corresponding to eight frequently occurring situations [1].

Number	Description	Optical Diagram	Ray-transfer matrix
1	Translation ($\mathcal{T}$-matrix)		$\begin{bmatrix} 1 & t/n \\ 0 & 1 \end{bmatrix} = \begin{bmatrix} 1 & T \\ 0 & 1 \end{bmatrix}$
2	Refraction at single surface ($\mathcal{R}$-matrix)		$\begin{bmatrix} 1 & 0 \\ \dfrac{-(n_2 - n_1)}{r} & 1 \end{bmatrix} = \begin{bmatrix} 1 & 0 \\ -P & 1 \end{bmatrix}$
3	Reflection at single surface (for convention see section II.11)		$\begin{bmatrix} 1 & 0 \\ \dfrac{2n}{r} & 1 \end{bmatrix} = \begin{bmatrix} 1 & 0 \\ -P & 1 \end{bmatrix}$
4	Thin lens in air (focal length f, power P)		$\begin{bmatrix} 1 & 0 \\ -(n-1)\left(\dfrac{1}{r_1} - \dfrac{1}{r_2}\right) & 1 \end{bmatrix} = \begin{bmatrix} 1 & 0 \\ -1/f & 1 \end{bmatrix}$
5	Between principal planes of lens system in air (focal length f)		$\begin{bmatrix} 1 & 0 \\ -1/f & 1 \end{bmatrix} = \begin{bmatrix} 1 & 0 \\ -P & 1 \end{bmatrix}$
6	Between focal planes of lens system in air (focal length f)		$\begin{bmatrix} 0 & f \\ -1/f & 0 \end{bmatrix}$
7	Imaging between two conjugate planes with lateral magnification m and focal length f		$\begin{bmatrix} m & 0 \\ -1/f & 1/m \end{bmatrix}$
8	Afocal system with lateral magnification m		$\begin{bmatrix} m & 0 \\ 0 & 1/m \end{bmatrix}$

Appendix III

Biography

Yongmao Chang est né le 21 août 1966 dans la province de Hebei, en Chine. Il a reçu le baccalauréat en physique a l'Université Nankai, Municipalité de Tianjin, Chine en 1988. De sept 1988 à juin 1991, il a étudie au département de physique de l'Université Nankai, où il a obtenu le diplôme de maîtrise en 1991. Il est allé à Hong Kong en 1992. De sept 1992 à 1994, il a travaillé au "City University of Hong Kong". Il est venu au Canada en 1994. Il a travaillé a l'Université Concordia en 1994. De janvier 1995 jusqu'à présent, il a poursuivi des études de doctorat au département de physique de l'Université de Montréal, sous la supervision des professeurs Romain Maciejko (Ecole Polytechnique) et Richard Leonelli. Durant cette dernière année, il a fait ses recherches au "Components R&D" de JDS Uniphase Corporation à Ottawa.

Yongmao Chang was born on August 21, 1966 in Hebei province, P.R.China. He received the Bachelor's degree with honours in physics from Nankai University, Tianjin, China. From Sept. 1988 to June 1991, he studied at the Optical Crystal Laboratory of the Department of Physics of Nankai University, where he obtained the Master's degree in 1991. He came to Hong Kong in 1992. For the years of 1992 and 1993, he worked as a Research Associate at the Department of Physics and Material Sciences of City University of Hong Kong. He came to Canada in 1994. In the year of 1994, he worked as Research Fellowship at the Physics Department of Concordia University. From Jan. 1995 to present, he has been a Ph.D student in the Department of Physics and Thin Film Group of Université de Montréal, under the supervision of Professors Richard Leonelli and Romain Maciejko (École Polytechnique). For the last year, he was working for the fiber Bragg grating products at the Components R&D Department of JDS Fitel Inc., Ottawa. He is currently working for various measurement instrumentation products at Instrument Engineering Department of JDS Uniphase Corporation, Ottawa. His research interests include ultrafast solid state lasers, semiconductor thin film devices, fiber optic components, laser spectroscopy and optical crystals.

Appendix IV

List of Publications and Conferences

1. Yongmao Chang, Richard Leonelli, Roman Maciejko, and Anthony SpringThorpe, "Characterization of a novel intracavity mode-locking element: strained GaInAs/AlInAs saturable Bragg reflector", submitted, 1999.

2. Yongmao Chang, Roman Maciejko, Abdelhamid Benhocine, Richard Leonelli and Czeslaw Rudowicz, "Theoretical and experimental investigation of the excited-state absorption in a Cr^{4+}:YAG gain medium", OSA Trends in Optics and Photonics Series (**TOPS**) Vol. **19**, *Advanced Solid State lasers*, pp.494-502 (1998).

3. Yongmao Chang, Roman Maciejko and Richard Leonelli, *"Excited-state absorption in a Cr^{4+}:YAG gain medium"*, Paper AWD15, Technical digest of OSA Topical meeting Advanced Solid State lasers, Feb. 2-4, 1998, Coeur d'Alene, Idaho, USA

4. Yongmao Chang, Roman Maciejko, Richard Leonelli and Anthony SpringThorpe, "Self-starting passively mode-locked tunable Cr^{4+}:YAG laser with a single prism for dispersion compensation", Appl. Phys. Lett. **73** (1998) 2098-30.

5. Yongmao Chang, Roman Maciejko, Richard Leonelli and Anthony SpringThorpe, "Continous-wave and self-starting passively mode-locked broadband Cr^{4+}:YAG laser systems", Paper ICAPT98T92, Oral presentation at International Conference on Applications of Photonic Technologies (ICAPT), July 27-30, 1998, Ottawa, Canada.

6. Yongmao Chang, Roman Maciejko, Richard Leonelli and Anthony SpringThorpe, "Continous-wave and self-starting passively mode-locked broadband Cr^{4+}:YAG laser systems", Proc. SPIE **3491** (1998) 1155-7.

7. Sushil K. Misra, Yongmao Chang and J. Felsteiner, "Calculation of effective g values at low temperatures for R^{3+} ions in $RBa_2Cu_3O_{7-d}$ and $RBa_2Cu_3O_8$ (R= Rare Earth) compounds: Low temperature ordering of rare-earth ions", J. Phys. Chem. Solids **58** (1997) 1-11.

8. Sushil K. Misra, Yongmao Chang, Vesselin Petkov, Samih Isber, Salam Charar, Claude Fau, Michel Averous and Zbigniew Golacki, "Electron paramagnetic resonance of Eu^{2+} in the diluted magnetic semiconductor $Pb_{1-x}Eu_xSe$ (x = 0.013) with a cubic structure", J. Phys. : Condensed Matter **7** (1995) 9897- 904.

9. Sushil K. Misra, Yongmao Chang and Jerzy Kotlinski, "An EPR study of Cu^{2+}-doped guanidinium aluminum sulfate hexahydrate (GASH) single crystal in the 3.9-433 K temperature range: Jahn-Teller effect", J. Phys.: Condensed Matter **7** (1995) 3327-38.

10. Y.M. Chang, H.F. Wang and C. Rudowicz, "Crystal-field Energy levels of deep photorefractive Fe centers at orthorhombic and higher symmetry sites in $BaTiO_3$", J. Opt. Soc. Am. B **12** (1995) 544-52.

11. T.H. Yeom, Y.M. Chang, S.H. Choh and C. Rudowicz, "Experimental and theoretical investigation of spin-Hamiltonian parameters for the low symmetry Fe^{3+} centers in $LiNbO_3$", Phys. Stat. Solidi. (b) **185** (1994) 409-415.

12. Y.Y. Yeung, C. Rudowicz, Y.M. Chang and J. Qin, "Model Calculation of the spectroscopic states for Cr^{3+} in kyanite", J. Lumin. **60&61** (1994) 108-11.

13. Y.M. Chang, C. Rudowicz and Y.Y. Yeung, "Crystal field analysis of the 3d ions at low symmetry sites involving imaginary terms", Computers in Phys. **48** (1994) 583-8.

14. Y.Y. Yeung, J. Qin, Y.M. Chang and C. Rudowicz, "Correlation of spectroscopic properties and substitutional sites of Cr^{3+} in Aluminosilicates – I : kyanite", Phys. Chem. Mineral. **21** (1994) 526-31.

15. J. Qin, C. Rudowicz, Y.M. Chang and Y.Y. Yeung, "Correlation of spectroscopic properties and substitutional sites of Cr^{3+} in Aluminosilicates - II : sillimanite and andalusite", Phys. Chem. Mineral. **21** (1994) 532-7.

16. T.H. Yeom, S.H. Choh, Y.M. Chang and C. Rudowicz, "EPR study of low symmetry Mn^{2+} centers in $LiNbO_3$: Superposition model crystal field analysis of the zero-field splitting parameters", Phys. Stat. Solidi. (b) **185** (1994) 417-28.

17. Y.M. Chang, T.H. Yeom, Y.Y. Yeung and C. Rudowicz, "Superposition model and crystal field analysis of the $^4A_2$ and ^2E state of Cr^{3+} ions at C_3 sites in $LiNbO_3$", J. Phys. : Condens. Matter **5** (1993) 6221-30.

18. T.H. Yeom, Y.M. Chang, C. Rudowicz and S.H. Choh, "Cr^{3+} centers in $LiNbO_3$: Experimental and theoretical investigation of spin Hamitonian parameters", Solid State Commun. **487** (1993) 245-9.

19. Guifen Wang, Yongmao Chang, Genyuan Ma, Qiang Guo, Xueqing Li and Guangyin Zhang, "Relation between photoacoustic signal and sample thickness", J. Appl. Phys. **73** (11) (1993) 7275-9.

20. Chang Yongmao, Wen Jinke, Wang Huafu and Li Bing, "Refractive Index measurement and Second Harmonic Generation in a series of $LiNbO_3$:Mg(5mol%) crystals", Chinese Phys. Lett. **9** (1992) 427-30.

21. C. Rudowicz, Y.Y. Yeung, M.L. Du and Y.M. Chang, "Mannual for the crystal (Ligand) field computer package for 3d ions with appendix : values of the parameters B, C, and ξ for $3d^4$ and $3d^6$ free ions and ions in crystals", Department of Applied Science, CPHK, Research report, AP-92-29 (1992).

22. Y.Y. Yeung, C. Rudowicz and Y.M. Chang, "Model calculation of the spectroscopic properties for Cr^{3+} in kyanite", Internal conference on Luminescence and optical spectroscopy in condensed matter, Storrs, USA, August, 1993.

23. C. Rudowicz, T.H. Yeom, Y.M. Chang and S.H. Choh, "Experimental and theoretical investigation of spin Hamiltonian parameters for Mn^{2+} centers in $LiNBO_3$", 35th Rochy Mountain conference – 16th Internal EPR symposiumm, Denver, USA, July, 1993.

24. C. Rudowicz, Y.M. Chang and H.F. Wang, "Crystal field energy levels for deep Fe centers at cubic, tetragonal and orthorhombic sites in $BaTiO_3$", 6th APPC and 11th AIP Congress, Brisbane, Australian, July, 1994.

25. Y.M. Chang, J.K. Wen, B. Li and H.F. Wang, "Mechanism of resistance to photorefraction in $LiNbO_3$:Mg" (in Chinese), J. Synth. Cryst. **20** (1992) 230.

26. Y.M. Chang, J.K. Wen, B. Li and H.F. Wang, "Optical homogeneity diagnosis of $LiNbO_3$:Mg crystal using Second Harmonic Generation" (in Chinese), J. Synth. Cryst. **20** (1992) 413.

27. B. Yue, J.K. Wen, Y.M. Chang and H.F. Wang, "OH⁻ spectra of $LiNbO_3$:Mg:Ti crystal" (in Chinese), J. Synth. Cryst. **21** (1992) 412.

28. Y.M. Chang, J.K. Wen, B. Li and H.F. Wang, "Refraction index measurement of $LiNbO_3$: Mg using prism coupling method" (in Chinese), J. Synth. Cryst. **20** (1992) 290.

29. Yongmao Chang, Optical Properties of a series of highly Mg-doped $LiNbO_3$ Crystals, Master's thesis, Dept of Physics, Nankai University, Tianjin, China, June 1991.